Title
Investigating Ion Solvation in Electrolyte Solutions via X-ray Absorption Spectroscopy

Author
Smith, Jacob W.

Publication Date
2016

Peer reviewed|Thesis/dissertation

Investigating Ion Solvation in Electrolyte Solutions via X-ray Absorption Spectroscopy

By

Jacob W. Smith

A dissertation submitted in partial satisfaction of the

requirements for the degree of

Doctor of Philosophy

in

Chemistry

in the

Graduate Division

of the

University of California, Berkeley

Committee in charge:

Professor Richard J. Saykally, Chair
Professor Daniel M. Neumark
Professor David B. Graves

Fall 2016

Abstract

Investigating Ion Solvation in Electrolyte Solutions via X-ray Absorption Spectroscopy

By

Jacob W. Smith

Doctor of Philosophy in Chemistry

University of California, Berkeley

Professor Richard J. Saykally, Chair

X-ray Absorption Spectroscopy (XAS) is a powerful atom-selective probe of the local chemical environment of a target atom. Streaming liquid microjets, created by forcing liquid at high pressures (ca. 20-100 atm.) through a capillary tube of inner diameter 30-100 μm, allow for liquids to be introduced into a vacuum chamber and interrogated with soft X-rays generated by synchrotron light sources. This technique has enabled the study of many liquids and solutions. In this dissertation, the use of soft X-ray XAS for the study of the solvation of ions in electrolyte solutions is discussed. The majority of chemical reactions occur in the solution phase. The thermodynamics and kinetics of these reactions are explicitly dependent upon the local chemical environments of the reactants. Consequently, knowledge of the solvation of ions in solution is critical to understanding their chemistry in this phase. By interpreting XAS measurements with *ab initio* Density Functional Theory (DFT)-based electronic structure calculations, it is possible to acquire valuable knowledge about the local chemical environment of ions and molecules in solution, such as the solvation number and geometry and propensity to form ion pairs.

Commercial lithium ion batteries typically contain a liquid electrolyte comprising a lithium salt dissolved in a mixture of alkyl carbonates such as propylene carbonate, dimethyl carbonate, and ethylene carbonate. The solvation environment of the lithium ion in these solutions is thought to direct the formation of the Solid Electrolyte Interphase (SEI), which in turn is believed to play a critical role in determining essential cell properties including power output, recharging rate, and cycle life. Consequently, understanding this solvation environment is of critical importance. Here I report the a study of the solvation of Li^+ in solutions of $LiBF_4$ in alkyl carbonates via XAS on the carbon and oxygen K-edges. In collaboration with Dr. David Prendergast, we have performed electronic structure calculations within the eXcited electron and Core Hole (XCH) approximation and extracted a solvation number for Li^+ in propylene carbonate.

I also report the study of aqueous solutions sodium nitrate and nitrite on the nitrogen K-edge utilizing similar experimental and theoretical methods. Aqueous nitrate and nitrite salts are important commercial reagents and play a critical role in the global nitrogen cycle. A detailed understanding of their chemical environment of solution would be beneficial in understanding and modeling reactivity. Unfortunately, the nitrogen K-edge XAS spectra of these species are

found to be largely insensitive to ion pairing and solvation geometry around the anion, such that limited chemical information was extracted from this study.

For Mr. Moreland, Mr. Ilyes, and Dr. Downey, who helped me discover the desire to pursue chemical research. And for Amy, who has been with me for virtually the entire time and knew all of them.

Table of Contents

Acknowledgements

Typically, the first person acknowledged in the dissertations I've read is the research advisor. But really, what has Rich gotten out of my time at Berkeley? Several additional publications with his name on them, one of which has attracted at least a modicum of attention (and citations) outside the group. Instead, I want to acknowledge my wife first. Her primary return from my graduate career was 6+ years of a boyfriend/fiancé/husband with a job that demanded relatively long hours for relatively little pay in order to set himself up for a future career path promising relatively long hours for relatively mediocre pay. Thanks Amy. I appreciate your patience. You were usually understanding and always supportive, especially around beamtime. I'm sure I wasn't the only one who appreciated the baking.

Of course I also need to acknowledge Rich. In spite of my making light of your contribution, we know you have to put in the hours writing the endless stream of grants, reports, summaries, and annual reviews that fund our research and our salaries. I know there are other things you'd rather be doing. I couldn't have asked for a better boss: you were almost never intrusive, almost never obtrusive, and almost always available. You sent me to Germany. Twice. It's been a great pleasure working in your group.

I also appreciate all of the various Saykally Group members who have been around during my tenure. As great a boss as Rich has been, the constant access to wonderful coworkers and friends has always played a huge role in keeping work fun and interesting and helping to develop ideas and research directions. The greatest thanks are in order for the other members of the X-ray group during my time at Berkeley: Royce, Orion, Alice, Greg, and Alex. There has always been a great working atmosphere in the group, both the X-ray group and the Saykally Group as a whole. Royce in particular has been on the project for much of the same time as I and in the Saykally Group for virtually the same period, and he was always much better with calculations than I. He also contributed tremendously to the quality of the figures in my publications. Very special thanks go to the people who were not members of the X-ray group but have helped fill shifts at beamtime over the years: Tony, Kaitlin, Chris, Sumana, and Nik – none of you ever had a first-author publication from this project, but without your help at best our lives would have been much more difficult around beamtime, and at worst we would never have collected much of the data that appears in this dissertation and others. A few days or nights a year never seemed like too big a deal to any of you, but it was always huge for us.

The staff of the Advanced Light Source have been extremely helpful and always gone out of their way to support our research as well as the research of the whole user community. Special thanks go to the beamline scientists who have helped us at various beamlines during my time working at the ALS: Wanli Yang, Alex Aguilar, David Kilcoyne, and Hendrik Bluhm. I would also like to thank Jon Spear and Bruce Rude for their invaluable support at Beamlines 8 and 6, respectively, as well as Doug Taube, David Malone, and the rest of the general support staff. ALS staff have worked tirelessly, on several occasions waking up in the middle of the night, to help us keep running throughout beamtime. What we most appreciate is how happy you all always seem to be to help out, even when it's clearly inconvenient.

Computational support for this research has been provided by David Prendergast of the Molecular Foundry along with his post-docs, particularly Tod Pascal. In addition to providing the code and support in its use, David has consistently provided helpful insights not only in approaching the analysis of our existing experimental data but also in planning future directions. I haven't been to the Foundry to talk as frequently as some former group members, but I've

always come away with new and helpful ideas when I have gone. Molecular configurations from Molecular Dynamics simulations of $LiBF_4$ in alkyl carbonates have been provided by Oleg Borodin of the U.S. Army Research Laboratory. These solutions are notoriously challenging to simulate effectively, and the study contained in Chapter 3 would not have been possible without Oleg's assistance.

Finally, I want to thank my family. I know I've been far away and not home as much as we might prefer, but I'd like to think it's worked out really well.

Experimental and computational portions of the work described in this dissertation were supported by the Director, Office of Basic Energy Sciences, Office of Science, U.S. Department of Energy (DOE) under Contract No. DE-AC02-05CH11231, through the Lawrence Berkeley National Lab, Berkeley, California: experimental XA spectra were collected at Beamlines 8.0 and 6.0 of the Advanced Light Souce; computational resources for electronic structure calculations were provided by the National Energy Research Scientific Computing Center (NERSC), a DOE Advanced Scientific Computing Research User Facility; and code and support for electronic structure calculations were provided by David Prendergast as part of a User Project at The Molecular Foundry. Computational resources for molecular dynamics simulations discussed in Chapter 4 were provided by the Molecular Graphics and Computation Facility in the UC Berkeley College of Chemistry under NSF CHE-0840505.

Chapter 1: Introduction to X-Ray Absorption of Electrolyte Solutions

I. Narrative

X-ray absorption spectroscopy (XAS) is an electronic absorption spectroscopy for which the initial state is a deeply-buried core level and the final state is an unoccupied excited orbital. The photon energies corresponding to such transitions are governed primarily by the binding energies of the initial state. Because the binding energies of core electrons vary between atomic species, this makes XAS an atom-selective spectroscopy. The fine structure of XAS spectra is governed by the energy levels of the accessible unoccupied orbitals, which are typically quite spatially delocalized. This makes XAS a sensitive, atom-selective probe of the local chemical environment of a target atom. XA spectra often lack some of the complexity and ambiguity present in valence-valence electronic spectra, arising from the presence of multiple initial states of similar energy. Proper interpretation of the spectra, utilizing computational spectroscopy typically leveraging Density Functional Theory (DFT)-based electronic structure calculations, can provide detailed information on both intra- and intermolecular interactions.[1]

Our group introduced liquid microjet technology into the field of XAS in 2001, enabling the general study of liquids and solutions via this powerful spectroscopy.[2] Chapter 2 of this dissertation provides a summary review of the XAS studies that have been performed on liquid samples in the intervening years. As will be discussed in greater detail in Chapter 2, XAS has provided new insights into the intermolecular interactions in many liquids, including water, glacial acetic acid, short-change alcohols, and longer-chain alkanes. It has also proven to be a useful probe of the local environment of solutes, providing information on solvation structure, solute aggregation, and the formation of both contact and solvent-separated ion pairs in salt solutions. Given the critical role played by solvent molecules in much of solution-phase chemical reactivity, developing a clear picture of the solvation environment of solutes is of critical importance in developing an understanding of chemical reactions in solution.[3,4] Qualitative and quantitative insights from XAS studies have proven useful in developing such pictures for many solutions with chemical or biological relevance, as discussed in Chapter 2.

In recent years, greater emphasis has been placed on XAS investigations of energy storage materials, including those for solar conversion devices, hydrogen generation, and battery components. This research has been recently reviewed.[5,6] Chapter 3 of this dissertation discusses the study of Li^+ solvation in solutions of $LiBF_4$ in alkyl carbonates. These solutions provide a model for the liquid electrolyte present in commercial lithium ion batteries. The solvation structure of the lithium ion is believed to have a directing effect on the structure of the Solid Electrolyte Interphase (SEI) formed by oxidation and reduction of the liquid electrolyte at the electrodes during initial battery cycling.[7,8] The structure of the SEI is thought to play a significant role in the rate of Li^+ transfer through the cell, thus playing a key role in determining the maximum power output and recharging rate of the battery. Furthermore, degradation of the SEI has been implicated as a major cause of battery degradation and failure.[9] Consequently, controlling SEI formation is critical to the improvement of lithium ion batteries. Furthermore, solvation and desolvation processes at the liquid interface are thought to play a significant role in Li^+ transport kinetics independent of the impact on SEI structure.[10] These factors make understanding of the Li^+ solvation environment a critical factor in optimizing battery design. We have studied the solvation of $LiBF_4$ in propylene carbonate and mixtures of ethylene carbonate and dimethyl carbonate. Quantitative analysis of the solvation environment of Li^+ in propylene

carbonate has been performed. This system is of particular interest because the solvation number in ethylene carbonate has been determined experimentally by vibrational Raman spectroscopy, but the mixture of isomers in propylene carbonate has made quantitative analysis of the solvation shell impossible via the same methodology.[11]

Chapter 4 of this dissertation comprises a study of the solvation of the sodium salts of nitrate and nitrite in aqueous solution. While the results of this study reveal a significant difference in the core binding energies of the nitrogen 1s electrons in nitrate and nitrite, simulated spectroscopy within the eXcited electron and Core Hole (XCH) approximation indicates that the XAS spectra of nitrate and nitrite are insensitive to ion pairing and solvation structure, thus limiting the chemical insight gained from this work.

II. References

(1) Stöhr, J. NEXAFS Spectroscopy; 1992; Vol. 25.

(2) Wilson, K. R.; Rude, B. S.; Catalane, T.; Schaller, R. D.; Tobin, J. G.; Co, D. T.; Saykally, R. J. X-Ray Spectroscopy of Liquid Water Microjets. J. Phys. Chem. B 2001, 105 (17), 3346–3349.

(3) Ball, P. Water as an Active Constituent in Cell Biology. Chem. Rev. 2008, 108 (1), 74–108.

(4) Buncel, E.; Stairs, R.; Wilson, H. The Role of the Solvent in Chemical Reactions; Oxford University Press: Oxford, 2003.

(5) Liu, X.; Yang, W.; Liu, Z. Recent Progress on Synchrotron-Based in-Situ Soft X-Ray Spectroscopy for Energy Materials. Adv. Mater. 2014, 26 (46), 7710–7729.

(6) Crumlin, E. J.; Liu, Z.; Bluhm, H.; Yang, W.; Guo, J.; Hussain, Z. X-Ray Spectroscopy of Energy Materials under in Situ/operando Conditions. J. Electron Spectros. Relat. Phenomena 2015, 200, 264–273.

(7) Xu, K.; Lam, Y.; Zhang, S. S.; Jow, T. R.; Curtis, T. B. Solvation Sheath of Li+ in Nonaqueous Electrolytes and Its Implication of Graphite/Electrolyte Interface Chemistry. J. Phys. Chem. C 2007, 111 (20), 7411–7421.

(8) von Cresce, A.; Xu, K. Preferential Solvation of Li+ Directs Formation of Interphase on Graphitic Anode. Electrochem. Solid-State Lett. 2011, 14 (10), A154.

(9) Harris, S. J.; Lu, P. Effects of Inhomogeneities - Nanoscale to Mesoscale - on the Durability of Li-Ion Batteries. J. Phys. Chem. C 2013, 117, 6481–6492.

(10) Xu, K.; von Wald Cresce, A. Li+-Solvation/desolvation Dictates Interphasial Processes on Graphitic Anode in Li Ion Cells. J. Mater. Res. 2012, 27 (18), 2327–2341.

(11) Allen, J. L.; Borodin, O.; Seo, D. M.; Henderson, W. A. Combined Quantum chemical/Raman Spectroscopic Analyses of Li+ Cation Solvation: Cyclic Carbonate solvents—Ethylene Carbonate and Propylene Carbonate. J. Power Sources 2014, 267, 821–830.

Chapter 2: Summary Review of Soft X-Ray Absorption Spectroscopy Experiments on Liquids and Solutions

I. Introduction

Modern 2nd- and 3rd-generation synchrotron light sources, utilizing wiggler and undulator radiation sources, are capable of producing X-ray beams with high flux (ca. 10^{10} to 10^{16} photons/s), excellent resolving power (typical $E/\Delta E$ = 1,000-10,000), small spot sizes (ca. a few hundred microns), and broad tunability (e.g. a single beamline may be able to produce photons with energies spanning 2 orders of magnitude, and a single facility may simultaneously produce beams in energy regimes ranging from the far infrared to hard X-ray). Access to such bright, tunable, and monochromatic sources has enabled a new suite of X-ray spectroscopies. Perhaps the most straightforward and widespread approach is soft X-ray Absorption Spectroscopy (XAS).

Soft X-rays are loosely defined as those having short attenuation lengths in most media, including air. While a variety of figures have been suggested for the upper energy bound of this region, 5 kEV (~0.25 nm, 4×10^7 cm^{-1}, 1.2 kHz) can be considered a reasonable cutoff between the soft and hard X-ray regimes. Studies involving X-rays below this energy have typically been carried out in high vacuum (HV) or ultra-high vacuum (UHV) chambers as a result of the short attenuation length of such photons in air. This requirement has historically limited the applicability of soft X-ray spectroscopies for the study of liquids – while XAS experiments became widespread beginning in the 1970s,[1,2] they did not become commonplace for liquid samples until the introduction of liquid microjet technology into the field by Wilson *et al.* in 2001.[3] Hence, this review covers primarily ~15 years of experiments in this area. A summary review of XAS and other X-ray techniques for the study of liquid samples has recently been published by Lange and Aziz.[4] In addition, Nilsson and coworkers have published several multi-technique reviews of X-ray spectroscopy of water.[5–7]

II. Experimental Techniques

The soft X-ray energy regime corresponds to the typical range of binding energies of core-shell electrons. Consequently, the dominant interaction between soft X-rays and matter is photon absorption and excitation of core electrons into unoccupied energy levels or unbound continuum states as photoelectrons. In the soft X-ray regime, this process is orders of magnitude stronger than scattering processes.[8] As core-level binding energies vary substantially from atom to atom, XAS techniques are highly atom-specific. The sensitivity of the unoccupied valence electronic structure to the local environment make XAS sensitive to the local intra- and inter-molecular chemical environment of the target atom. The majority of studies discussed in this review involve experiments on the absorption K-edges of low-z atoms; viz. absorptions with an initial state of n=1. Absorptions from higher energy levels advance through the alphabet (e.g. excitations from n=2 are termed L-edge, etc.). XAS experiments can be broadly categorized into two classes. Studies probing the region from the absorption onset to several tens of eV above the edge are typically referred to as Near-Edge X-ray Absorption Fine Structure (NEXAFS) or X-ray Absorption Near Edge Structure (XANES) and probe the unoccupied bound states accessible to the target atom.[9] Within the dipole approximation, it may be said that K-edge NEXAFS spectra reflect the p-projection of the local unoccupied density of states. Experiments probing above this

energy, sometimes to as much as 1000 eV above the absorption edge, are termed Extended X-ray Absorption Fine Structure (EXAFS) and probe the local structural environment of the target atom.

a. NEXAFS/XANES

Near-edge XAS experiments probe excitations from core levels to the unoccupied energy levels accessible to the target atom, producing both an excited electron and a core hole. Relaxation of the core-excited atom can take place radiatively, through the emission of a fluorescent photon, or non-radiatively via the emission of an Auger electron. The processes involved in excitation and de-excitation are illustrated in Figure 1.

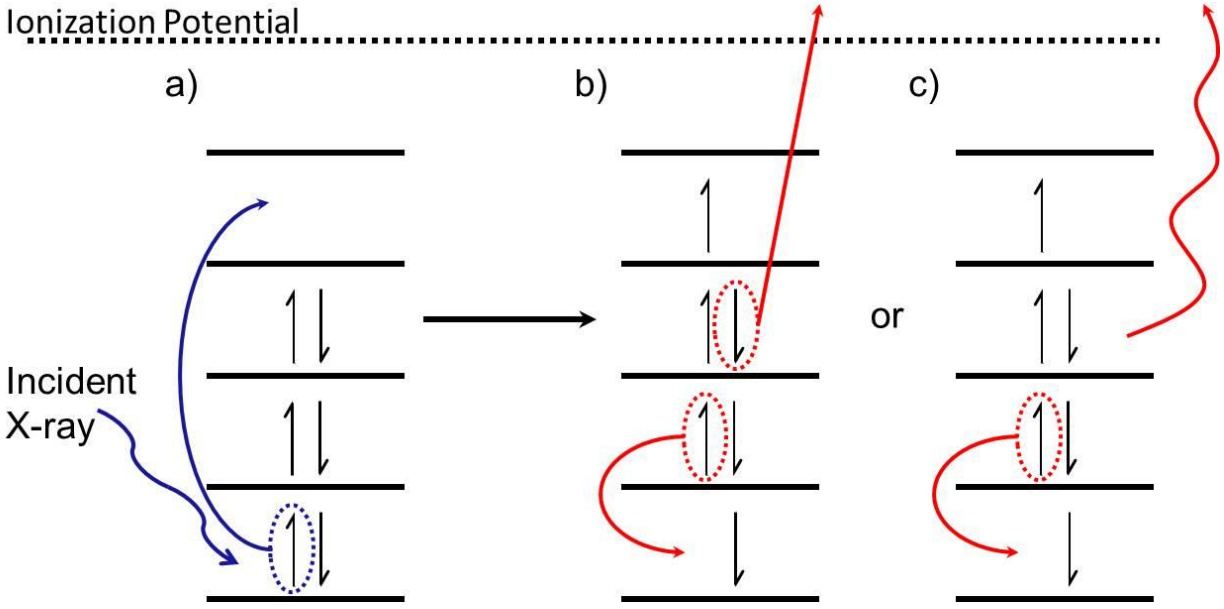

Figure 1: NEXAFS-relevant electronic transitions: a) Absorption of an X-ray photon results in excitation of a core electron into an unoccupied valence state. b) Non-radiative relaxation occurs via the Auger process. c) Radiative relaxation occurs via emission of a fluorescent X-ray photon. As depicted in these energy-level diagrams, relaxation of the excited electron is slow relative to relaxation of the core hole.

A variety of detection schemes can be employed for measurement of NEXAFS spectra, exploiting both emission pathways. The first fluorescence detection of a NEXAFS spectrum was reported by Fischer *et al.* in 1986 and utilized a gas proportional counter to detect the fluorescent signal.[10] In the years that followed, fluorescence was often measured by the larger, liquid nitrogen-cooled solid-state detectors that had been utilized for some decades for detection of X and γ radiation from radioactive isotopes (e.g. Si(Li), Ge(Li), drifted silicon, etc.), which offered the advantage of excellent energy resolution when properly maintained. All of these detection apparati typically employ windows of varying chemical composition to filter out low-energy photons that may have reached the detector as a result of scattering processes or from external sources.[9] Modern studies measuring fluorescence yield, however, tend to utilize semiconductor photodiodes. These simple detectors are small and do not require cryogenic cooling, making them much easier to incorporate into experimental designs. However, they do not energy-resolve

the incident photons and are also sensitive to photons with energies in the visible and UV ranges. While the quantum efficiency of such devices increases with photon energy, and substantially larger currents are observed at X-ray energies relative to the visible and UV,[11] photodiodes generally produce XA spectra with larger but generally constant backgrounds relative to energy-resolved detection devices. Because photodiodes do not discriminate photon energies, data collected with such detectors are typically referred to as total fluorescence yield (TFY) spectra.

While energy-resolved fluorescence yield XA spectra tend to have very low background and therefore offer an excellent signal/background ratio, they often do not exhibit high signal/noise as a result of low total signal strength. For core-excited low-z elements, the Auger relaxation pathway dominates, as shown in Figure 2; for example, the average fluorescence quantum yield of carbon following K-edge excitation has been measured to be 2.8×10^{-3}.[12] An additional complication for fluorescence yield spectroscopy arises in part because of this low quantum yield: state-dependent variation in the relative yield of fluorescent photons is large relative to the average quantum yield, potentially distorting fluorescence-yield spectra in favor of spectral features resulting from transitions into states with high fluorescence quantum yield.[13,14] Furthermore, as the fluorescent X-ray photons have energy only slightly below that of the incident beam, they have a similar attenuation length. Consequently, any resonant absorption events occurring within the sample may, in principle, result in fluorescent emissions that may reach the detector and be recorded. For samples with a path length enabling near-complete absorption of the incoming beam – only hundreds of nanometers around edge resonances[15] – this results in substantial saturation effects in the TFY spectrum. Self-absorption errors have also been observed.

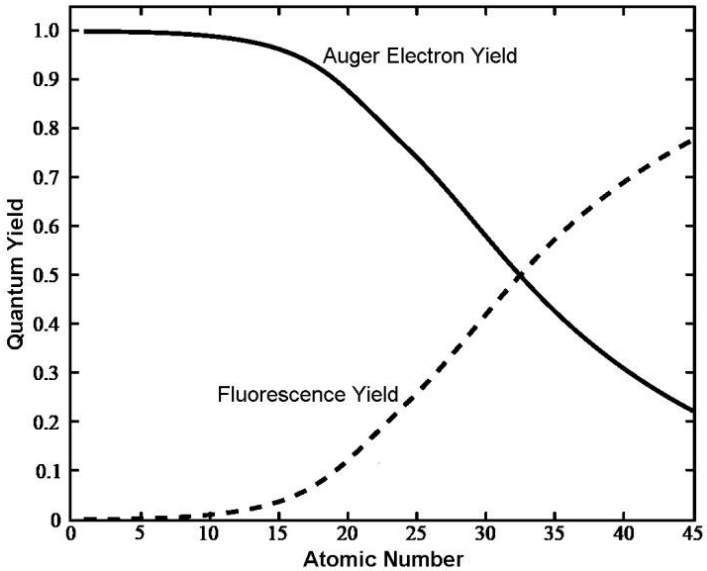

Figure 2: Quantum yields of Auger electrons and fluorescent X-rays per core-excited atom. For second-row elements Auger yield represents > 99% of relaxation events.

In recent years, a technique known as inverse partial fluorescence yield (iPFY) has been developed to enable fluorescence detection without the interference of saturation and self-absorption effects and state-dependent spectral intensity fluctuations.[16,17] In this technique, partial fluorescence yield is measured at a non-resonant wavelength, typically several 10s of eV below the resonant edge fluorescence energy. As absorption events attenuate the beam and

reduce the potential for non-resonant scattering, resonant absorption results in a reduction in the iPFY signal. It has been shown that the iPFY signal is inversely related to the absorption coefficient, and that the inverse iPFY spectrum matches well with electron detection experiments.[16] The sensitivity of iPFY detection closely matches that of PFY detection while minimizing the effects of saturation and state-dependent effects; however, both techniques exhibit reduced sensitivity relative to TFY.

While electron escape depths of 10s of Angstroms represent a substantially shallower probe depth than that measured via fluorescence yield, TEY still constitutes primarily a bulk measurement. It is possible to increase surface sensitivity by energy-filtering the detected electrons. With each subsequent scattering event, the Auger and secondary electrons become greater in number and lower in energy; the TEY signal is largely dominated by the numerous low-energy electrons generated by Auger emission events initiated deep within the sample.[9] By collecting only the higher-energy electrons, a detection approach referred to as partial electron yield (PEY), it is possible to isolate signal from electrons having undergone a small number of scattering events; such electrons will generally have originated near the sample surface. PEY spectra have most commonly been measured by placing a screening grid with a negative bias between a sample and a simple electron multiplier. The negative bias of the grid, often referred to as the retarding bias, blocks electrons with kinetic energies below the grid potential from reaching the detector; thus, a retarding bias of 200 V would allow passage and subsequent detection of electrons leaving the sample with KE > 200 eV. Typical retarding biases are 30-80 eV below the characteristic Auger electron energy of the atom being probed. A comparison of a PEY spectrum obtained using this type of detector, with a retarding bias ~40 V below the Auger energy, with a fluorescence yield spectrum of ethylene chemisorbed on a Cu(100) crystal is exhibited in Figure 3. This comparison makes it clear why PEY has generally been preferred to fluorescence yield for the study of low-z species adsorbed to solid substrates: while the signal/background ratio is vastly superior for fluorescence yield, the signal/noise is substantially better in the PEY spectrum. PEY spectra can also be measured using a standard electron energy analyzer such as a channeltron or hemispherical energy analyzer and integrating only the desired range of electron energies.[23,24]

An additional class of electron detection, also illustrated in Figure 3, is Auger electron yield (AEY). Unsurprisingly, AEY XA spectra measure electrons with a very narrow energy range around an Auger emission energy of the target atom. Typically, such spectra are collected via a cylindrical mirror analyzer (CMA) with its acceptance window centered on the desired Auger energy. The poor signal/noise evidenced in Figure 3 for this detection method is largely a result of a shorter count time – given equal counting time, AEY spectra of adsorbed species generally exhibit superior signal/noise relative to fluorescence yield detection due to the greater quantum yield of Auger electrons.[10] The probe depth for such experiments is determined by the mean free path of the Auger electron, ~1 nm in condensed phase media, providing greatly enhanced surface sensitivity relative to other methods. However, due to the fixed and typically short focal length and high vacuum requirements for the operation of CMAs, this detection mechanism has generally been perceived to be incompatible with liquid samples.

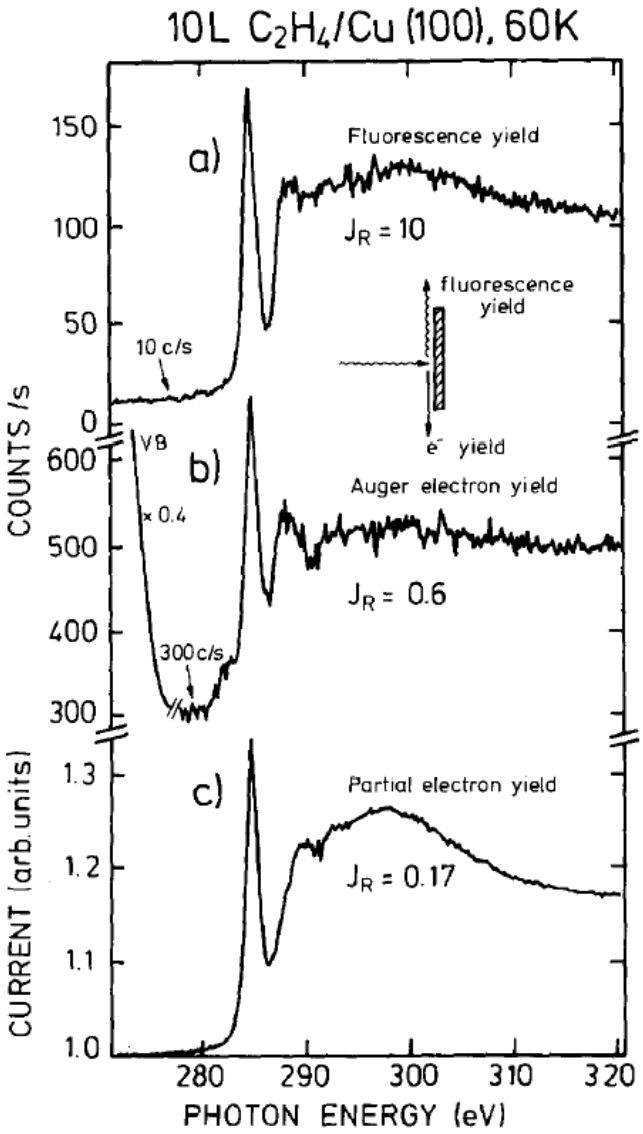

Figure 3: NEXAFS spectrum of ~2 monolayers of ethylene adsorbed on the (100) surface of a copper substrate as measured by a) fluorescence yield collected in a gas proportional counter b) Auger electron yield collected in a cylindrical mirror analyzer and c) partial electron yield collected with a 220 V retarding bias. All spectra are normalized to the spectrum of clean Cu(100) measured via the corresponding method. The listed J_R values correspond to the signal/background ratios (measured at 320 eV). Reproduced from D. Fischer *et al.*, "Carbon K-Edge Structure of Chemisorbed Molecules by Means of Fluorescence Detection." *Surf. Sci.* **1986**, *177* (1), 114–120.

Two additional classes of NEXAFS detection merit discussion. The first is ion yield detection. Auger electron emission and the subsequent cascade of secondary electrons produce local pockets of positive charge. This results in the expulsion of ionized species, which can be detected as an ion yield. Ion yield NEXAFS spectra have been recorded for gases,[25] adsorbed molecules on solids,[26] and liquids.[3,27] It is suggested in these works that ion yield detection may be the most surface sensitive NEXAFS detection technique as a result of the very short mean free

path of ionic species in condensed phase. However, it has been demonstrated that ion yield spectra of adsorbed species do not produce a spectrum linearly proportional to the absorption coefficients of the target atom in the spectral range.[28,29] Moreover, while ions must be generated near the vacuum interface to escape and be detected, contributions of ions produced by secondary ionization events following initial excitation and Auger emission within the bulk have been found to dominate the spectrum of solid ice,[30] and further experimentation has shown the ion yield and electron yield spectra of liquids to be generally indistinguishable.[31]

The final detection scheme for NEXAFS spectroscopy, which has become increasingly relevant to the study of liquids in recent years, is transmission mode detection. This is the most straightforward detection method for any absorption spectroscopy. However, as a result of the small mean free path of soft X-rays in sample media, it is primarily useful in the study of thin films,[32] or more recently in the study of very thin liquid samples, which will be discussed in greater detail in this work.

b. EXAFS

Whereas NEXAFS probes the unoccupied bound states of a target atom, thereby providing information on the local *electronic* environment, EXAFS produces excitations into the continuum, producing photoelectrons and probing the local *structural* environment. As production of an X-ray photoelectron generates a core hole which may relax via the same Auger or fluorescence pathways accessible to core-excited atoms following excitation into bound states, EXAFS spectra can be collected using the same suite of measurement techniques employed for NEXAFS. When displayed on signal vs. energy coordinates, as is typical for NEXAFS spectra (e.g. Figure 3), EXAFS spectra appear as low-amplitude oscillations in the signal intensity in the slowly-decaying baseline typically observed at energies above an absorption edge (Figure 4). The origin of these oscillations is interference between the wavefunctions of photoelectrons and backscatter from nearby atoms.

Extraction of structural information from EXAFS spectra requires conversion from energy coordinates to momentum coordinates, typically expressed in terms of the photoelectron wave vector *k*

$$k = \sqrt{\frac{2m}{\hbar^2}(E - E_0)} \qquad (1)$$

where E_0 is the ionization threshold. The signal intensity is background-subtracted, typically by removal of a constant background measured from the pre-edge region. The oscillation intensity $\chi(k)$ is then obtained by normalization to an isolated atomic background μ_0:

$$\chi(k) = \frac{\mu - \mu_0}{\mu_0} \qquad (2)$$

This atomic background can be obtained from experimental measurements or from a simple long-range fitting of the EXAFS spectrum over many oscillations. Plots in k-space are often displayed with $\chi(k)$ multiplied by a power of k (typically k^2 or k^3) to visually amplify the lower-amplitude oscillations at higher values of k.

The "EXAFS Equation" can be derived from Fermi's Golden Rule with consideration of perturbations resulting from the backscatter interference. While exact statements of the EXAFS

Equation vary slightly with the formalism used (e.g. plane wave vs. curved wave, single-scattering vs. multiple scattering, etc.), the common form of the equation is:

$$\chi(k) = \sum_j \frac{N_j f_j(k)}{kR_j^2} e^{-2k^2\sigma_j^2} \sin\{2kR_j + \varphi_j(k)\} \qquad (3)$$

Here N_j is the number of nearest neighbors, $f_j(k)$ is a decreasing amplitude function, R_j is the interatomic separation, φ_j a phase shift function arising from the atomic potential, and σ_j is the Debye-Waller factor. This final term is a measure of the structural disorder in the sample, proportional to the mean-squared fluctuation of symmetry-equivalent values of R_j. Consequently, the exponential term of the EXAFS equation describes a function reducing in amplitude at higher momentum at a rate proportional to the disorder in the local structure resulting from increasingly destructive interference patterns arising from neighbors at differing radial separation. Consequently, the rates at which the magnitude of EXAFS oscillations decay indicate the degree of disorder in the local structure.

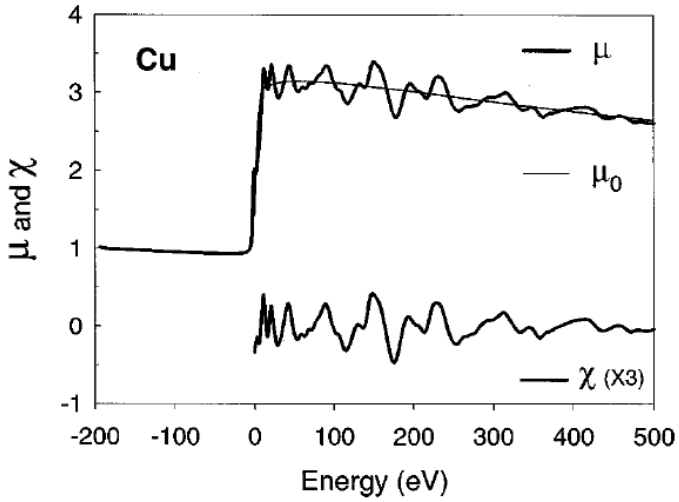

Figure 4: Raw EXAFS spectrum (μ) at the copper K edge of a single copper crystal showing the smooth atomic-like absorption background μ_0 and χ, in this case shown in energy coordinates as $\chi(E)$. The zero of the energy axis has been set to the ionization onset energy. Reproduced from J. J. Rehr & R. C. Albers, "Theoretical Approaches to X-Ray Absorption Fine Structure." *Rev. Mod. Phys.* **2000**, *72* (3), 621–654.

While reasonable values for some of the unknowns in Equation 3 can be extracted from the experimental data, fitting of raw $\chi(k)$ data is challenging due to the typical complexity of the spectra. The basis of the modern solution to this problem was developed in 1971 by Sayers et al: by computing the Fourier transform of $\chi(k)$, they demonstrated that it is possible to extract a plot in terms of radial distance to scattering atoms.[33] Back-transforming a single peak from this spectrum produces a simpler EXAFS spectrum in k-space, for which Equation 3 can be solved to find the number of atoms and Debye-Waller factor for neighbors at the distance from the target atom of the back-transformed peak.

More detailed discussion of the derivation and solution of the EXAFS Equation for various formalisms can be found in the literature.[19,34–39] At present, most EXAFS data processing and interpretation is performed in a generally straightforward – albeit not trivial in many cases –

manner, utilizing one of several pre-programmed packages that are readily available with varying user inputs. A list of common programs for EXAFS processing, including short descriptions and links, can be found at *http://www.ixasportal.net/wiki/Software*.

c. Scattering Techniques

While they do not truly fit into the category of XAS techniques, it is necessary to briefly mention X-ray and electron scattering techniques because of their modern applications to similar problems. Experiments utilizing inelastic X-ray scattering, often referred to as X-ray Raman spectroscopy (XRS), typically measure the inelastic scattering energy loss at energies around an X-ray absorption edge – producing data analogous to those measured in NEXAFS experiments – or above it – producing data analogous to those measured in EXAFS experiments. It has been shown mathematically that for cases in which the momentum transfer is small relative to the inverse radial distribution of the ground state electrons (e.g. 1s electrons for K-shell scattering) – that is, cases in which the dipole approximation can be considered valid – XRS provides the same chemical and structural information available from XAS.[40] Studies of crystalline substances by XRS have shown that it reproduces spectra measured by traditional NEXAFS[41] (Figure 5) and EXAFS[42] techniques for low-z atom types. Such experiments have the substantial benefit of offering an essentially free choice of input photon energies. As scattering cross-sections increase at higher photon energy, XRS studies are typically performed with hard X-rays, and consequently are not subject to the substantial difficulties associated with vapor background from liquid samples and limited penetration depth that make soft X-ray spectroscopy of liquids particularly challenging.[43] However, XRS experiments in the hard X-ray require collection and quantitative energy resolution of the scattered hard X-rays, often at $E > 10$ keV, and consequently tend to require substantially longer collection times and exhibit inferior spectral resolution compared to equivalent soft X-ray techniques. A thorough overview of the development and utility of the XRS technique through its early years has been published by Krisch and Sette.[44]

Inelastic electron scattering experiments at soft X-ray energies, typically referred to as inner shell electron energy loss spectroscopy (ISEELS) or simply EELS (which may also refer to the equivalent technique in the vibrational energy regime), can also probe information equivalent to that obtained from XAS and XRS experiments.[45] Experimental designs for ISEELS typically combine an "electron gun" with a high-resolution electron energy analyzer to map electron energy loss. However, while ISEELS has been utilized to study, for example, the water content of mineral species,[46] the requirement for HV or UHV pressures at the detector, typically short detector focal lengths, and poor electron penetration through window materials render bulk liquid samples incompatible with this technique.

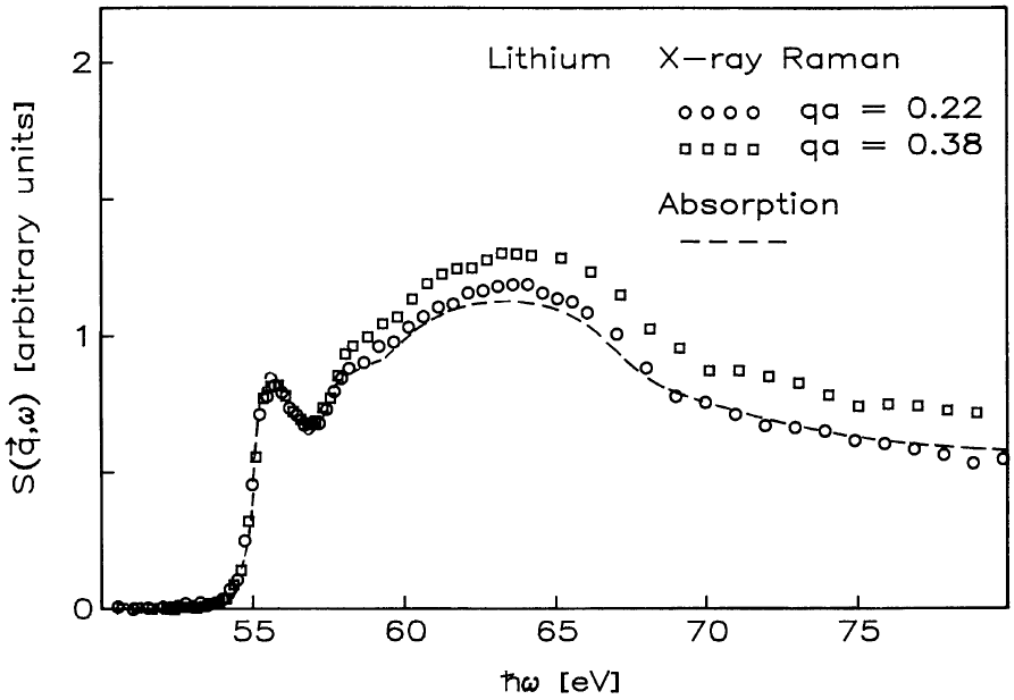

Figure 5: Comparison of XRS (empty points at several momentum transfer values) and NEXAFS (dashed line) spectra in the area of the lithium K-edge of solid lithium metal. In this figure, qa represents the product of the scattering momentum transfer q and the Li 1s inverse orbital radius a. It is clear that for low qa – that is, cases in which the dipole approximation is valid – the XRS spectrum reproduces the NEXAFS spectrum quite well, while for larger qa the breakdown of the dipole approximation results in greater discrepancies. Reproduced from H. Nagasawa*et al.*, "X-Ray Raman Spectrum of Li, Be and Graphite in a High-Resolution Inelastic Synchrotron X-Ray Scattering Experiment." *J. Phys. Soc. Japan* **1989**, *58* (2), 710–717.

III. Theoretical Interpretation of NEXAFS Spectra

XA spectra in the NEXAFS/EXAFS energy regimes contain a great deal of information on the electronic and structural properties of numerous chemical species. However, this information can only be extracted through comparison with appropriate theoretical calculations. While interpretation of EXAFS can be achieved by the straightforward solution of the EXAFS Equation for a given set of spectral data, interpretation of NEXAFS spectra is less straightforward and typically requires individual first-principles calculations on a system-by-system basis. For example, a study in our group of the TEY nitrogen K-edge NEXAFS spectrum of guanidinium ions in aqueous solution found that the LUMO and LUMO+1 states exchange upon core-excitation of a target nitrogen atom.[47] Such effects are not captured by a purely analytical computational approach. Instead, the standard approach to analysis of NEXAFS spectra combines molecular dynamics (MD) simulations of appropriately chosen model systems with electronic structure calculations – most commonly *ab initio* density functional theory (DFT)-based calculations[48,49] – to compute core excitation energies and intensities. A thorough and detailed overview of MD and electronic structure techniques utilized in such calculations has been recently published.[50] Here we will discuss briefly the specific challenges associated with

simulation of NEXAFS spectra of liquid systems and provide relevant details of the most commonly-utilized computational methods for such systems.

The first challenge in simulating liquid-phase NEXAFS spectra is the selection of appropriate molecular coordinates from which to compute the theoretical core-excitation spectrum. Because of the inherent disorder in liquid systems, it is necessary to representatively sample a large region of configuration space while modeling generally transient intermolecular interactions as accurately as is reasonably possible. Many calculations utilize molecular coordinates sampled from MD simulations of clusters, typically modeling transitions arising from ground states of atom(s) near the center of the cluster. Alternatively, a bulk liquid environment can be simulated in some cases by utilizing periodic boundary conditions. Many liquid studies have utilized fully classical MD simulations or quantum mechanics/molecular mechanics (QM/MM) simulations in which the central molecule to be excited, and in many cases its interactions with nearby solvent molecules, are treated quantum mechanically while the bulk liquid is treated classically. In addition, a number of simulated NEXAFS studies have utilized full *ab initio* molecular dynamics, particularly in the simulation of water,[51–54] including Car-Parrinello MD simulations[55] and path-integral *ab initio* MD simulations.[56]

Calculation of the simulated core-excitation spectrum from coordinates sampled from MD simulations has been performed within numerous methodologies. The simplest and least computationally expensive standard DFT method for simulating NEXAFS spectra is the so-called "muffin-tin approach," a single-electron multiple-scattering approach in which the excited states are modeled as dispersed within a potential field consisting of a spherical potential around nuclei and a constant interstitial potential. This method is analogous to the analysis of EXAFS spectra; indeed, muffin-tin calculations for the interpretation of NEXAFS spectra can be performed semi-quantitatively with the FEFF software package for EXAFS analysis.[37] This simple approach neglects the local electron density and core hole interactions; however, it has been found to be sufficient to reproduce the K-edge NEXAFS spectra of systems with highly delocalized excited states for which individual electronic interactions are less significant.[57,58] Note that newer versions of FEFF have been updated to include packages for NEXAFS analysis that combine multiple scattering with, e.g., core hole interaction estimates as described below.[59,60] A methodology utilizing a similar multiple scattering approach but employing an unconstrained potential field (i.e. free from the muffin tin approximation) has been published by Joly.[61]

The exponential growth in computational resources has enabled DFT-based methods of NEXAFS spectral analysis for realistic systems employing detailed approximations of the core-hole interaction and the local electronic structure of the final states. One such method which has been utilized substantially for liquid systems is Transition Potential DFT (TP-DFT).[62] This method is a philosophical descendant of the Slater Transition Potential Method of calculating electronic transition energies[63] in that it leverages an electronic configuration averaged between the ground and excited states. However, unlike the Slater method, which computes transitions on a state-by-state basis, TP-DFT typically removes half of a core electron from the atom of interest (for which reason it is often referred to as the Half Core Hole {HCH} Method), relaxes the generated molecular ion, freezes the resulting density and computes the full spectrum of excited states in a single calculation from the resulting potential. Consequently, this methodology is able to model directly the interactions of the core-excited structure and the excited electron.

Analogous methodology to the HCH TP-DFT method utilizing a full core hole (FCH) has also been explored.[51,64] Most commonly, the FCH is modeled using the z+1 approximation, in

which, rather than explicitly generating a core hole, the nucleus of the excited atom is replaced by the z+1 nucleus (i.e. a carbon target atom would be modeled as a nitrogen with 4 valence electron, effectively generating the same core charge as a carbon nucleus with a core hole). It has been suggested that this method is problematic for atom pairs wherein a substantial electronegativity gap between the two species exists, in which case enhanced local valence occupation due to the electronegative attraction for bonding electron pairs may substantially impact the relative weights of peaks in the observed spectrum.[65] Furthermore, it has been suggested that TP-DFT calculations may in general not be quantitatively accurate in reproducing the experimental NEXAFS spectra of liquids based on a random selection of coordinates,[66,67] although this claim has been contested.[5,6,68,69] The fact that the excited half-electron is ignored may also be problematic for systems in which the excited electron is fairly localized and/or interacts strongly with the unoccupied orbitals of the excited atom.[68]

The other analytical method which has been used effectively in the analysis of liquid-phase NEXAFS spectra is the Prendergast-Galli eXcited electron and Core Hole (XCH) methodology.[70] In this approach the excited atom is modeled with a modified pseudopotential to represent the presence of the core hole, and the excited electron is included explicitly in the first available valence orbital. The electron density of the first excited state is then calculated self-consistently. The remaining states are generated non-self-consistently from the unoccupied Kohn-Sham orbitals of the self-consistently generated field. Transition matrix elements to the computed states are calculated with in Fermi's Golden Rule within the dipole approximation. Whereas TP-DFT calculations are typically performed with an orbital basis set utilizing cluster-based sample systems, the XCH calculation utilizes a plane-wave basis. Consequently, calculations on clusters produce substantial non-physical edge effects; instead, coordinates must be generated under periodic boundary conditions. For small box sizes, this may result in non-physical boundary interactions.[7] Critics of the methodology have also pointed out that it may break down in cases for which the first excited state and higher-energy excited states differ substantially, and have also suggested that the non-self-consistent portion of the calculation – the orbitals for which are computed in the presence of the core-excited electron in the LUMO and thus with a net neutral charge rather than a positive charge – may be a poor model for insulating materials in which metallic charge-screening mimicking this effect would not be expected.[68]

NEXAFS spectra can also be computed via time-dependent DFT (TDDFT).[71] The accuracy of such methods has been found to vary substantially with system and choice of functional.[71,72] Only 2 thorough TDDFT studies of the NEXAFS spectra of liquids have been performed, both studying pure liquid water.[73,74] Brancato *et al.* calculated a spectrum with relative peak heights in poor agreement with experiment; however, Fransson *et al.* found that by utilizing larger clusters and multi-molecule averaging TDDFT produced a more quantitatively accurate reproduction of the experimental data than TP-DFT calculations on the same molecular coordinates, as exhibited in Figure 6.

All of the above computational methods simplify the two-body electron-core hole system into a single-body problem, typically by modeling the core hole via an appropriate pseudopotential for the core-excited atomic center. However, in recent years it has become possible to solve the two-body Bethe-Saltpeter equation (BSE) in conjunction with a plane-wave DFT treatment of the excited state and *GW* quasiparticle corrections to the self-energy to computationally address spectral broadening.[60,75–77] This methodology has been applied to water;[78] however, the system size was constrained to 17 water molecules by the computational costs of the theoretical methodology, and the calculated spectrum was not consistent with

experiment at high energies.[7] The computational method has recently been further streamlined for application to larger systems, but this more-efficient adaptation of the calculation has not yet been applied to liquid systems.[79]

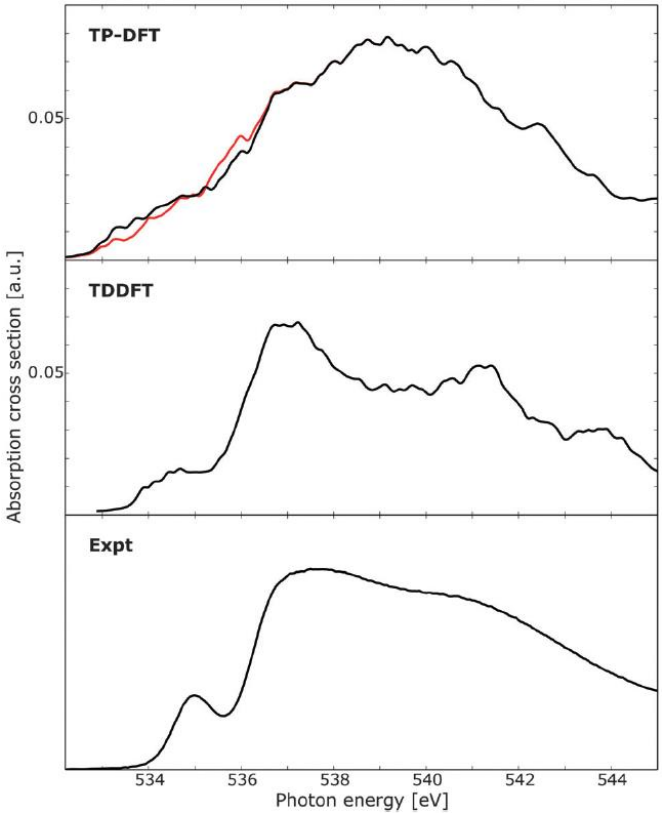

Figure 6: Comparison of simulated liquid water NEXAFS spectra obtained from TP-DFT and TDDFT to the experimental spectrum. Each theoretical spectrum is averaged over 100 sets of molecular coordinates; each set of coordinates consists of a cluster of 32 water molecules computed using PIMD. Here, the TDDFT calculated spectrum shows a better agreement with experiment, particularly in terms of the main edge (~537 eV) to post edge (~541.5 eV) peak ratio. This concept will be discussed in greater detail in the discussion of the water NEXAFS spectrum. Reproduced from T. Fransson *et al.*, "Requirements of First-Principles Calculations of X-Ray Absorption Spectra of Liquid Water." *Phys. Chem. Chem. Phys.* **2016**, *18* (1), 566–583.

IV. XAS of Water

The hydrogen bond structure of water has been the subject of extensive study as it underlies the remarkable properties of water in its condensed phases. The unique liquid properties of water are critical to its role in biological solvation and reaction dynamics, e.g. in the stabilization of native protein structure.[80] It has long been believed that liquid water at ambient temperature has a locally ordered tetrahedral structure with a small number of broken hydrogen bonds, allowing for tighter packing than that found in ice I_h.[81,82] Indeed, this picture has become "textbook knowledge" and has been supported by several experimental techniques. For example, Fourier Transform Infrared Spectroscopy (FTIR) studies have indicated a small number of

dangling hydrogen bonds at room temperature,[83,84] supporting a picture of liquid water in which most water molecules are donating and accepting two hydrogen bonds. Neutron[85] and x-ray scattering[86,87] results have been interpreted such that the extracted O-O radial distribution functions (RDFs) have a reasonably sharp second peak indicating an ordered and periodic structure relative to that of most liquids and with a separation between peak positions consistent with tetrahedral bond angles. First principles simulations of liquid water have also nearly universally supported the tetrahedral structure of water, with exceptions generally being ascribed to an incomplete basis set.[88] The tetrahedral picture of liquid water was nearly universally accepted until the development of techniques for NEXAFS spectroscopy of liquid water introduced new controversy into this old discussion, inciting passionate disagreements regarding the nature of liquid water at ambient conditions.

a. Liquid Microjet Experiments

The first XA spectrum of a liquid sample was an EXAFS spectrum of water published by Yang and Kirz in 1987.[89] The authors utilized a static water cell comprising two 150 nm silicon nitride windows surrounding a sample of thickness 1 um and a PMT detector in a transmission geometry. Transmission through the empty cell was ~20%. The resulting EXAFS spectrum matched qualitatively with the authors' calculated spectrum; however, the lack of an accurate amplitude function and phase shift for liquid water, combined with the poor spectral resolution available at the time, did not permit quantitative determination of the O-O pair correlation function and Debye-Waller factor.

The breakthrough in XAS of liquids occurred with the publication by Wilson *et al.* of the EXAFS and NEXAFS spectra of liquid water microjets in 2001.[3] Liquid microjet technology had been pioneered for Ultraviolet Photoelectron Spectroscopy (UPS) by Faubel et al in the late 1980s[90] and was adapted for use in XAS at Berkeley. Liquid microjets are formed by forcing pressurized liquids through a micron-scale opening, typically under laminar flow conditions with a linear flow velocity in the range 20-100 m/s. The streaming jet provides a continuously-renewing sample and avoids the substantial absorption losses from the windows observed in the static cell experiment of Yang and Kirz. For XAS experiments, the resulting liquid jet is intersected with the X-ray beam downstream from the jet tip. Any of the various detection apparati described above compatible with observed chamber pressures can be placed near the region of intersection. Differential pumping allows the X-ray beamline to be maintained at ultra-high vacuum while the local pressure at the liquid jet may be substantially higher (typical chamber pressures are 10^{-5} to 10^{-3} torr). As X-ray beam diameters are typically larger than liquid microjets, a background signal from the vapor jacket evaporating from the liquid jet is usually unavoidable for volatile samples, although the recent introduction of electrokinetic detection of the XAS spectrum by Lam *et al.* greatly reduces the vapor contribution to the measured signal.[91] A schematic diagram of the experimental chamber utilized in the earliest XAS studies of liquid water is shown in Figure 7, and a detailed experimental description can be found in Ref. 92.

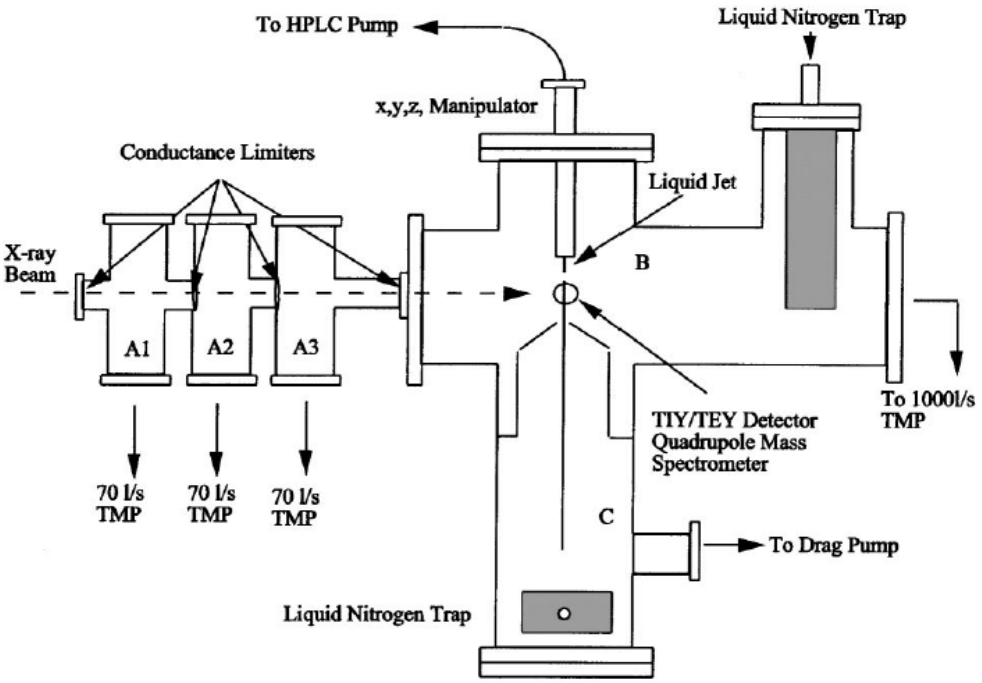

Figure 7: Schematic diagram of the Berkeley apparatus used to perform XAS of liquid microjets. This configuration allows pressures of ca. 10^{-4} torr to be reached in the main chamber and pressures of ca. 10^{-9} torr to be simultaneously maintained in the X-ray beamline. Reproduced from K. R. Wilsom *et al.*, "Investigation of Volatile Liquid Surfaces by Synchrotron X-Ray Spectroscopy of Liquid Microjets." *Rev. Sci. Instrum.* **2004**, *75* (3), 725–736.

Improvements to experimental and computational resources since the publication of Yang and Kirz, particularly in the resolution and brightness of synchrotron light sources, allowed Wilson *et al.* to fit the EXAFS spectrum of liquid water, exhibited in Figure 8. Utilizing a simple single-scattering formalism the authors found a nearest-neighbor O-O radius of 2.85 ± 0.05 Å, consistent with the values found from X-ray[87] and neutron[85] scattering studies. A later follow-up study found a similar value of 2.80 ± 0.05 Å.[93] These studies illustrated the power of the liquid microjet technique for studying liquid samples by soft X-ray absorption spectroscopy.

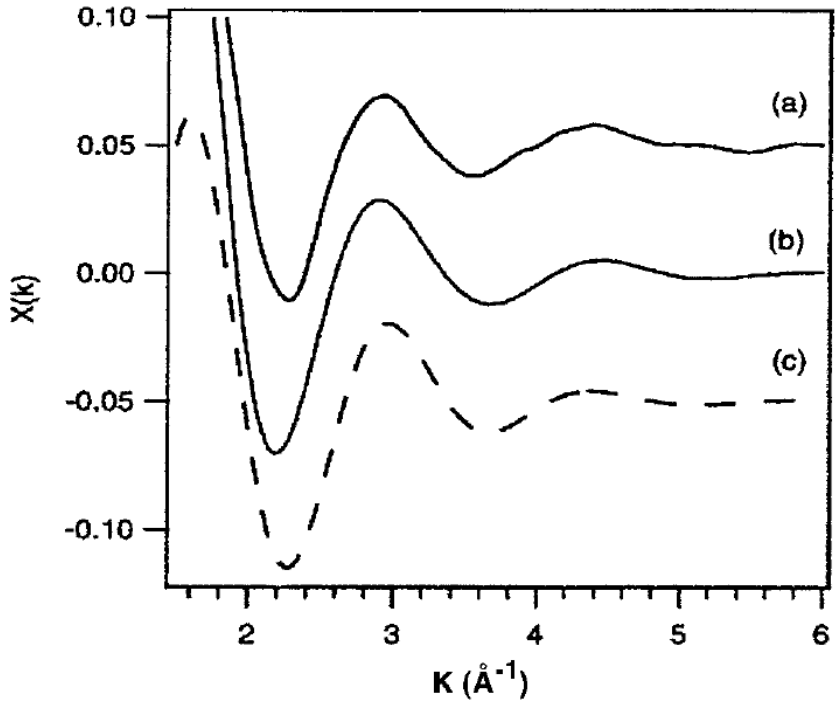

Figure 8: EXAFS spectrum above the liquid water oxygen K-edge measured using TEY detection and transformed into K-space. (a) Experimental data smoothed via a 5-point Savitzsky-Galoy smoothing algorithm. (b) Fourier-filtered experimental data. (c) Calculated spectrum of water assuming a fixed single O-O scattering distance, calculated to be 2.85±0.05 Å. Reproduced from K. R. Wilson *et al.*, "X-Ray Spectroscopy of Liquid Water Microjets." *J. Phys. Chem. B* **2001**, *105* (17), 3346–3349.

Ekimova *et al.* have recently reported the development of a liquid flatjet produced by collision of two liquid jets in air or vacuum.[94] As can be seen in the photographs of such a jet apparatus in Figure 9, under appropriate flow conditions this collision results in the formation of several orthogonal flat liquid sheets of roughly elliptical shape. The authors report that these sheets are stable over periods as long as hours and have fairly stable thickness of ca. 1 μm. This combination of long-term stability and thin sample path length render such sheets ideal for windowless transmission-mode XAS studies of liquid samples; several applications of this technique are presented in Ref. 94. As transmission-mode spectral detection avoids potential spectral distortions from absorption saturation, decay path yields, etc., this technology has the potential to open a valuable new class of XAS experiments on liquid samples. Additionally, the authors incorporated a sample recycling system similar to that of Lange *et al.*,[95] allowing for real-time re-use of the sample. While introducing an enhanced risk of contamination or radiative sample damage, this feature can prove helpful when working with expensive or difficult-to-synthesize liquid samples.

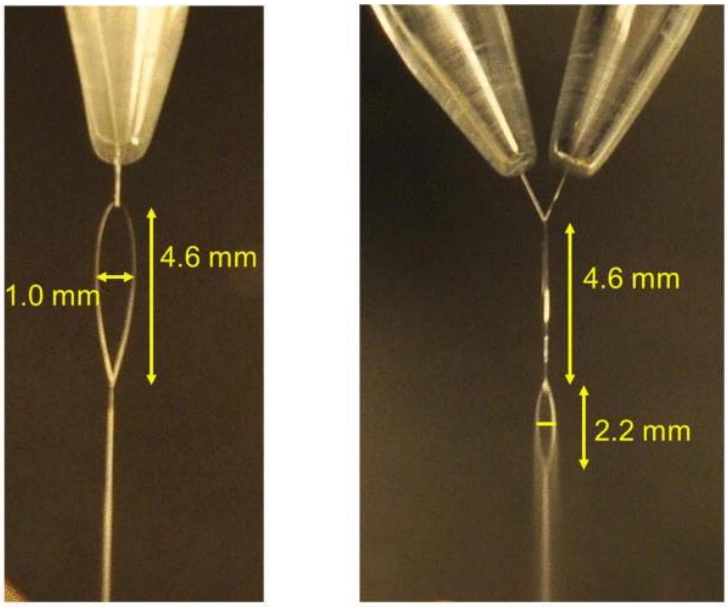

Figure 9: Two taken taken in (left) and perpendicular to (right) the plane of the collision of two liquid jets. This jet was produced by flowing the liquid sample at identical flow rates of ~6 mL/min through two identical capillary tips with inner diameter 50 µm. The initial elliptical flat liquid sheet is formed perpendicularly to the plane of the collision. In this case the second liquid sheet can be seen breaking into droplets. Reproduced from M. Ekimova *et al.*, "A Liquid Flatjet System for Solution Phase Soft-X-Ray Spectroscopy." *Struct. Dyn. (Melville, N.Y.)* **2015**, *2* (5), 54301.

b. Liquid Flow Cell Techniques

Shortly after the introduction of liquid microjet technology into soft XAS by Wilson *et al.*, flow cells emerged as an alternative method of sample delivery for liquid XAS experiments. The first flow-cell based liquid XAS experiment was published by Freiwald *et al.* in 2004.[96] Their apparatus, diagrammed in Figure 10a, consisted of a liquid chamber with input and output tubing allowing liquid samples to be pumped through. Incident X-rays enter and fluorescent photons escape to the detector via a single 150 nm thick silicon nitride window. X-Ray transmittance through such windows generally increases through the soft X-ray energy regime, ranging from 0.1 at 200 eV to 0.96 at 1600 eV.[96]

Several additional flow cell designs for XAS of liquids utilizing silicon nitride windows of 100-150 µm thickness have been introduced since the cell of Freiwald *et al.*[97–104] Like liquid microjets, flow cells have the advantage of providing a sample which can be renewed without the need to break vacuum and remove the sample mount. However, the sample renewal is much slower than that of microjet experiments as a result of the requirement that the pressure forcing the liquid through the cell not burst the thin windows. Furthermore, the silicon nitride window introduces a solid interface to the sample that does not exist in liquid microjet experiments. On the other hand, flow cell experiments remove the risk of freezing that is present with liquid jets and thus are generally more robust than microjet experiments. Most can be performed without the gas phase background observed in microjet XA spectra.

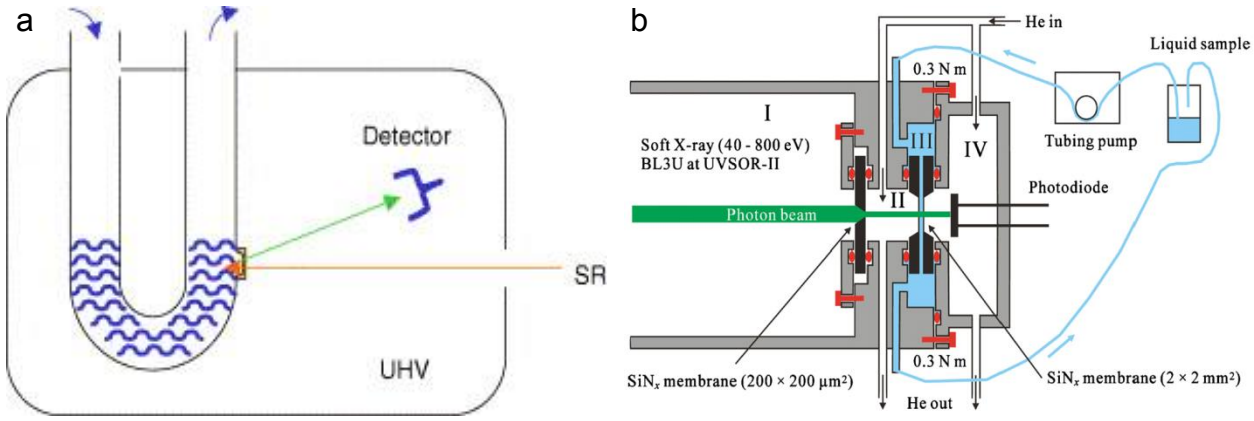

Figure 10: Schematic diagrams of several liquid flow cell apparatus used for XAS experiments. a) A single window photon-in/photon-out flow cell for TFY experiments. Reproduced from M. Freiwald *et al*., "Soft X-Ray Absorption Spectroscopy in Liquid Environments." *J. Electron Spectros. Relat. Phenomena* **2004**, *137–140*, 413–416. b) Variable-thickness dual-window flow cell for transmission mode experiments. Reproduced from M. Nagasaka *et al.*, "Development of a Liquid Flow Cell to Measure Soft X-Ray Absorption in Transmission Mode: A Test for Liquid Water." *J. Electron Spectros. Relat. Phenomena* **2010**, *177* (2–3), 130–134.

Various cell designs have been employed to introduce different experimental elements. For example, some are designed for active temperature control,[100,102] with two parallel windows to allow for transmission studies,[97,98,101,102] or even to study liquids at solid interfaces.[99,103,104] Several cell designs allow for XA spectroscopy to be conducted simultaneously with electrochemical cycling.[103–107] Figure 10b illustrates the cell design of Nagasaka *et al.*, a variable-thickness flow cell with two parallel silicon nitride windows for transmission detection.[97] As illustrated in the figure, the windows are sealed externally to the flow cell via o-rings (pictured as red circles in cross section). The windows are separated by spacers outside the o-rings relative to the central interaction region. This arrangement allows sufficient flexibility to modulate sample thickness *in situ* by changing the pressure of the helium in regions II and IV and maintain the desired total absorption through the sample without removing the cell from vacuum to change out a spacer. On the other hand, the dual-window transmission cell of Meibohm *et al.* utilizes rigid gold spacers to maintain a well-defined sample thickness of 500 nm.[102]

c. Interpreting the Water NEXAFS Spectrum

The oxygen K-edge NEXAFS spectrum of water, initially reported by Wilson *et al.*, has since been replicated by numerous methods and is well-established.[3,24,55,93,97,98,100–102,108–110] Spectra measured with various detection methods are exhibited in Figure 11. From this comparison it is clear that the general spectral features are consistent from method to method. The resolution of XRS experiments is substantially inferior to that of the NEXAFS methods (~0.5-1 eV vs. ~0.1 eV). The intensity of ratios of the spectral features appear to differ in AEY from the other techniques. The origin of this anomaly is unclear; while AEY is believed to represent the spectrum of interfacial molecules even in a bulk sample, the experiment providing the data for this spectrum was also performed on the so-called 'pre-melted' water, a thin layer of

liquid known to exist at the surface of ice in an atmosphere of water vapor.[24] This sample may not exhibit the same structural characteristics of the bulk water samples used for the other detection methods.

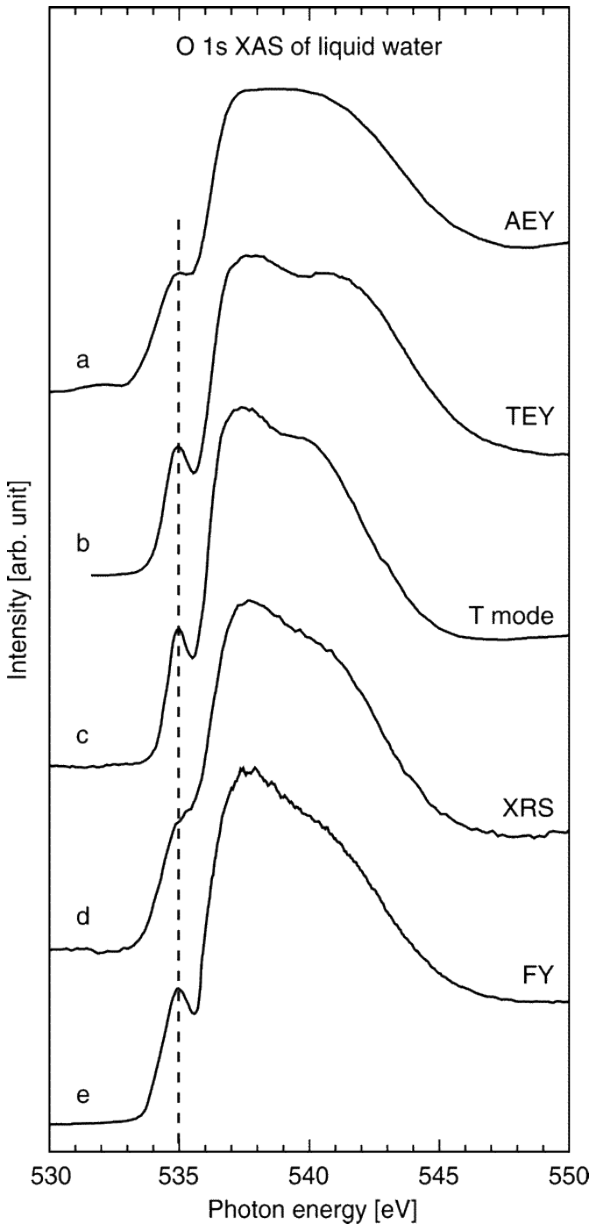

Figure 11: Comparison of oxygen K-edge NEXAFS spectra of water measured via a variety of detection methods: a) AEY b) TEY c) transmission mode d) XRS and e) TFY. Spectra are area-normalized to the full spectral width available in all 5 spectra; that is, from 532-550 eV. They have also been energy aligned to place the pre-edge feature at 535 eV. In addition, the TFY spectrum has been corrected for saturation effects as described in Ref. [111]. Reproduced from , L.-A. Näslund *et al*., "X-Ray Absorption Spectroscopy Measurements of Liquid Water." *J. Phys. Chem. B* **2005**, *109* (28), 13835–13839.

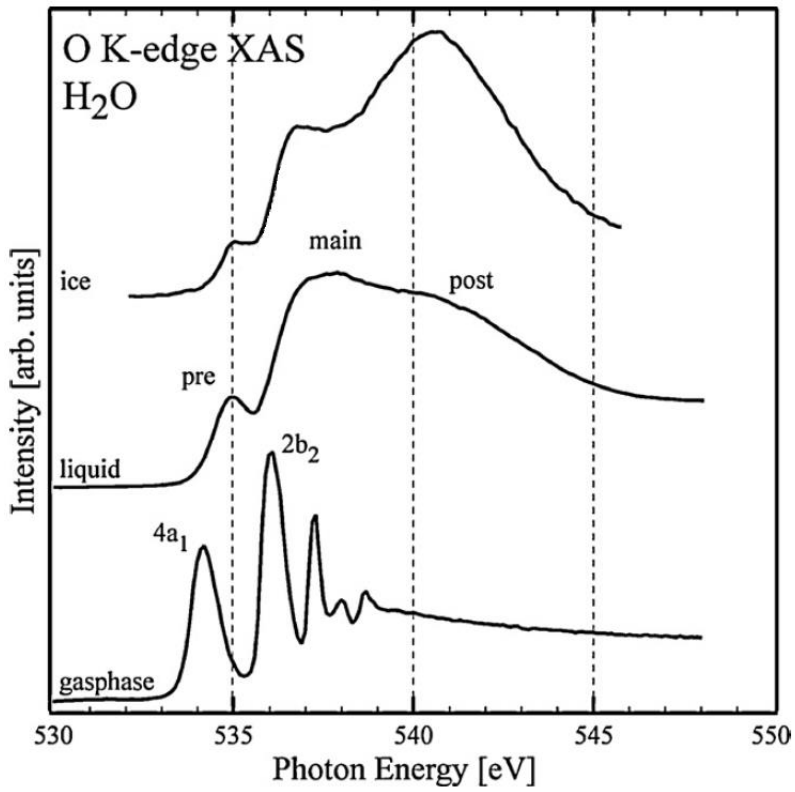

Figure 12: Comparison of the oxygen K-edge NEXAFS spectra of liquid water to gas phase water vapor and ice I_h indicating the spectral regions comprising the pre-edge, main edge, and post-edge of the liquid water spectrum. Adapted from A. Nilsson *et al.*, "X-Ray Absorption Spectroscopy and X-Ray Raman Scattering of Water and Ice; an Experimental View." *J. Electron Spectros. Relat. Phenomena* **2010**, *177* (2–3), 99–129.

The water spectrum exhibits three distinct spectral features, highlighted in Figure 12: a small pre-edge feature around 535 eV and larger main edge (centerered between 537 and 538 eV) and post-edge (centered between 541 and 542 eV) features. It was proposed by Cavalleri *et al.* in 2002 that the pre-edge feature intensity was related to the number of broken hydrogen bonds, as DFT calculations indicated that broken hydrogen-bond donor sites result in asymmetry that enhances the p-character of the $4a_1$ state and increases the oscillator strength of transitions from the oxygen 1s.[112] This suggestion is reinforced by the fact that the pre-edge feature is weaker or nonexistent in oxygen K-edge NEXAFS spectra of ice and has since been generally accepted.[56,113,114] Similarly, the post-edge feature has been attributed to highly-coordinated long-range tetrahedral structure and is stronger in ice than liquid water.[55,112] Moreover, time resolved core-excitation decay studies have indicated that the final state corresponding to the pre-edge feature is fairly localized, whereas the final state corresponding to the post-edge feature is highly delocalized.[115]

Substantial controversy exists as to the hydrogen bond structure of liquid water implied by the peak ratios observed in the oxygen K-edge spectrum of liquid water. Wernet *et al.* proposed in 2004 that the spectrum could only be explained by a liquid structure in which most of the water molecules only made two strong hydrogen bonds, one donated and one accepted.[55] Such a hydrogen bond structure results in the one-dimensional "rings and chains" structural

motif, entirely at odds with the traditional picture of liquid water as a three-dimensional quasi-tetrahedral liquid at room temperature. These conclusions and the quantitative validity of the associated theory were quickly questioned in the literature,[113,116,117] and the structure of liquid water has continued to be the subject of vigorous debate.[5,6,22,52,67,68,118–122] Kühne and Khaliullin have proposed an intermediary theory in which the average molecule in liquid water is in a structurally symmetric environment (that is, donating and accepting two strong hydrogen bonds), but high-frequency structural fluctuations result in significant instantaneous energetic asymmetry between symmetry-equivalent bonding sites.[114] The implications of the NEXAFS spectrum of water on the understanding of the hydrogen bond structure of liquid water have been recently reviewed in greater detail in Ref. 7.

d. Perturbing the Hydrogen Bond Structure of Liquid Water

The understanding of the spectral features exhibited in the oxygen K-edge NEXAFS spectrum of liquid water has been enhanced by studies of water under conditions for which the hydrogen bonding network has been intentionally altered, e.g. by changing the temperature of the sample or introducing defects into the liquid water matrix. Several studies of the temperature dependence of the liquid water spectrum have been carried out spanning a temperature range from supercooled to supercritical.[54,55,102,109,123] While Wernet *et al.* and Smith *et al.* disagreed on the rearrangement energy to break a hydrogen bond and adopt an asymmetrical configuration,[55,109] the spectral signatures observed upon temperature change are consistent across all studies. As temperature increases, the post-edge intensity decreases, the pre-edge intensity increases, and the entire spectrum shifts to lower energy; these effects are illustrated in Figure 13 for the temperature range 1.5-39 °C. Based on the standard interpretation of the spectral regions, these changes are consistent with an increase in broken hydrogen bond donor sites and a decrease in long-range tetrahedral order as temperature increases. Alternatively, increasing the pressure results first in a decrease in pre-edge intensity, suggesting a reduction of dangling hydrogens, followed by an increase in pre-edge intensity above 0.3 GPa, perhaps indicating that the structure becomes too compressed for tetrahedral ordering at higher pressures.[124]

Lange *et al.* have demonstrated a similar spectral effect to that of increasing the temperature by diluting water with acetonitrile, a polar organic solvent that accepts but cannot donate hydrogen bonds.[125–127] Indeed, at 5 volume % water, the pre- and main edges of the water spectrum closely resemble a simple blue shift to the $4a_1$ and $2b_2$ peaks of gas phase water. The pre-edge is still reduced in intensity relative to the gas phase $4a_1$ peak, consistent with previous findings indicating that even at very low water concentration in acetonitrile many water molecules form 2-3 strong hydrogen bonds;[128] however, the existence of a strong pre-edge enhancement indicates that acetonitrile may not actually be acting as a strong hydrogen bond acceptor in these mixtures. Additional studies have found this effect to be highly solvent-dependent.[125,129] For example, at similar concentrations, 3-methyl-pyridine acts as a strong hydrogen bond acceptor, and while the spectrum of 10% D_2O in acetonitrile closely resembles that of H_2O in acetonitrile, the spectrum of 10% D_2O in 3-methyl-pyridine much more closely resembles that of neat water with a reduced post-edge intensity.[129] Water at very low concentrations in non-polar solvents such as benzene and chloroform exhibits the spectral characteristics of highly-coordinated ice-like structure, indicating strong aggregation within the hydrophobic solvent, and in the case of benzene, possible formation of clathrate-like solvent

traps.[125] Having noted a heavy water experiment here, it is also notable that Bergmann *et al.* have reported that the NEXAFS spectrum of D_2O resembles that of H_2O at a temperature ~20 K lower; that is, isotopic substitution to heavy water results in a spectrum that is blue shifted and exhibits a slightly enhanced post-edge and reduced pre-edge relative to H_2O.[130]

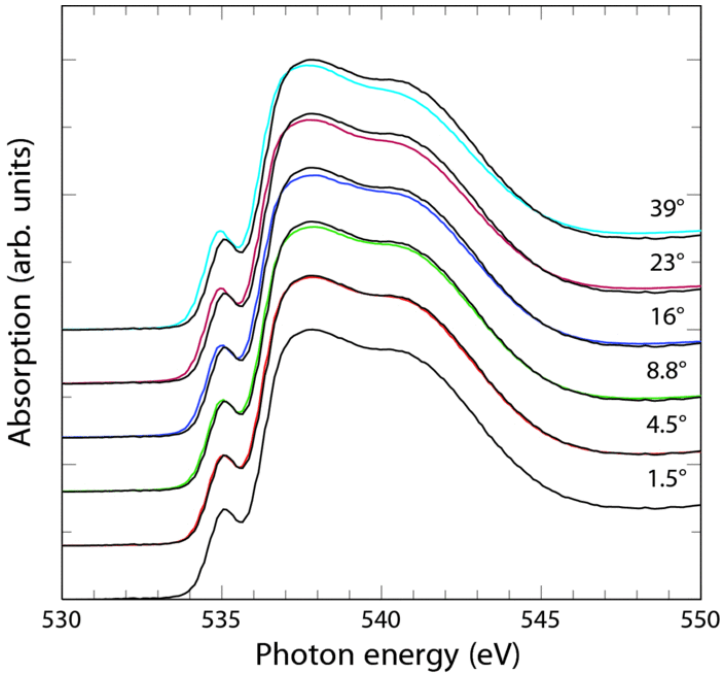

Figure 13: Temperature dependence of the oxygen K-edge NEXAFS spectrum of liquid water. All black spectra are reproductions of the 1.5° spectrum to illustrate spectral changes. All spectra were collected in transmission mode using a temperature-controlled flow cell with temperature resolution of ±0.25 °C and have been area normalized. Reproduced from J. Meibohm *et al.*, "Temperature Dependent Soft X-Ray Absorption Spectroscopy of Liquids." *Rev. Sci. Instrum.* **2014**, *85* (10), 103102.

A related clustering effect to that observed for low concentrations of water in hydrophobic solvents has been observed for thin films of water on solid substrates. Nordlund *et al.* found that while isolated water molecules adsorbed on Ru(001) exhibited an oxygen K-edge NEXAFS spectrum largely indistinguishable from that of the gas phase, continued addition of water molecules resulted in an enhancement of the post-edge and reduction in the pre-edge, and at coverage approaching one monolayer, an ice-like spectrum was observed.[131] A similar interfacial spectral behavior has been observed for bulk water at a gold interface.[104] Velasco-Velez *et al.* utilized an electrochemical liquid flow cell with a ~20 nm layer of gold deposited on the 100 nm Si_3N_4 window and acting as the working electrode and current collector for TEY spectroscopy of the interfacial region. The NEXAFS spectrum of water at the gold interface, shown in Figure 14, was found to exhibit minimal signal in the pre-edge region at neutral or positive potential. This phenomenon has been attributed to electronic coupling of the core-excited state with the gold substrate rather than a lack of dangling hydrogen bonds. By applying a negative potential to the gold the authors were able to observe a normal water spectrum with the pre-edge feature intact, presumably resulting from a structural rearrangement to rotate water hydrogens toward the gold surface. The same spectral effect could be achieved by coating the

surface with a hydrophobic substrate and preventing the electronic coupling with interfacial water.

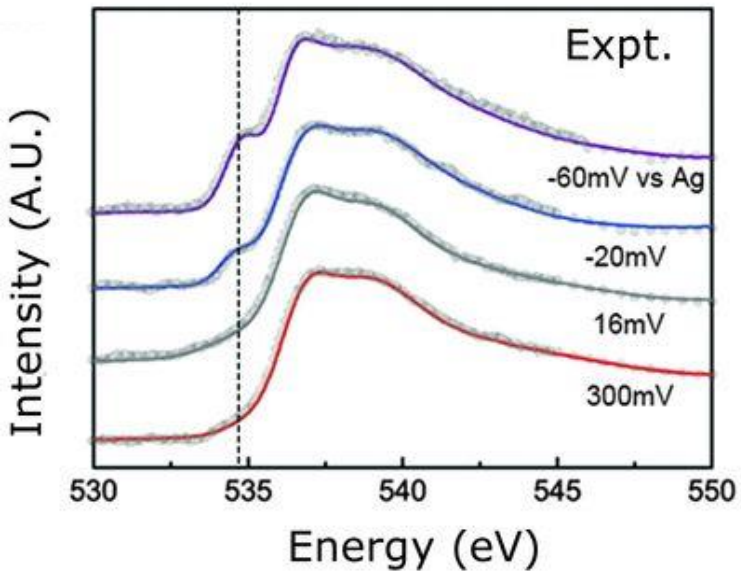

Figure 14: Oxygen K-edge NEXAFS spectrum of water at a gold interface measured by total electron yield for several surface potentials (relative to Ag). The dashed line indicates the position of the pre-edge feature of the liquid water spectrum. Reproduced from J.-J. Velasco-Velez *et al.*, "The Structure of Interfacial Water on Gold Electrodes Studied by X-Ray Absorption Spectroscopy." *Science (80-.).* **2014**, *346* (6211).

More subtle changes to the liquid water NEXAFS spectrum can be induced by the introduction of certain solutes into aqueous solution. Näslund *et al.* observed new peaks in the liquid water spectrum upon orbital mixing with the d orbitals of dissolved transition metals in salt solutions.[132] In the same work, the authors suggest the presence of a reproducible change to the water NEXAFS spectrum attributable to hydrogen bond rearrangement upon addition of salts. The first systematic study of such a phenomenon was published by Cappa *et al.* in 2005 and indicated linear increases in the intensity of the pre- and main edges and a linear decrease in the intensity of the post-edge feature with increasing concentration of sodium halide salts in a study of liquid microjet samples utilizing TEY detection (results shown in Figure 15).[66] In addition, a concentration-dependent red shift was observed for NaI solutions, a smaller red shift for NaCl solutions, and no meaningful shift for NaBr solutions relative to neat water. These changes are attributed primarily to local electronic perturbations from near-neighbor halide anions rather than substantial perturbation of the water hydrogen bonding network outside of the first solvation shell.[66,111] It has been alternatively suggested that iodide and sodium ions both contribute to disruption of the water hydrogen bond network, while chloride and bromide do not substantially alter hydrogen bonding.[69] Interestingly, utilizing a flow cell with TFY detection Guo *et al.* observed a small blue shift, rather than a red shift, for the sodium, magnesium, and aluminum salts of chloride;[133] the origin of this discrepancy is unclear.

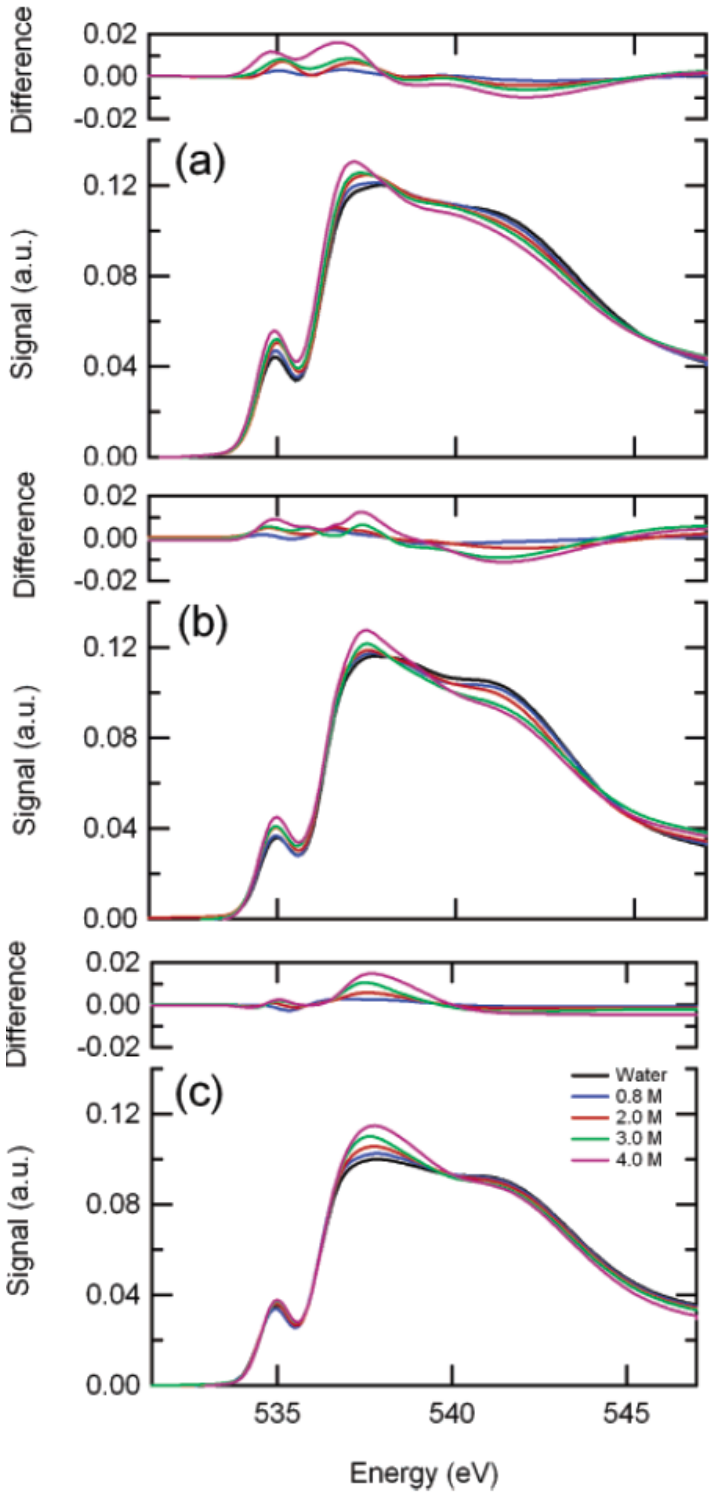

Figure 15: Oxygen K-edge NEXAFS spectrum of aqueous solutions of (a) NaI, (b) NaBr, and (c) NaCl. Spectra were collected via TEY of liquid microjets and have been area normalized over the spectral region 532-550 eV. Difference spectra between each solution and the neat water spectrum are shown at the top of each panel. Reproduced from C. D. Cappa *et al.*, "Effects of Alkali Metal Halide Salts on the Hydrogen Bond Network of Liquid Water." *J. Phys. Chem. B* **2005**, *109* (15), 7046–7052.

A substantial discrepancy in the observed impact on the water NEXAFS spectrum of monovalent cations has also been observed. Liquid jets of aqueous solutions of akali metal, ammonium, and guanidinium chloride salts, detected via TEY, revealed minimal differences between the solution oxygen K-edge spectra of the various salts.[134] Spectra of solutions of Li^+, Na^+, K^+, and NH_4^+ acetate measured in a single-window flow cell by TFY also exhibited no significant difference in the water spectrum between the cations.[135] However, in a transmission-mode study published by Waluyo *et al.*, the alkali chlorides and fluorides from Li^+ through Rb^+ exhibited the spectral signatures of disrupted hydrogen bonding – that is, reduced post-edge and enhanced pre-edge intensity, with cations larger than sodium also inducing a small red shift.[69] With the exception of Rb^+, the observed spectral changes are more pronounced with each larger cation. As with the preceding study of anions, the cause of this discrepancy is currently unclear.

Utilizing the same methodology as that which found a red shift for NaCl, Cappa *et al.* found a substantially smaller and opposite spectral change for solutions of HCl than those of NaCl.[136] This has been attributed to competing effects; that is, while chloride is implicated as a "structure breaker" in aqueous solution, the hydronium ion acts as a "structure maker," with the combination resulting in a solution NEXAFS spectrum similar to that of neat water. Chen *et al.* have studied the NEXAFS spectra of aqueous HCl and NaOH and suggest that hydronium structures water within the first solvation shell, but hydroxide induces longer-range ordering.[137] Some multivalent cations may also be implicated as structure makers as a result of apparent offsetting spectral effects in the spectra measured for their halide salts.[133,138] Spectral effects of multivalent cations also appear to be ion-specific and may result from a combination of structural impact on the water hydrogen bonding network and electronic coupling between the ions and near-neighbor solvent molecules. The question of whether ions substantially impact the hydrogen bond network of water outside the first solvation shell remains open.

V. XAS of Short-Chain Alcohols

While studies of water and aqueous solutions have clearly dominated the field of XAS of liquids since its introduction, short-chain alcohols have also been the subject of an increasing number of experiments in recent years. The first and most-common non-aqueous liquid to be studied by XAS has been methanol. As it contains only one O-H bond, methanol can only donate one hydrogen bond per molecule and therefore has an average of ~2 H-bonded nearest-neighbors.[139] Consequently, the local liquid structure comprises primarily rings and chains, and methanol exhibits lower density than water at room temperature despite a shorter O-O separation. Wilson *et al.* first reported the TEY EXAFS spectrum of methanol above the oxygen K-edge in a liquid microjet in 2002,[93] determining an average nearest-neighbor O-O distance of 2.75 Å, slightly shorter than the O-O hydrogen bond pair length of bulk water and in good agreement with existing neutron and X-ray diffraction measurements.[140] Subsequently, the liquid methanol NEXAFS spectrum has been measured on both the oxygen and carbon k-edges.[141–145] The carbon K-edge spectrum of liquid methanol measured by Cappa *et al.* is only moderately distinguishable from that of the vapor and thus provides little opportunity for extraction of meaningful information on the liquid structure,[142] consistent with the vapor-phase finding that carbon K-edge spectrum of CH_3 is largely insensitive to the chemical environment.[146] The carbon K-edge spectrum of Nagasaka *et al.* does exhibit some broadening and enhanced post-edge intensity.[144] In contrast, Figure 16 illustrates that the oxygen K-edge spectrum exhibits a similar behavior to that observed upon condensation of water: a blue shift, reduction in $4a_1$ peak

intensity, and broadening of the higher-energy spectral features.[141–145] Indeed, the liquid methanol spectrum closely resembles that of liquid water, with reduced pre-edge intensity and a more extended but less distinct post-edge feature (see comparison of methanol and water spectra in Figure 17). Computational analysis of this spectrum indicates that the spectral signature is consistent with a 2-dimensional structure of rings and chains with few dangling hydrogen bonds; however, the calculated spectral signatures of rings vs. chains may be too similar to differentiate their relative populations from the NEXAFS spectrum.[142,143] Moreover, while longer-chain and branched alcohols of up to 4 carbons exhibit small but distinct spectral differences on the oxygen K-edge, the spectral signature of hydrogen bonding and calculated hydrogen bonding structure are similar for all such species.[143]

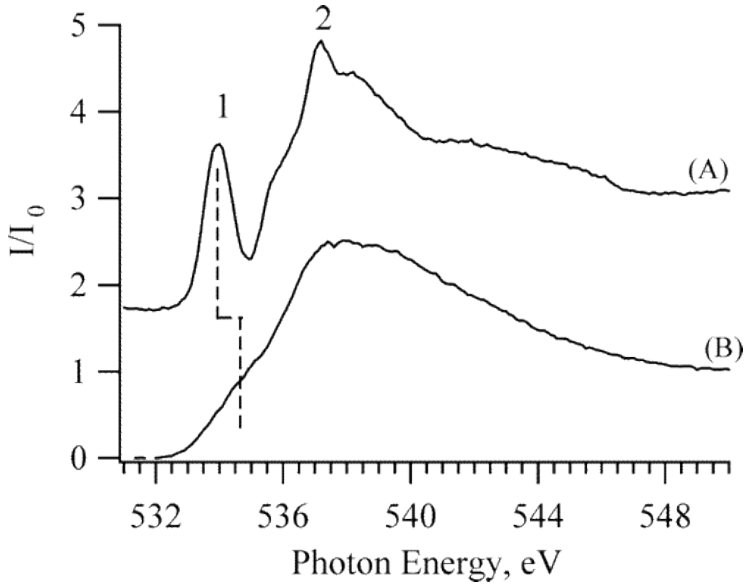

Figure 16: Comparison of the oxygen K-edge NEXAFS spectra of methanol in the vapor phase (A) and liquid phase (B). Liquid spectra were collected via TEY of a liquid methanol microjet; the vapor spectrum was collected using the same experimental apparatus by translating the jet several cm from the X-ray beamline, allowing only the evaporated gas to interact with the X-rays. Reproduced from K. R. Wilson *et al.*, "X-Ray Absorption Spectroscopy of Liquid Methanol Microjets: Bulk Electronic Structure and Hydrogen Bonding Network." *J. Phys. Chem. B* **2005**, *109* (20), 10194–10203.

While the various spectra measured for liquid methanol are all generally in good agreement, one small but potentially meaningful difference again occurs between the spectra collected from liquid microjets[145] and those collected in flow cells.[141,144] As illustrated in Figure 16, when compared directly with a water spectrum collected under the same conditions, the liquid microjet experiment produces a methanol spectrum for which the pre-edge is at slightly lower energy than that of water. In flow cell experiments, the pre-edge of methanol is at the same or slightly higher energy. As is the case for similar anomalies discussed above in the spectra of salt solutions, the origin of this discrepancy is not clear.

Mixtures of water and methanol are of interest due to their unusual thermodynamic properties. It has long been known that these mixtures exhibit a negative excess entropy of mixing; that is, mixtures are more ordered than would be suggested by an ideal/random

mixing.[147] Possible explanations for and previous studies of this phenomenon are discussed in Refs. 144 and 145 and references therein. The sensitivity of NEXAFS spectra to local hydrogen bonding structure makes the technique an ideal tool to investigate the local structure in H_2O:MeOH mixtures. Guo *et al.* interrogated several water:methanol mixtures on the oxygen K-edge utilizing a photon-in, photon-out (TFY) flow cell.[141] Their experimental spectra exhibit a new feature 3 eV below the pre-edge for liquid mixtures. Analysis of the observed spectra in light of both calculations and complimentary X-ray emission experiments attributes the observed negative excess enthalpy of mixing to two factors: 1) incomplete mixing and micro-immiscibility and 2) conversion of methanol chains into more organized ring structures containing one or more water molecules. Later studies of the oxygen K-edge of water:methanol mixtures by Nagasaka *et al.* and Lam *et al.*, displayed in Figure 17, observed no new low-energy feature upon solvent mixing.[144,145] Instead, the pre-edge regions of solution spectra appear as linear combinations of the water and methanol spectra. Nagasaka *et al.* find a linear relationship between the relative concentrations of the components and the intensities of their respective spectral components. Lam *et al.*, however, observed a faster-than-linear decrease in the spectral intensity of the methanol pre-edge upon addition of water and therefore have attributed the negative excess entropy of mixing to a reduction in the number of broken hydrogen bonds around the methanol molecules in water:methanol mixtures relative to the neat liquid.

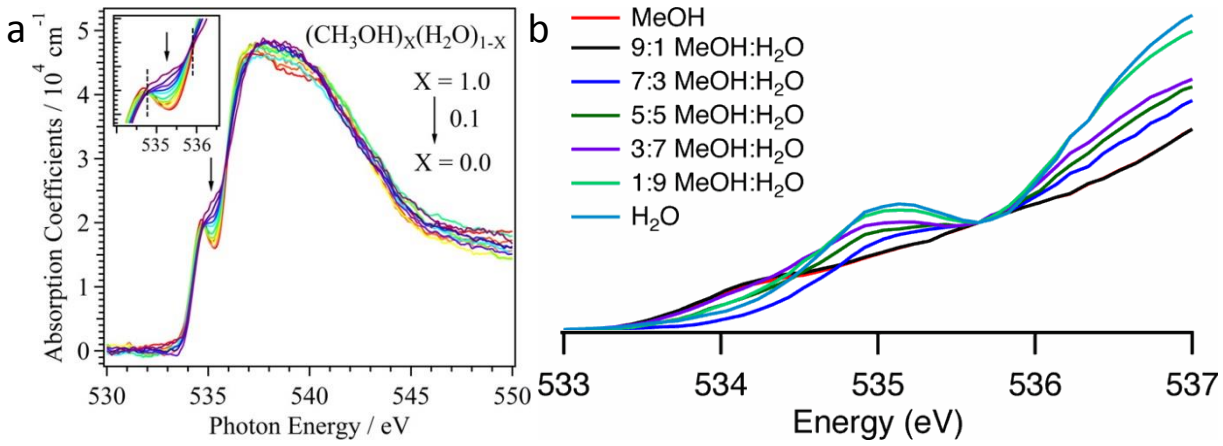

Figure 17: Oxygen K-edge NEXAFS spectra of water:methanol mixtures. a) Transmission-mode flow-cell spectra of Nagasaka *et al.*; the pure water spectrum is in red and the the pure methanol spectrum in violet. The pre-edge becomes increasingly pronounced as the fraction of water increases and shifts to lower energy. Reproduced from M. Nagasaka *et al.*, "Local Structures of Methanol-Water Binary Solutions Studied by Soft X-Ray Absorption Spectroscopy." *J. Phys. Chem. B* **2014**, *118* (16), 4388–4396. b) Liquid jet TEY spectra of Lam *et al.* around the pre-edge spectral region. In these data the pre-edge also becomes more prominent as the fraction of water increases but it is observed to shift to higher energy. Reproduced from R. K. Lam *et al.*, "Communication: Hydrogen Bonding Interactions in Water-Alcohol Mixtures from X-Ray Absorption Spectroscopy." *J. Chem. Phys.* **2016**, *144* (19), 191103.

VI. XAS of Solutes as a Probe of Solution Structure

a. Probing Solute-Solute Interactions

The vast majority of chemical reactions are carried out in solution, wherein details of the interactions of solutes with solvent molecules and one another are critical for controlling their rates and products. Consequently, a clear picture of the chemical environments of molecules in solution is critical to a proper understanding of these reactions. XAS has proven to be a powerful probe of the solvation environment of appropriately chosen solutes. It should be noted that it is not always an effective tool for all solutes, however. For example, DFT calculations on a variety of molecular configurations indicate that the boron K-edge spectra of aqueous boric acid, borate, and polyborate, while clearly distinct from one another, are largely insensitive to the formation of contact pairs with sodium ions.[148] Similarly, the calculated nitrogen K-edge spectra of the aqueous sodium salts of nitrate and nitrite are insensitive to both ion pairing and hydration number and geometry.[149] Computational results with respect to ion pairing in these cases are supported by experimental data indicating no spectral changes as a function of salt concentration. Conversely, concentration-dependent investigation of the sodium K-edge in aqueous NaCl reveals a distinct spectral signature of ionic association.[96,150] Computational spectroscopy further reveals that the observed spectral changes are associated with the formation of solvent-separated (alternatively "solvent-shared") ion pairs rather than contact ion pairs.[150] Moreover, the spectral shape can be assigned to sodium ions solvated by either 6 waters or 5 waters and one chloride, providing a qualitative understanding of the overall solvation environment. Addition of hydroxide to solutions containing Na^+ results in the formation of ion clusters, with each OH^- interacting with 2.4±0.6 Na^+ ions as either contact or solvent-separated ion pairs.[151]

It should be noted that NEXAFS spectral analyses are often not so quantitative. For example, observe the concentration-dependent spectra of aqueous $NiCl_2$ on the nickel L_3-edge presented in Figure 18.[152] The peaks labeled P_1 and P_2 correspond to transitions into the triplet and singlet final states, respectively. It is clear that at elevated salt concentration excitations into the singlet state become increasingly favorable. An additional feature above P_2 is predicted for Ni^{2+} ions in contact ion pairs and is visible in the spectrum of solid $NiCl_2$. As there is at most a slight indication of the appearance of this peak in the 1.5M solution spectrum, it appears that, as with NaCl, any ion pairing occurs via solvent-sharing and not direct ion-ion interaction. Calculations indicate that enhancement of the singlet excitation can occur upon reweighting of the transition dipole matrix elements induced by breaking of the dipole equivalence of the symmetry axes. However, no quantitative picture of the solvation sphere corresponding to such a shift in the matrix elements can be deduced, merely the existence of a change resulting from asymmetry generated by formation of solvent-separated ion pairs.

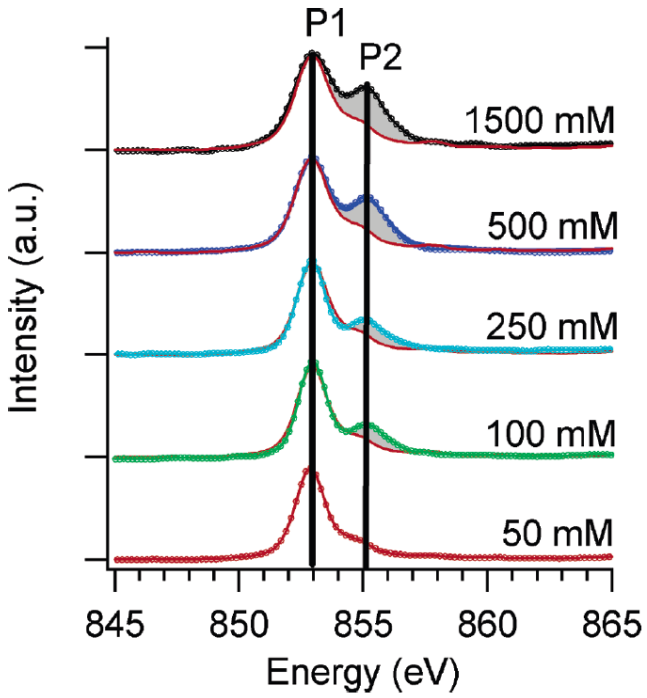

Figure 18: Nickel L_3-edge TFY NEXAFS spectrum, collected in a flow cell, of several concentrations of aqueous $NiCl_2$. The solid red lines indicate the projected 50 mM spectrum corrected for saturation effects at higher concentrations. Thus, the area on each spectrum shaded in grey is the concentration-dependent spectral enhancement at that concentration. Reproduced from E. F. Aziz *et al*., "Direct Contact versus Solvent-Shared Ion Pairs in NiCl2 Electrolytes Monitored by Multiplet Effects at Ni(II) L Edge X-Ray Absorption." *J. Phys. Chem. B* **2007**, *111* (17), 4440–4445.

In addition to concentration-dependent pairing effects, ion-specific pairing effects have been observed for carbonyl species.[135,153] On the carbon K-edge, blue shifts in the NEXAFS spectral features corresponding to the $C_{1s}\rightarrow\pi^*_{C=O}$ transitions of acetate and formate correspond to stronger cation interactions with the carbonyl oxygen.[153] Using this formalism, it is established that Li^+ associates more strongly with the carbonyl than does Na^+, which in turn associates more strongly than does K^+, consistent with the respective ionic sizes and charge densities of these species. Moreover, the magnitude of the observed shift between the sodium and potassium acetate spectral features is similar to the difference in interaction energies previously reported for these species.[154] On the oxygen K-edge, enhanced interaction strength with the counterion manifests as an enhancement of the spectral feature corresponding to the $O_{1s}\rightarrow\pi^*_{C=O}$ transition in solutions of acetate, formate, and glycine.[135] Donation of electron density from the π^* orbital to the cation results in an increased unoccupied density of states in the final state, resulting in the stronger spectral signature for this transition shown in Figure 19. Interestingly, by this measure the interaction strength of the carbonyl with lithium is found to be weaker than that with sodium.

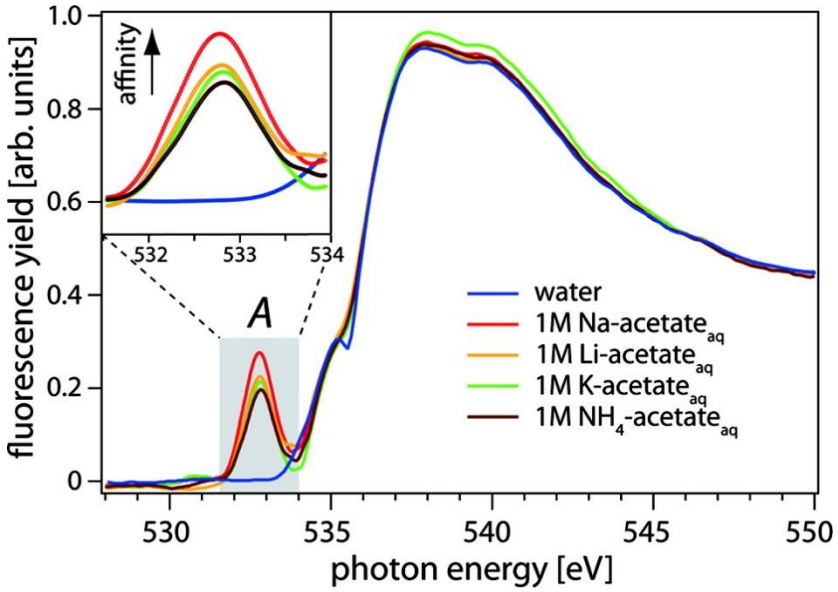

Figure 19: TFY oxygen K-edge NEXAFS spectra of several salts of acetate compared to that of neat water. Reproduced from E. F. Aziz *et al*., "Cation-Specific Interactions with Carboxylate in Amino Acid and Acetate Aqueous Solutions: X-Ray Absorption and Ab Initio Calculations." *J. Phys. Chem. B* **2008**, *112* (40), 12567–12570.

NEXAFS spectroscopy is also a valuable tool for the study of solute aggregation. In addition to the water clusters in organic solvents discussed earlier in this review, solutions of acetic acid provide an interesting example, as the gas-phase oxygen K-edge NEXAFS spectra of monomeric and small-cluster acetic acid are well known[155] and provide a reference for spectral behavior upon clustering. Figure 20 exhibits these reference spectra along with the spectra of several concentrations of acetic acid dissolved in hexane and acetonitrile.[156] It is clear that both cluster formation and dissolution in these organic solvents results in a systematic narrowing of the gap between the π* feature at ~532 eV, corresponding to the transition originating from the carbonyl oxygen 1s, and the π* feature at ~535 eV, corresponding to the transition originating from the hydroxyl oxygen 1s. These effects can be attributed to the formation of strong hydrogen bonds at both oxygens. Donation of hydrogen bonds by the hydroxyl oxygen and acceptance of hydrogen bonds by the carbonyl oxygen make the oxygens increasingly indistinguishable as the hydrogen bonds grow stronger/shorter, causing the peak positions to move nearer to one another. Based on the experimental spectra, it is clear that acetic acid in hexane solution forms dimers or larger clusters at all experimental concentrations. In acetonitrile this phenomenon is enhanced with concentration, indicating a cooperative enhancement of hydrogen bonding interactions as a function of acetic acid concentration. Whereas acetonitrile acts as a hydrogen-bond acceptor in MD simulations of this system, hexane cannot act as a hydrogen-bond donor or acceptor. Thus, interaction of acetic acid molecules with one another must cause the observed shifts. A slightly more pronounced shift has also been observed in glacial acetic acid.[157] Perhaps a more unusual example of aggregation of like-type solutes is the π-stacking cation-cation pair formation observed by Shih *et al.* in aqueous solutions of guanidinium chloride.[158] Observed spectral changes in nitrogen K-edge NEXAFS spectrum at concentrations above 1M can only be reproduced in the theory by formation of like-charge ion pairs. In this case the π-stacking energy is sufficient to overcome the electrostatic repulsion under concentrated conditions.

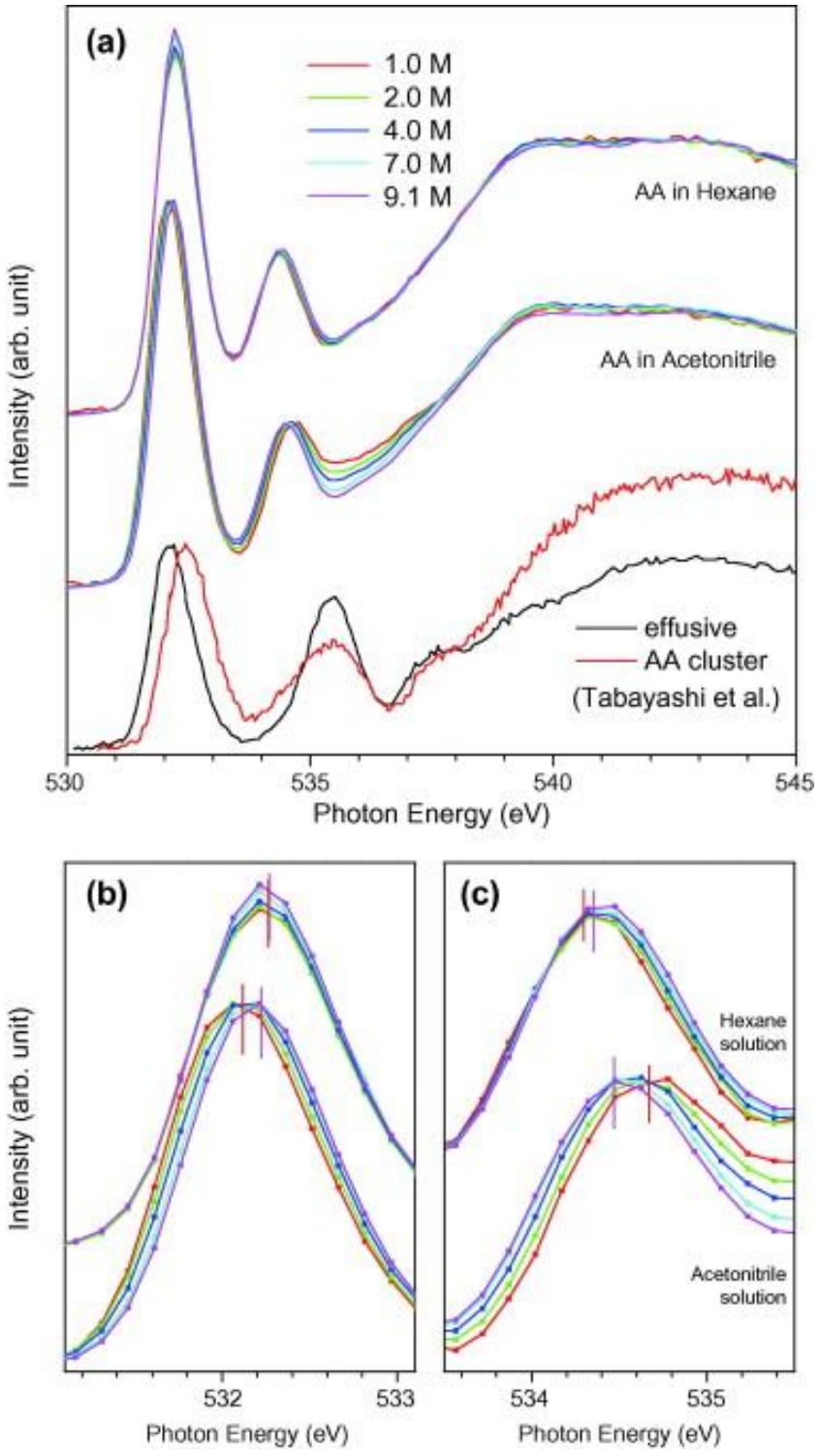

Figure 20: Oxygen K-edge TFY NEXAFS spectra of acetic acid solutions in hexane and acetonitrile. Vapor-phase spectra of monomeric and clustered acetic acid are provided for reference. The two sharp π* features are shown in greater detail in (b) and (c). Reproduced from Y. Horikawa *et al*., "Spectral Fingerprint in X-Ray Absorption for Hydrogen-Bonded Dimer Formation of Acetic Acids in Solution." *Chem. Phys. Lett.* **2012**, *522*, 33–37.

b. Probing Solute-Solvent Interactions

As described in the previous section, the solvation environment of Na^+ in aqueous solution comprises 6 components (6 waters or 5 waters and one counterion).[150] The solvation environment of Na^+ in ethanol has been determined to have the same composition.[96] More recently, the solvation of sodium halides has been studied in water, methanol, ethanol, propanol, and mixtures thereof.[159] The dipole interaction strength of the alcohol solvents was found to decrease with increasing chain length. However, Figure 21 illustrates that the sodium K-edge NEXAFS spectrum of Na^+ in a mixture of water and methanol contains similar contributions from the pure water and pure methanol solution spectra, while water:ethanol and methanol:ethanol mixtures favor water and methanol over ethanol at approximately 2:1. However, in spite of the apparently similar interactions of sodium ions with water and methanol, water is found to have a particularly stabilizing effect on the solvation shell. Stopping the liquid flow within the experimental cell and exposing the alcohol solutions to soft X-rays over time results in the formation of I_3^- as a result of radiative sample damage. Triiodide binds tightly with the Na^+ ion in alcohol solution, which causes a substantial change in the observed spectrum in alcohol solutions (Figure 21d). However, in water and water-alcohol mixed solvents no spectral changes are observed with irradiation time, which has been attributed to a stabilization of the solvation shell by water which prevents triiodide from forming contact ion pairs.

The solvation of Fe^{2+} and Fe^{3+} have also been investigated in water and short-chain alcohol solvents.[96,160] The charge states of iron differ meaningfully in their spectral fine structure on the iron L_2 and L_3 edges. The corresponding solvation structures in alcohols have been determined from ligand multiplet electronic structure calculations to be octahedral for Fe^{3+} and primarily tetragonal for Fe^{2+}.[160] In addition, the spectral differences between the oxidation states have been utilized by Nagasaka *et al.* to demonstrate the capabilities of their electrochemical flow cell.[105–107] The authors have utilized cell potentials to reversibly cycle between Fe^{2+} and Fe^{3+} in aqueous solutions of iron sulfate without evidence of radiative or electrochemical sample damage. The solvation of Li^+ in solutions of $LiBF_4$ in propylene carbonate has been measured via NEXAFS by Smith *et al.*[161] In this case, a blue shift in the spectral feature in the oxygen K-edge spectrum of propylene carbonate corresponding to the $1s_{carbonyl} \rightarrow \pi^*$ transition occurs when the carbonyl oxygen is in the first solvation shell of a lithium ion. Spectral analysis and electronic structure calculations within the XCH approximation permit the net shift in experimental solution spectra to be interpreted as a proportion of Li^+-binding and non-Li^+-binding solvent molecules and so determine a solvation number.

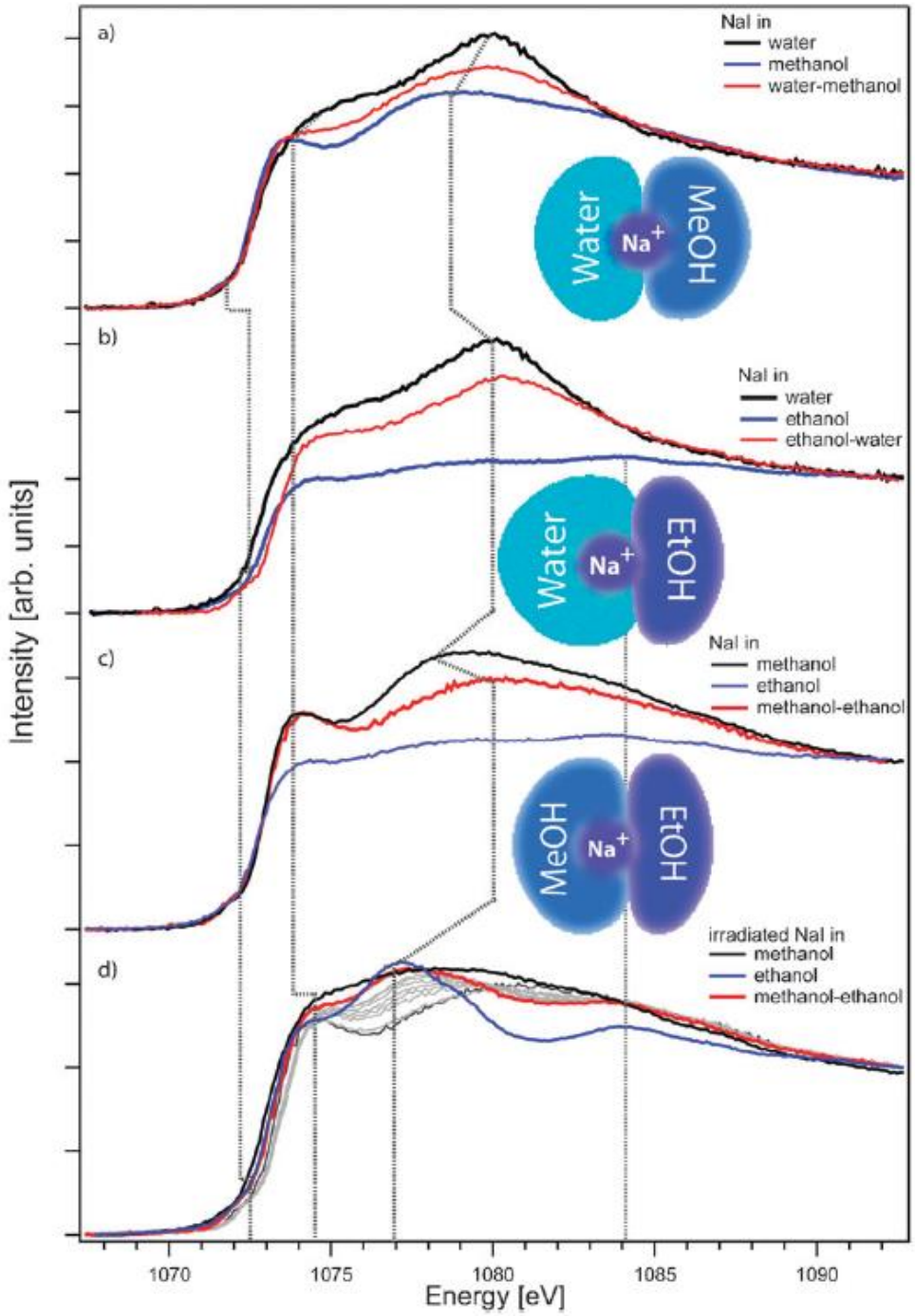

Figure 21: Sodium K-edge TFY NEXAFS spectra of Na^+ in solutions of water, methanol, ethanol, and mixtures thereof collected in a flow cell. Panel (d) exhibits the spectral changes in alcohol solvents observed following extended irradiation under stopped flow conditions. Reproduced from K. M. Lange *et al*., "Shared Solvation of Sodium Ions in Alcohol-Water Solutions Explains the Non-Ideality of Free Energy of Solvation." *Phys. Chem. Chem. Phys.* **2011**, *13* (34), 15423–15427.

We have established the predictive power of XCH calculations for reproducing spectra of the aqueous carbonate system. England *et al.* published the carbon K-edge NEXAFS spectra of aqueous sodium carbonate and bicarbonate and gaseous CO_2 in 2011.[162] Calculated spectra of these species as well as carbonic acid (H_2CO_3) and aqueous CO_2, computed within the XCH approximation, were also published; however, the transient nature of the latter 2 species rendered their experimental detection too difficult in the initial experiment. Lam *et al.* have subsequently developed a fast-flow liquid microjet mixing system utilizing a microfluidic mixing Y-cell to acidify bicarbonate ~5-10 μs before intersecting the solution with the X-ray beamline. Utilizing this apparatus Lam *et al.* have measured the spectra of both aqueous carbonic acid[163] and hydrated CO_2.[164] In particular the NEXAFS spectrum of aqueous CO_2 exhibits not only the characteristic shift in the primary 1s→π* transition observed for all members of the aqueous carbonate system, but also the disappearance of a small vibronic peak that is clearly observed in the spectrum of gaseous CO_2, as shown in Figure 22. It is interesting to note here the significance of this finding relative to the statement made at the beginning of this section of our review: XAS has proven to be a valuable probe of the solvation environment of *appropriately chosen* solutes. The small but distinctive change in the CO_2 carbon K-edge NEXAFS spectrum upon solvation in water – namely, the disappearance of the vibronic peak – occurs in both the experimental and calculated spectrum in spite of very weak hydration energies. MD simulations indicate the existence of only 0.56 hydrogen bonds per solute molecule. This highlights the fact that *appropriately chosen* is not always intrinsically obvious, and in many cases, the suitability of systems for NEXAFS analysis can only be determined empirically.

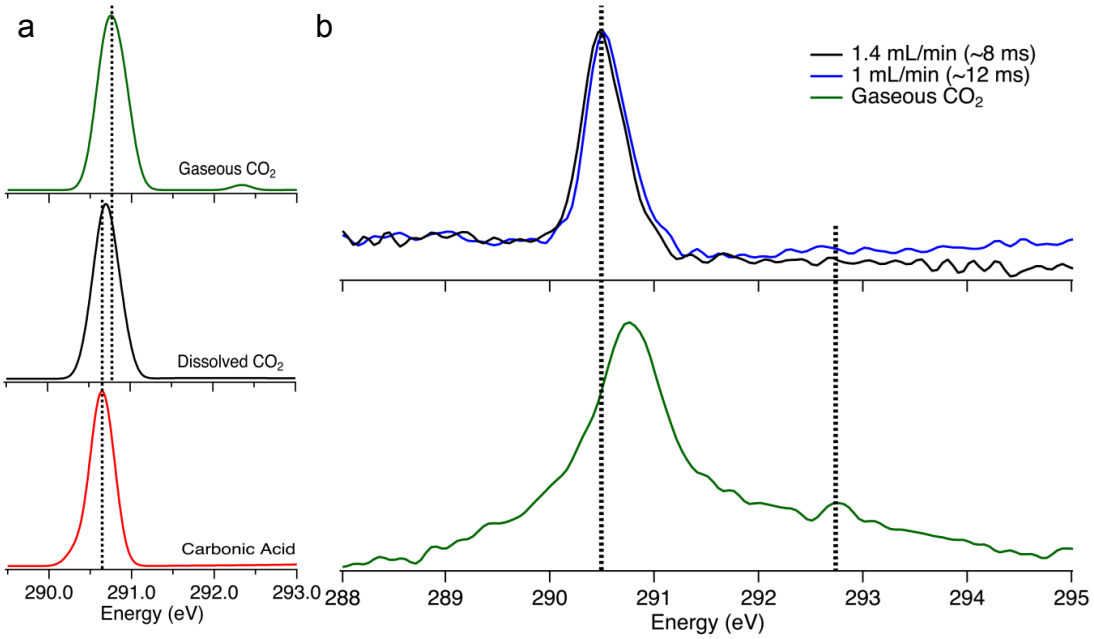

Figure 22: Carbon K-edge NEXAFS spectra of the acidic pH species of the aqueous carbonate system. (a) Calculated spectra of gaseous CO_2, dissolved CO_2, and aqueous carbonic acid. (b) Experimental spectra of 1M HCl and 1M $NaHCO_3$ combined in the fast-flow mixing system with sufficient interaction time to allow H_2CO_3 to decompose into water and CO_2 (top panel) and well before interrogating the system, allowing for CO_2 to leave solution (bottom panel). Reproduced from R. K. Lam *et al.*, "The Hydration Structure of Dissolved Carbon Dioxide from X-Ray Absorption Spectroscopy." *Chem. Phys. Lett.* **2015**, *633*, 214–217.

c. XAS Studies of Solvated Biomolecules

While the suitability of XAS for biomolecules is largely restricted by the size of most such molecules and resulting spectral complexity, some of the most important contributions of the liquid XAS techniques have nevertheless resulted from the study of solvation of biologically relevant molecules, including isolated amino acids,[165–167] polypeptides,[165,168–170] nucleotide bases,[171–173] and adenosine triphosphate (ATP).[174] A great deal of effort has been directed towards the study of the metal centers of metalloproteins, particularly those within porphyrin rings. For example, NEXAFS spectroscopy has been performed on the iron L_2 and L_3 edges – corresponding to transitions from the $2p_{1/2}$ and $2p_{3/2}$ orbitals, respectively - of bovine hemoglobin and hemin in the crystalline and solution phases.[168] The data from these experiments, along with calculated spectra for the solution-phase samples calculated via the ligand multiplet method,[175,176] are exhibited in Figure 23. These data unambiguously demonstrate that while the iron centers in the crystalline forms of these species exist in the low spin state, in the solution phase they are almost exclusively in the high-spin state, as shown by the agreement between experimental spectra and calculated spectra for these spin states. In addition, spectral analysis reveals the extent σ and π donation from the ligands to the iron center and quantifies the total charge transfer between iron and the porphyrin ring. This same technique has more recently been applied to the study of charge transfer between the Fe-porphyrin active region of myoglobin and various transport ligands.[177] The spectra of aqueous myoglobin under ambient conditions in a liquid flow cell exhibited in Figure 24 show a clear reduction in the intensity of the iron L_3-edge upon ligand binding. This reduction is substantially more significant for the more tightly-bound ligands (CO and CN) and has been attributed to charge transfer between the ligands and iron. Additional studies of metal active sites in proteins via X-ray spectroscopies have been previously reviewed by Aziz.[178] In addition, a similar L-edge NEXAFS study has investigated the interaction between Ni^{2+} and nucleotide bases in (Ni)·*M*-DNA, in which the metal ion participates in the base pair bonding interaction.[171]

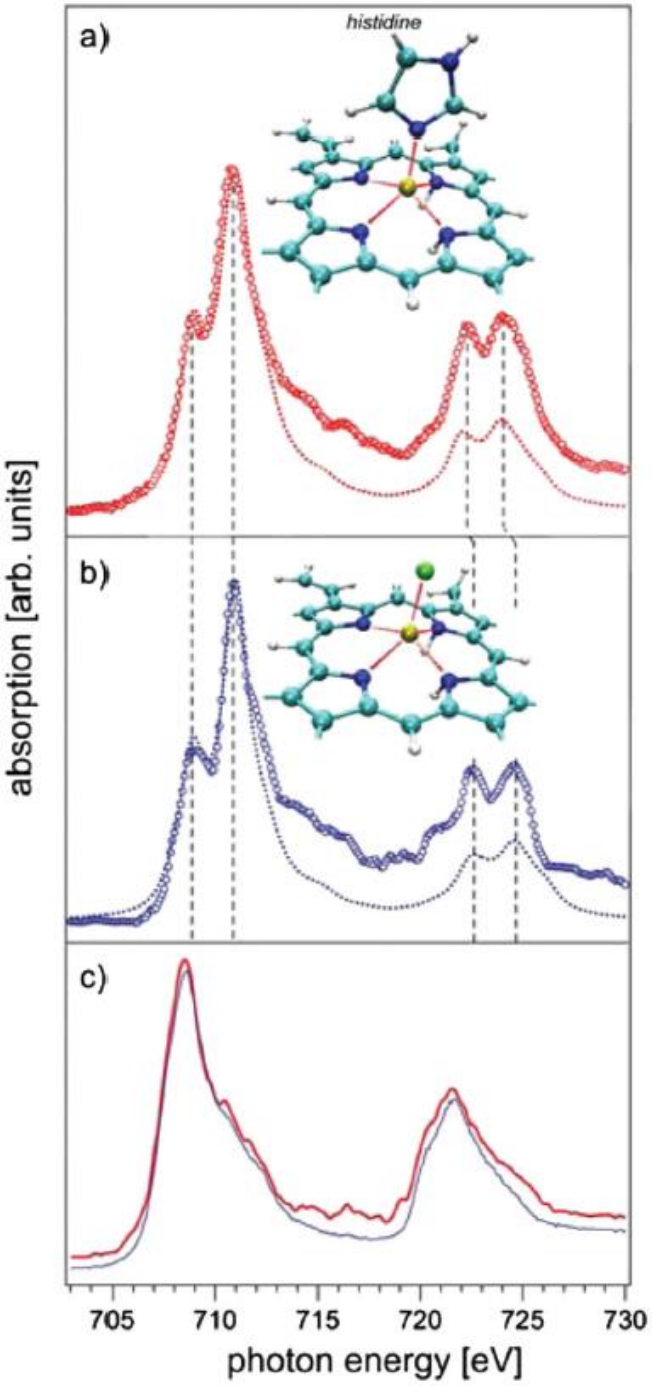

Figure 23: TFY NEXAFS spectra of the Fe L_2 and L_3 edges of (a) 3 mM aqueous solutions of hemoglobin and (b) a 3 mM solution of hemin in ethanol collected in a liquid flow cell, as well as (c) the solid-phase spectra of hemoglobin (red) and hemin (blue). Dotted lines in the solution-phase panels indicate calculated spectra from ligand multiplet calculations. Inset figures show the structures of the iron-porphyrin complexes of hemoglobin and hemin with imidazole and chloride proximal ligands, respectively. Reproduced from E. F. Aziz *et al.*, "Probing the Electronic Structure of the Hemoglobin Active Center in Physiological Solutions." *Phys. Rev. Lett.* **2009**, *102* (6), 68103.

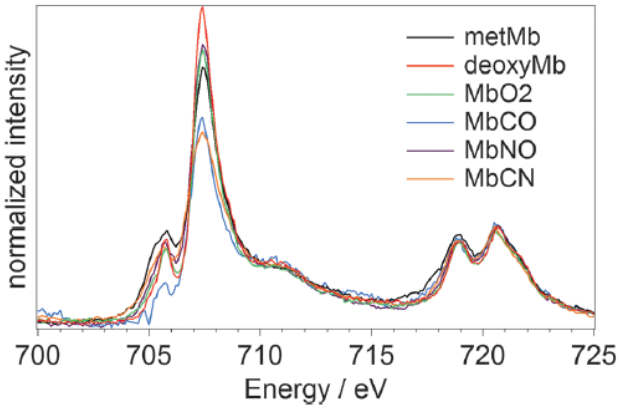

Figure 24: TFY NEXAFS spectra of the Fe L_2 and L_3 edges of myoglobin with various transport ligands. The spectra have been normalized to the intensity of the most intense feature of the L_2 edge centered at ~721 eV. Reduced intensity of the primary feature of the L_3 edge, centered at ~707.5 eV, has been attributed to charge transfer between the ligands and the iron center. Reproduced from K. M. Lange *et al*., "Ligand Discrimination of Myoglobin in Solution: An Iron L-Edge X-Ray Absorption Study of the Active Centre." *Chem. Commun.* **2013**, *49* (39), 4163.

Additional studies of amino acid and protein solvation and structure in solution have been carried out directly on the structural edges of the polypeptide backbone (i.e. C, O, and N K-edges). Such studies are inherently limited to small molecule samples, since large polypeptides contain numerous non-equivalent atoms of these types and thus would have NEXAFS spectra with too much complexity for reasonable interpretation. Schwartz *et al.*, for example, studied the nitrogen K-edge of triglycine in several salt solutions to study specific-ion interactions of the protein backbone with ions across the Hofmeister series.[170] A detailed pH-dependent study of all 3 structural edges of the peptide backbone focused on the isolated glycine amino acid for spectral simplicity.[166] The NEXAFS C, O, and N K-edge spectra of aqueous glycine as a cation, zwitterion, and anion are shown in Figure 25. The oxygen and nitrogen K-edges reveal distinctive spectral changes upon protonation/deprotonation of the target atom, as might be expected. Changes to the carbon K-edge spectrum as a function of pH are subtle. Interestingly, the most obvious change is the red shift in the sharp feature corresponding to the $1s_{C=O} \rightarrow \pi^*$ transition at high pH. The protonation state of the carbonyl oxygen, however, is identical at high and neutral pH. Instead, this shift is thought to arise from a decrease in the electronegativity of nitrogen upon deprotonation resulting in a small rearrangement of the electron localization along the molecular backbone.

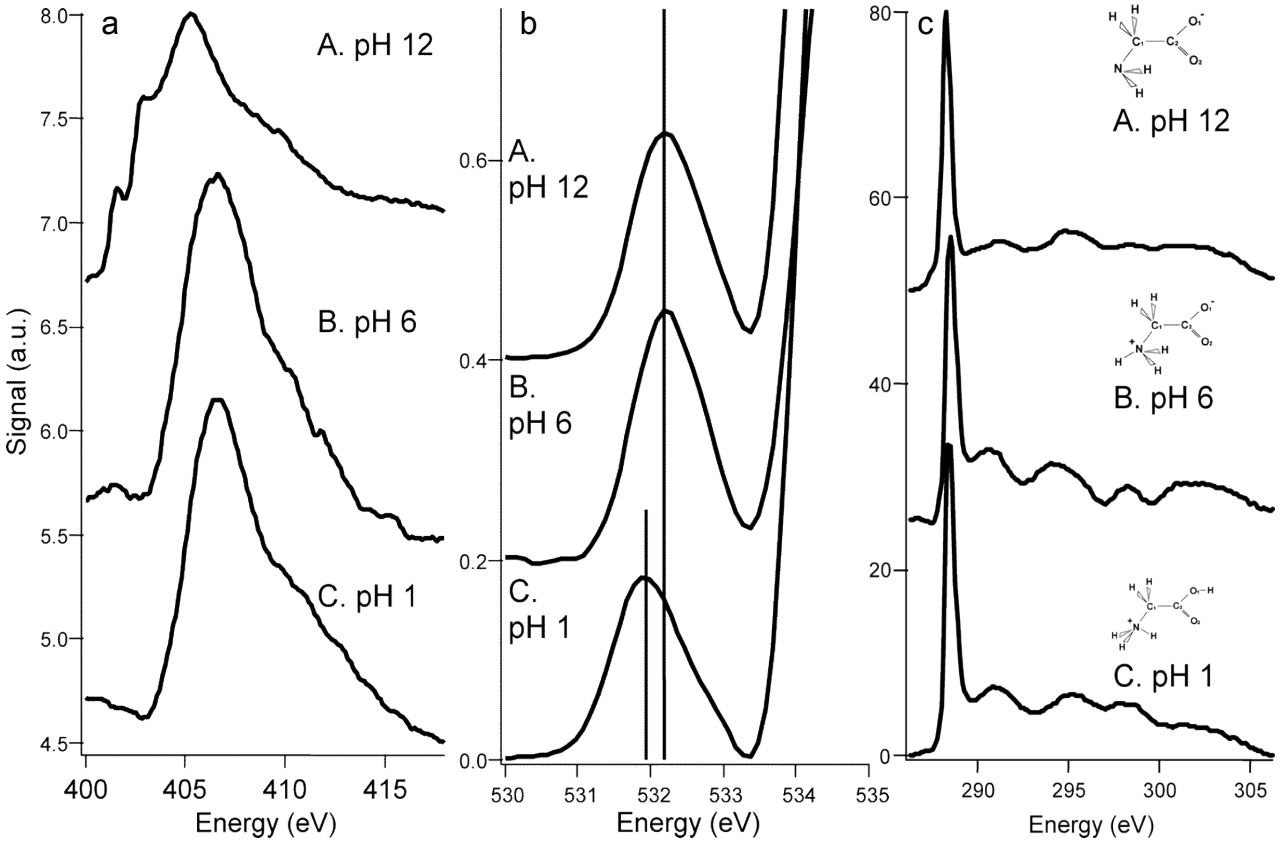

Figure 25: pH dependence of the NEXAFS spectrum of glycine on (a) the nitrogen K-edge, (b) the oxygen K-edge, and (c) the carbon K-edge showing spectra of glycine as an anion (A), zwitterion (B), and cation (C). Spectral changes upon deprotonation of the amino group and protonation of the carboxyl group are clearly visible in the high and low pH spectra, respectively. Reproduced from B. M. Messer *et al.*, "pH Dependence of the Electronic Structure of Glycine." *J. Phys. Chem. B* **2005**, *109* (11), 5375–5382.

VII. Concluding Remarks

Since the introduction of liquid microjet technology into XAS in 2001, X-ray absorption spectroscopy has evolved into a general and powerful tool for the study of the structures and dynamics of liquids and solutions. NEXAFS and EXAFS techniques, coupled with electronic structure calculations, have now been utilized to characterize the local environments of many species in the liquid phase. The atom-specific nature of this spectroscopy allows for the chemical environments of specific atoms in fairly complex molecules to be investigated, providing a probe of solute-solute, solute-solvent, and solvent-solvent interactions. This review has provided an overview of current capabilities of XAS for the study of liquids, and highlighted some salient results obtained from these experiments. We have also revealed a trend of subtle but unmistakable discrepancies between spectra of liquid systems measured in liquid microjets and flow cells, particularly with regards to changes to the water oxygen K-edge NEXAFS spectrum upon addition of solutes. The origin of this discrepancy has not yet been examined.

VIII. References

(1) Stumm von Bordwehr, R. A History of X-Ray Absorption Fine Structure. *Ann. Phys. (Paris).* **1989**, *14* (4), 377–465.

(2) Stern, E. A. Musings about the Development of XAFS. *J. Synchrotron Radiat.* **2001**, *8* (2), 49–54.

(3) Wilson, K. R.; Rude, B. S.; Catalane, T.; Schaller, R. D.; Tobin, J. G.; Co, D. T.; Saykally, R. J. X-Ray Spectroscopy of Liquid Water Microjets. *J. Phys. Chem. B* **2001**, *105* (17), 3346–3349.

(4) Lange, K. M.; Aziz, E. F. Electronic Structure of Ions and Molecules in Solution: A View from Modern Soft X-Ray Spectroscopies. *Chem. Soc. Rev.* **2013**, *42* (16), 6840–6859.

(5) Nilsson, A.; Nordlund, D.; Waluyo, I.; Huang, N.; Ogasawara, H.; Kaya, S.; Bergmann, U.; Näslund, L.-Å.; Öström, H.; Wernet, P.; *et al.* X-Ray Absorption Spectroscopy and X-Ray Raman Scattering of Water and Ice; an Experimental View. *J. Electron Spectros. Relat. Phenomena* **2010**, *177* (2–3), 99–129.

(6) Nilsson, A.; Pettersson, L. G. M. Perspective on the Structure of Liquid Water. *Chem. Phys.* **2011**, *389* (1–3), 1–34.

(7) Fransson, T.; Harada, Y.; Kosugi, N.; Besley, N. A.; Winter, B.; Rehr, J. J.; Pettersson, L. G. M.; Nilsson, A. X-Ray and Electron Spectroscopy of Water. *Chem. Rev.* **2016**, acs.chemrev.5b00672.

(8) Hubbell, J. H.; Gimm, H. A.; Øverbø, I. Pair, Triplet, and Total Atomic Cross Sections (and Mass Attenuation Coefficients) for 1 MeV-100 GeV Photons in Elements Z=1 to 100. *J. Phys. Chem. Ref. Data* **1980**, *9* (4), 1023.

(9) Stöhr, J. *NEXAFS Spectroscopy*; Springer Series in Surface Sciences; Springer Berlin Heidelberg: Berlin, Heidelberg, 1992; Vol. 25.

(10) Fischer, D. .; Döbler, U.; Arvanitis, D.; Wenzel, L.; Baberschke, K.; Stöhr, J. Carbon K-Edge Structure of Chemisorbed Molecules by Means of Fluorescence Detection. *Surf. Sci.* **1986**, *177* (1), 114–120.

(11) Seligson, D.; Pan, L.; King, P.; Pianetta, P. Soft X-Ray Dosimetry and Its Application on the Lithography Beamline at SSRL. *Nucl. Instruments Methods Phys. Res. Sect. A Accel. Spectrometers, Detect. Assoc. Equip.* **1988**, *266* (1–3), 612–618.

(12) Krause, M. O. Atomic Radiative and Radiationless Yields for K and L Shells. *J. Phys. Chem. Ref. Data* **1979**, *8* (2), 307.

(13) de Groot, F. M. F.; Arrio, M. A.; Sainctavit, P.; Cartier, C.; Chen, C. T. Distortions of X-Ray Absorption Spectra Measured with Fluorescence Yield. *Phys. B Condens. Matter* **1995**, *208–209*, 84–86.

(14) de Groot, F. M. F.; Arrio, M. A.; Sainctavit, P.; Cartier, C.; Chen, C. T. Fluorescence Yield Detection: Why It Does Not Measure the X-Ray Absorption Cross Section. *Solid State Commun.* **1994**, *92* (12), 991–995.

(15) Henderson, G. S.; de Groot, F. M. F.; Moulton, B. J. A. X-Ray Absorption Near-Edge Structure (XANES) Spectroscopy. *Rev. Mineral. Geochemistry* **2014**, *78* (1), 75–138.

(16) Achkar, A. J.; Regier, T. Z.; Wadati, H.; Kim, Y.-J.; Zhang, H.; Hawthorn, D. G. Bulk Sensitive X-Ray Absorption Spectroscopy Free of Self-Absorption Effects. *Phys. Rev. B* **2011**, *83* (8), 81106.

(17) Lange, K. M.; Suljoti, E.; Aziz, E. F. Resonant Inelastic X-Ray Scattering as a Probe of Molecular Structure and Electron Dynamics in Solutions. *J. Electron Spectros. Relat. Phenomena* **2013**, *188*, 101–110.

(18) Henke, B. L.; Lee, P.; Tanaka, T. J.; Shimabukuro, R. L.; Fujikawa, B. K. Low-Energy X-Ray Interaction Coefficients: Photoabsorption, Scattering, and Reflection. *At. Data Nucl. Data Tables* **1982**, *27* (1), 1–144.

(19) Bianconi, A. Surface X-Ray Absorption Spectroscopy: Surface EXAFS and Surface XANES. *Appl. Surf. Sci.* **1980**, *6* (3–4), 392–418.

(20) Abbate, M.; Goedkoop, J. B.; de Groot, F. M. F.; Grioni, M.; Fuggle, J. C.; Hofmann, S.; Petersen, H.; Sacchi, M. Probing Depth of Soft X-Ray Absorption Spectroscopy Measured in Total-Electron-Yield Mode. *Surf. Interface Anal.* **1992**, *18* (1), 65–69.

(21) Frazer, B. H.; Gilbert, B.; Sonderegger, B. R.; De Stasio, G. The Probing Depth of Total Electron Yield in the Sub-keV Range: TEY-XAS and X-PEEM. *Surf. Sci.* **2003**, *537* (1–3), 161–167.

(22) Smith, J. D. Response to Comment on "Energetics of Hydrogen Bond Network Rearrangements in Liquid Water." *Science* **2005**, *308* (5723), 793b–793b.

(23) Ogletree, D. F.; Bluhm, H.; Lebedev, G.; Fadley, C. S.; Hussain, Z.; Salmeron, M. A Differentially Pumped Electrostatic Lens System for Photoemission Studies in the Millibar Range. *Rev. Sci. Instrum.* **2002**, *73* (11), 3872.

(24) Bluhm, H.; Ogletree, D. F.; Fadley, C. S.; Hussain, Z.; Salmeron, M. The Premelting of Ice Studied with Photoelectron Spectroscopy. *J. Phys. Condens. Matter* **2002**, *14* (8), L227–L233.

(25) Carlson, T. A. Measurement of the Relative Abundances and Recoil-Energy Spectra of Fragment Ions Produced as the Initial Consequences of X-Ray Interaction with CH_3I, HI, and DI. *J. Chem. Phys.* **1966**, *44* (12), 4510.

(26) Knotek, M. L.; Feibelman, P. J. Ion Desorption by Core-Hole Auger Decay. *Phys. Rev. Lett.* **1978**, *40* (14), 964–967.

(27) Wilson, K. R.; Cavalleri, M.; Rude, B. S.; Schaller, R. D.; Nilsson, A.; Pettersson, L. G. M.; Goldman, N.; Catalano, T.; Bozek, J. D.; Saykally, R. J. Characterization of Hydrogen Bond Acceptor Molecules at the Water Surface Using near-Edge X-Ray Absorption Fine-Structure Spectroscopy and Density Functional Theory. *J. Phys. Condens. Matter* **2002**, *14* (8), L221–L226.

(28) Jaeger, R.; Treichler, R.; Stöhr, J. Evidence for Multi-Electron Excitations in Photon Stimulated Ion Desorption: CO and NO on Ni(100). *Surf. Sci.* **1982**, *117* (1–3), 533–548.

(29) Jaeger, R.; Stöhr, J.; Treichler, R.; Baberschke, K. Photon-Stimulated Desorption due to Multielectron Excitations in Chemisorbed Molecules: CO on Ni(100). *Phys. Rev. Lett.* **1981**, *47* (18), 1300–1304.

(30) Coulman, D.; Puschmann, A.; Höfer, U.; Steinrück, H.-P.; Wurth, W.; Feulner, P.; Menzel, D. Excitation, Deexcitation, and Fragmentation in the Core Region of Condensed and Adsorbed Water. *J. Chem. Phys.* **1990**, *93* (1), 58.

(31) Cappa, C. D.; Smith, J. D.; Wilson, K. R.; Saykally, R. J. Revisiting the Total Ion Yield X-Ray Absorption Spectra of Liquid Water Microjets. *J. Phys. Condens. Matter* **2008**, *20* (20), 205105.

(32) *Unoccupied Electronic States - Fundamentals for XANES, EELS, IPS and BIS*; Fuggel, J. C., Inglesfield, J. E., Eds.; Springer: Berlin, 1991.

(33) Sayers, D. E.; Stern, E. A.; Lytle, F. W. New Technique for Investigating Noncrystalline Structures: Fourier Analysis of the Extended X-Ray—Absorption Fine Structure. *Phys. Rev. Lett.* **1971**, *27* (18), 1204–1207.

(34) Lytle, F. W.; Sayers, D. E.; Stern, E. A. Extended X-Ray-Absorption Fine-Structure Technique. II. Experimental Practice and Selected Results. *Phys. Rev. B* **1975**, *11* (12), 4825–4835.

(35) Stern, E. A.; Sayers, D. E.; Lytle, F. W. Extended X-Ray-Absorption Fine-Structure Technique. III. Determination of Physical Parameters. *Phys. Rev. B* **1975**, *11* (12), 4836–4846.

(36) Rehr, J. J.; Stern, E. A.; Martin, R. L.; Davidson, E. R. Extended X-Ray-Absorption Fine-Structure amplitudes—Wave-Function Relaxation and Chemical Effects. *Phys. Rev. B* **1978**, *17* (2), 560–565.

(37) Rehr, J. J.; Albers, R. C. Theoretical Approaches to X-Ray Absorption Fine Structure. *Rev. Mod. Phys.* **2000**, *72* (3), 621–654.

(38) Lee, P. A.; Citrin, P. H.; Eisenberger, P.; Kincaid, B. M. Extended X-Ray Absorption Fine Structure—its Strengths and Limitations as a Structural Tool. *Rev. Mod. Phys.* **1981**, *53* (4), 769–806.

(39) Ankudinov, A. L.; Ravel, B.; Rehr, J. J.; Conradson, S. D. Real-Space Multiple-Scattering Calculation and Interpretation of X-Ray-Absorption near-Edge Structure. *Phys. Rev. B* **1998**, *58* (12), 7565–7576.

(40) Mizuno, Y.; Ohmura, Y. Theory of X-Ray Raman Scattering. *J. Phys. Soc. Japan* **1967**, *22* (2), 445–449.

(41) Nagasawa, H.; Mourikis, S.; Schülke, W. X-Ray Raman Spectrum of Li, Be and Graphite in a High-Resolution Inelastic Synchrotron X-Ray Scattering Experiment. *J. Phys. Soc. Japan* **1989**, *58* (2), 710–717.

(42) Tohji, K.; Udagawa, Y. Novel Approach for Structure Analysis by X-Ray Raman Scattering. *Phys. Rev. B* **1987**, *36* (17), 9410–9412.

(43) Bowron, D. T.; Krisch, M. H.; Barnes, A. C.; Finney, J. L.; Kaprolat, A.; Lorenzen, M. X-Ray-Raman Scattering from the Oxygen K Edge in Liquid and Solid H_2O. *Phys. Rev. B* **2000**, *62* (14), R9223–R9227.

(44) Krisch, M.; Sette, F. X-ray Raman Scattering from Low-z Materials. *Surf. Rev. Lett.* **2002**, *9* (2), 969–976.

(45) Hitchcock, A. P. Inner Shell Excitation Spectroscopy of Molecules Using Inelastic Electron Scattering. *J. Electron Spectros. Relat. Phenomena* **2000**, *112* (1–3), 9–29.

(46) Wirth, R. Water in Minerals Detectable by Electron Energy-Loss Spectroscopy EELS. *Phys. Chem. Miner.* **1997**, *24* (8), 561–568.

(47) Shih, O.; England, A. H.; Dallinger, G. C.; Smith, J. W.; Duffey, K. C.; Cohen, R. C.; Prendergast, D.; Saykally, R. J. Cation-Cation Contact Pairing in Water: Guanidinium. *J. Chem. Phys.* **2013**, *139* (3), 35104.

(48) Hohenberg, P.; Kohn, W. Inhomogeneous Electron Gas. *Phys. Rev.* **1964**, *136* (3B), B864–B871.

(49) Kohn, W.; Sham, L. J. Self-Consistent Equations Including Exchange and Correlation Effects. *Phys. Rev.* **1965**, *140* (4A), A1133–A1138.

(50) Jahn, S.; Kowalski, P. M. Theoretical Approaches to Structure and Spectroscopy of Earth Materials. *Rev. Mineral. Geochemistry* **2014**, *78* (1), 691–743.

(51) Hetényi, B.; De Angelis, F.; Giannozzi, P.; Car, R. Calculation of near-Edge X-Ray-Absorption Fine Structure at Finite Temperatures: Spectral Signatures of Hydrogen Bond Breaking in Liquid Water. *J. Chem. Phys.* **2004**, *120* (18), 8632–8637.

(52) Chen, W.; Wu, X.; Car, R. X-Ray Absorption Signatures of the Molecular Environment in Water and Ice. *Phys. Rev. Lett.* **2010**, *105* (1), 17802.

(53) Iannuzzi, M. X-Ray Absorption Spectra of Hexagonal Ice and Liquid Water by All-Electron Gaussian and Augmented Plane Wave Calculations. *J. Chem. Phys.* **2008**, *128* (20), 204506.

(54) Sahle, C. J.; Sternemann, C.; Schmidt, C.; Lehtola, S.; Jahn, S.; Simonelli, L.; Huotari, S.; Hakala, M.; Pylkkänen, T.; Nyrow, A.; *et al.* Microscopic Structure of Water at Elevated Pressures and Temperatures. *Proc. Natl. Acad. Sci. U. S. A.* **2013**, *110* (16), 6301–6306.

(55) Wernet, P.; Nordlund, D.; Bergmann, U.; Cavalleri, M.; Odelius, M.; Ogasawara, H.; Näslund, L. A.; Hirsch, T. K.; Ojamäe, L.; Glatzel, P.; *et al.* The Structure of the First Coordination Shell in Liquid Water. *Science* **2004**, *304* (5673), 995–999.

(56) Kong, L.; Wu, X.; Car, R. Roles of Quantum Nuclei and Inhomogeneous Screening in the X-Ray Absorption Spectra of Water and Ice. *Phys. Rev. B* **2012**, *86* (13), 134203.

(57) Wilke, M.; Schmidt, C.; Dubrail, J.; Appel, K.; Borchert, M.; Kvashnina, K.; Manning, C. E. Zircon Solubility and Zirconium Complexation in H_2O+Na_2O+SiO_2±Al_2O_3 Fluids at High Pressure and Temperature. *Earth Planet. Sci. Lett.* **2012**, *349–350*, 15–25.

(58) Tailby, N. D.; Walker, A. M.; Berry, A. J.; Hermann, J.; Evans, K. A.; Mavrogenes, J. A.; O'Neill, H. S. C.; Rodina, I. S.; Soldatov, A. V.; Rubatto, D.; *et al.* Ti Site Occupancy in Zircon. *Geochim. Cosmochim. Acta* **2011**, *75* (3), 905–921.

(59) Rehr, J. J.; Kas, J. J.; Vila, F. D.; Prange, M. P.; Jorissen, K. Parameter-Free Calculations of X-Ray Spectra with FEFF9. *Phys. Chem. Chem. Phys.* **2010**, *12* (21), 5503–5513.

(60) Rehr, J. J.; Kas, J. J.; Prange, M. P.; Sorini, A. P.; Takimoto, Y.; Vila, F. Ab Initio Theory and Calculations of X-Ray Spectra. *Comptes Rendus Phys.* **2009**, *10* (6), 548–559.

(61) Joly, Y. X-Ray Absorption near-Edge Structure Calculations beyond the Muffin-Tin Approximation. *Phys. Rev. B* **2001**, *63* (12), 125120.

(62) Triguero, L.; Pettersson, L. G. M.; Ågren, H. Calculations of near-Edge X-Ray-Absorption Spectra of Gas-Phase and Chemisorbed Molecules by Means of Density-Functional and Transition-Potential Theory. *Phys. Rev. B* **1998**, *58* (12), 8097–8110.

(63) Slater, J. C.; Johnson, K. H. Self-Consistent-Field X α Cluster Method for Polyatomic Molecules and Solids. *Phys. Rev. B* **1972**, *5* (3), 844–853.

(64) Buczko, R.; Duscher, G.; Pennycook, S.; Pantelides, S. Excitonic Effects in Core-Excitation Spectra of Semiconductors. *Phys. Rev. Lett.* **2000**, *85* (10), 2168–2171.

(65) Cavalleri, M.; Odelius, M.; Nordlund, D.; Nilsson, A.; Pettersson, L. G. M. Half or Full Core Hole in Density Functional Theory X-Ray Absorption Spectrum Calculations of Water? *Phys. Chem. Chem. Phys.* **2005**, *7* (15), 2854–2858.

(66) Cappa, C. D.; Smith, J. D.; Wilson, K. R.; Messer, B. M.; Gilles, M. K.; Cohen, R. C.; Saykally, R. J. Effects of Alkali Metal Halide Salts on the Hydrogen Bond Network of Liquid Water. *J. Phys. Chem. B* **2005**, *109* (15), 7046–7052.

(67) Smith, J. D.; Cappa, C. D.; Messer, B. M.; Drisdell, W. S.; Cohen, R. C.; Saykally, R. J. Probing the Local Structure of Liquid Water by X-Ray Absorption Spectroscopy. *J. Phys. Chem. B* **2006**, *110* (40), 20038–20045.

(68) Leetmaa, M.; Ljungberg, M. P.; Lyubartsev, A.; Nilsson, A.; Pettersson, L. G. M. Theoretical Approximations to X-Ray Absorption Spectroscopy of Liquid Water and Ice. *J. Electron Spectros. Relat. Phenomena* **2010**, *177* (2–3), 135–157.

(69) Waluyo, I.; Nordlund, D.; Bergmann, U.; Schlesinger, D.; Pettersson, L. G. M.; Nilsson, A. A Different View of Structure-Making and Structure-Breaking in Alkali Halide Aqueous Solutions through X-Ray Absorption Spectroscopy. *J. Chem. Phys.* **2014**, *140* (24), 244506.

(70) Prendergast, D.; Galli, G. X-Ray Absorption Spectra of Water from First Principles Calculations. *Phys. Rev. Lett.* **2006**, *96* (21), 215502.

(71) Besley, N. A.; Asmuruf, F. A. Time-Dependent Density Functional Theory Calculations of the Spectroscopy of Core Electrons. *Phys. Chem. Chem. Phys.* **2010**, *12* (38), 12024–12039.

(72) DeBeer George, S.; Petrenko, T.; Neese, F. Prediction of Iron K-Edge Absorption Spectra Using Time-Dependent Density Functional Theory. *J. Phys. Chem. A* **2008**, *112* (50), 12936–12943.

(73) Brancato, G.; Rega, N.; Barone, V. Accurate Density Functional Calculations of near-Edge X-Ray and Optical Absorption Spectra of Liquid Water Using Nonperiodic Boundary Conditions: The Role of Self-Interaction and Long-Range Effects. *Phys. Rev. Lett.* **2008**, *100* (10), 107401.

(74) Fransson, T.; Zhovtobriukh, I.; Coriani, S.; Wikfeldt, K. T.; Norman, P.; Pettersson, L. G. M. Requirements of First-Principles Calculations of X-Ray Absorption Spectra of Liquid Water. *Phys. Chem. Chem. Phys.* **2016**, *18* (1), 566–583.

(75) Shirley, E. L.; Soininen, J. A.; Rehr, J. J. Modeling Core-Hole Screening in Core-Excitation Spectroscopies. *Phys. Scr.* **2005**, *2005* (T115), 31.

(76) Rehr, J. J.; Soininen, J. A.; Shirley, E. L. Final-State Rule vs the Bethe-Salpeter Equation for Deep-Core X-ray Absorption Spectra. *Phys. Scr.* **2005**, *2005* (T115), 207.

(77) Vinson, J.; Rehr, J. J.; Kas, J. J.; Shirley, E. L. Bethe-Salpeter Equation Calculations of Core Excitation Spectra. *Phys. Rev. B* **2011**, *83* (11), 115106.

(78) Vinson, J.; Kas, J. J.; Vila, F. D.; Rehr, J. J.; Shirley, E. L. Theoretical Optical and X-Ray Spectra of Liquid and Solid H_2O. *Phys. Rev. B* **2012**, *85* (4), 45101.

(79) Gilmore, K.; Vinson, J.; Shirley, E. L.; Prendergast, D.; Pemmaraju, C. D.; Kas, J. J.; Vila, F. D.; Rehr, J. J. Efficient Implementation of Core-Excitation Bethe–Salpeter Equation Calculations. *Comput. Phys. Commun.* **2015**, *197*, 109–117.

(80) Ball, P. Water as an Active Constituent in Cell Biology. *Chem. Rev.* **2008**, *108* (1), 74–108.

(81) Bernal, J. D.; Fowler, R. H. A Theory of Water and Ionic Solution, with Particular Reference to Hydrogen and Hydroxyl Ions. *J. Chem. Phys.* **1933**, *1* (8), 515.

(82) Rehner, J. The Structure of Water and Ionic Solutions. *Rev. Sci. Instrum.* **1934**, *5* (1), 2.

(83) Maréchal, Y. The Molecular Structure of Liquid Water Delivered by Absorption Spectroscopy in the Whole IR Region Completed with Thermodynamics Data. *J. Mol. Struct.* **2011**, *1004* (1), 146–155.

(84) Larouche, P.; Max, J.-J.; Chapados, C. Isotope Effects in Liquid Water by Infrared Spectroscopy. II. Factor Analysis of the Temperature Effect on H[sub 2]O and D[sub 2]O. *J. Chem. Phys.* **2008**, *129* (6), 64503.

(85) Soper, A. K. The Radial Distribution Functions of Water and Ice from 220 to 673 K and at Pressures up to 400 MPa. *Chem. Phys.* **2000**, *258* (2), 121–137.

(86) Sorenson, J. M.; Hura, G.; Glaeser, R. M.; Head-Gordon, T. What Can X-Ray Scattering Tell Us about the Radial Distribution Functions of Water? *J. Chem. Phys.* **2000**, *113* (20), 9149.

(87) Hura, G.; Russo, D.; Glaeser, R. M.; Head-Gordon, T.; Krack, M.; Parrinello, M.; Hura, G.; Sorenson, J. M.; Glaeser, R. M.; Head-Gordon, T.; *et al.* Water Structure as a Function of Temperature from X-Ray Scattering Experiments and Ab Initio Molecular Dynamics. *Phys. Chem. Chem. Phys.* **2003**, *5* (10), 1981.

(88) Szalewicz, K.; Leforestier, C.; van der Avoird, A. Towards the Complete Understanding of Water by a First-Principles Computational Approach. *Chem. Phys. Lett.* **2009**, *482* (1–3), 1–14.

(89) Yang, B. X.; Kirz, J. Extended X-Ray-Absorption Fine Structure of Liquid Water. *Phys. Rev. B* **1987**, *36* (2), 1361–1364.

(90) Faubel, M.; Schlemmer, S.; Toennies, J. P. A Molecular Beam Study of the Evaporation of Water from a Liquid Jet. *Zeitschrift für Phys. D Atoms, Mol. Clust.* **1988**, *10* (2–3), 269–277.

(91) Lam, R. K.; Shih, O.; Smith, J. W.; Sheardy, A. T.; Rizzuto, A. M.; Prendergast, D.; Saykally, R. J. Electrokinetic Detection for X-Ray Spectra of Weakly Interacting Liquids: N-Decane and N-Nonane. *J. Chem. Phys.* **2014**, *140* (23), 234202.

(92) Wilson, K. R.; Rude, B. S.; Smith, J.; Cappa, C.; Co, D. T.; Schaller, R. D.; Larsson, M.; Catalano, T.; Saykally, R. J. Investigation of Volatile Liquid Surfaces by Synchrotron X-Ray Spectroscopy of Liquid Microjets. *Rev. Sci. Instrum.* **2004**, *75* (3), 725–736.

(93) Wilson, K. R.; Schaller, R. D.; Co, D. T.; Saykally, R. J.; Rude, B. S.; Catalano, T.; Bozek, J. D. Surface Relaxation in Liquid Water and Methanol Studied by X-Ray Absorption Spectroscopy. *J. Chem. Phys.* **2002**, *117* (16), 7738.

(94) Ekimova, M.; Quevedo, W.; Faubel, M.; Wernet, P.; Nibbering, E. T. J. A Liquid Flatjet System for Solution Phase Soft-X-Ray Spectroscopy. *Struct. Dyn. (Melville, N.Y.)* **2015**, *2* (5), 54301.

(95) Lange, K. M.; Kothe, A.; Aziz, E. F. Chemistry in Solution: Recent Techniques and Applications Using Soft X-Ray Spectroscopy. *Phys. Chem. Chem. Phys.* **2012**, *14* (16), 5331–5338.

(96) Freiwald, M.; Cramm, S.; Eberhardt, W.; Eisebitt, S. Soft X-Ray Absorption Spectroscopy in Liquid Environments. *J. Electron Spectros. Relat. Phenomena* **2004**, *137–140* (SPEC. ISS.), 413–416.

(97) Nagasaka, M.; Hatsui, T.; Horigome, T.; Hamamura, Y.; Kosugi, N. Development of a Liquid Flow Cell to Measure Soft X-Ray Absorption in Transmission Mode: A Test for Liquid Water. *J. Electron Spectros. Relat. Phenomena* **2010**, *177* (2–3), 130–134.

(98) Näslund, L.-A.; Lüning, J.; Ufuktepe, Y.; Ogasawara, H.; Wernet, P.; Bergmann, U.; Pettersson, L. G. M.; Nilsson, A. X-Ray Absorption Spectroscopy Measurements of Liquid Water. *J. Phys. Chem. B* **2005**, *109* (28), 13835–13839.

(99) Guo, J.; Tong, T.; Svec, L.; Go, J.; Dong, C.; Chiou, J.-W. Soft-X-Ray Spectroscopy Experiment of Liquids. *J. Vac. Sci. Technol. A Vacuum, Surfaces, Film.* **2007**, *25* (4), 1231.

(100) Fuchs, O.; Maier, F.; Weinhardt, L.; Weigand, M.; Blum, M.; Zharnikov, M.; Denlinger, J.; Grunze, M.; Heske, C.; Umbach, E. A Liquid Flow Cell to Study the Electronic Structure of Liquids with Soft X-Rays. *Nucl. Instruments Methods Phys. Res. Sect. A Accel. Spectrometers, Detect. Assoc. Equip.* **2008**, *585* (3), 172–177.

(101) Schreck, S.; Gavrila, G.; Weniger, C.; Wernet, P. A Sample Holder for Soft X-Ray Absorption Spectroscopy of Liquids in Transmission Mode. *Rev. Sci. Instrum.* **2011**, *82* (10), 103101.

(102) Meibohm, J.; Schreck, S.; Wernet, P. Temperature Dependent Soft X-Ray Absorption Spectroscopy of Liquids. *Rev. Sci. Instrum.* **2014**, *85* (10), 103102.

(103) Bora, D. K.; Glans, P.-A.; Pepper, J.; Liu, Y.-S.; Du, C.; Wang, D.; Guo, J.-H. An Ultra-High Vacuum Electrochemical Flow Cell for in Situ/operando Soft X-Ray Spectroscopy Study. *Rev. Sci. Instrum.* **2014**, *85* (4), 43106.

(104) Velasco-Velez, J.-J.; Wu, C. H.; Pascal, T. A.; Wan, L. F.; Guo, J.; Prendergast, D.; Salmeron, M. The Structure of Interfacial Water on Gold Electrodes Studied by X-Ray Absorption Spectroscopy. *Science* **2014**, *346* (6211).

(105) Nagasaka, M.; Yuzawa, H.; Horigome, T.; Hitchcock, A. P.; Kosugi, N. Electrochemical Reaction of Aqueous Iron Sulfate Solutions Studied by Fe L-Edge Soft X-Ray Absorption Spectroscopy. *J. Phys. Chem. C* **2013**, *117* (32), 16343–16348.

(106) Nagasaka, M.; Yuzawa, H.; Horigome, T.; Kosugi, N. In Operando Observation System for Electrochemical Reaction by Soft X-Ray Absorption Spectroscopy with Potential Modulation Method. *Rev. Sci. Instrum.* **2014**, *85* (10).

(107) Nagasaka, M.; Ohigashi, T.; Kosugi, N. Local Structure Analysis of Electrochemical Reaction by Soft X-Ray Absorption Spectroscopy. *Bunseki Kagaku* **2015**, *64* (3), 163–172.

(108) Myneni, S.; Luo, Y.; Näslund, L. Å.; Cavalleri, M.; Ojamäe, L.; Ogasawara, H.; Pelmenschikov, A.; Wernet, P.; Väterlein, P.; Heske, C.; *et al.* Spectroscopic Probing of Local Hydrogen-Bonding Structures in Liquid Water. *J. Phys. Condens. Matter* **2002**, *14* (8), L213–L219.

(109) Smith, J. D.; Cappa, C. D.; Wilson, K. R.; Messer, B. M.; Cohen, R. C.; Saykally, R. J. Energetics of Hydrogen Bond Network Rearrangements in Liquid Water. *Science* **2004**, *306* (5697), 851–853.

(110) Smith, J. D.; Cappa, C. D.; Messer, B. M.; Drisdell, W. S.; Cohen, R. C.; Saykally, R. J. Probing the Local Structure of Liquid Water by X-Ray Absorption Spectroscopy. *J. Phys. Chem. B* **2006**, *110* (40), 20038–20045.

(111) Näslund, L.-A.; Edwards, D. C.; Wernet, P.; Bergmann, U.; Ogasawara, H.; Pettersson, L. G. M.; Myneni, S.; Nilsson, A. X-Ray Absorption Spectroscopy Study of the Hydrogen Bond Network in the Bulk Water of Aqueous Solutions. *J. Phys. Chem. A* **2005**, *109* (27), 5995–6002.

(112) Cavalleri, M.; Ogasawara, H.; Pettersson, L. G. .; Nilsson, A. The Interpretation of X-Ray Absorption Spectra of Water and Ice. *Chem. Phys. Lett.* **2002**, *364* (3–4), 363–370.

(113) Prendergast, D.; Galli, G. X-Ray Absorption Spectra of Water from First Principles Calculations. *Phys. Rev. Lett.* **2006**, *96* (21), 215502.

(114) Kühne, T. D.; Khaliullin, R. Z.; Bernal, J. D.; Fowler, R. H.; Stillinger, F. H.; Clark, G. N. I.; Cappa, C. D.; Smith, J. D.; Saykally, R. J.; Head-Gordon, T.; *et al.* Electronic Signature of the Instantaneous Asymmetry in the First Coordination Shell of Liquid Water. *Nat. Commun.* **2013**, *4*, 1450.

(115) Nordlund, D.; Ogasawara, H.; Bluhm, H.; Takahashi, O.; Odelius, M.; Nagasono, M.; Pettersson, L. G. M.; Nilsson, A. Probing the Electron Delocalization in Liquid Water and Ice at Attosecond Time Scales. *Phys. Rev. Lett.* **2007**, *99* (21), 217406.

(116) Smith, J. D.; Cappa, C. D.; Wilson, K. R.; Messer, B. M.; Cohen, R. C.; Saykally, R. J. Energetics of Hydrogen Bond Network Rearrangements in Liquid Water. *Science* **2004**, *306* (5697), 851–853.

(117) Head-Gordon, T.; Johnson, M. E. Tetrahedral Structure or Chains for Liquid Water. *Proc. Natl. Acad. Sci. U. S. A.* **2006**, *103* (21), 7973–7977.

(118) Nilsson, A.; Wernet, P.; Nordlund, D.; Bergmann, U.; Cavalleri, M.; Odelius, M.; Ogasawara, H.; Näslund, L.-Å.; Hirsch, T. K.; Ojamäe, L.; *et al.* Comment on "Energetics of Hydrogen Bond Network Rearrangements in Liquid Water"; *Science* **2005**, *308* (5723).

(119) Odelius, M.; Cavalleri, M.; Nilsson, A.; Pettersson, L. G. M. X-Ray Absorption Spectrum of Liquid Water from Molecular Dynamics Simulations: Asymmetric Model. *Phys. Rev. B* **2006**, *73* (2), 24205.

(120) Huang, C.; Wikfeldt, K. T.; Tokushima, T.; Nordlund, D.; Harada, Y.; Bergmann, U.; Niebuhr, M.; Weiss, T. M.; Horikawa, Y.; Leetmaa, M.; *et al.* The Inhomogeneous Structure of Water at Ambient Conditions. *Proc. Natl. Acad. Sci. U.S.A.* **2009**, *106* (36), 15214–15218.

(121) Iannuzzi, M. X-Ray Absorption Spectra of Hexagonal Ice and Liquid Water by All-Electron Gaussian and Augmented Plane Wave Calculations. *J. Chem. Phys.* **2008**, *128* (20), 204506.

(122) Vinson, J.; Kas, J. J.; Vila, F. D.; Rehr, J. J.; Shirley, E. L. Theoretical Optical and X-Ray Spectra of Liquid and Solid H_2O. *Phys. Rev. B* **2012**, *85* (4), 45101.

(123) Pylkkänen, T.; Sakko, A.; Hakala, M.; Hämäläinen, K.; Monaco, G.; Huotari, S. Temperature Dependence of the near-Edge Spectrum of Water. *J. Phys. Chem. B* **2011**, *115* (49), 14544–14550.

(124) Fukui, H.; Huotari, S.; Andrault, D.; Kawamoto, T. Oxygen K-Edge Fine Structures of Water by X-Ray Raman Scattering Spectroscopy under Pressure Conditions. *J. Chem. Phys.* **2007**, *127* (13), 134502.

(125) Lange, K. M.; Hodeck, K. F.; Schade, U.; Aziz, E. F. Nature of the Hydrogen Bond of Water in Solvents of Different Polarities. *J. Phys. Chem. B* **2010**, *114* (50), 16997–17001.

(126) Lange, K. M.; Könnecke, R.; Soldatov, M.; Golnak, R.; Rubensson, J.-E.; Soldatov, A.; Aziz, E. F. On the Origin of the Hydrogen-Bond-Network Nature of Water: X-Ray Absorption and Emission Spectra of Water-Acetonitrile Mixtures. *Angew. Chem. Int. Ed. Engl.* **2011**, *50* (45), 10621–10625.

(127) Lange, K. M.; Soldatov, M.; Golnak, R.; Gotz, M.; Engel, N.; Könnecke, R.; Rubensson, J.-E.; Aziz, E. F. X-Ray Emission from Pure and Dilute H_2O and D_2O in a Liquid Microjet: Hydrogen Bonds and Nuclear Dynamics. *Phys. Rev. B* **2012**, *85* (15), 155104.

(128) Venables, D. S.; Schmuttenmaer, C. A. Spectroscopy and Dynamics of Mixtures of Water with Acetone, Acetonitrile, and Methanol. *J. Chem. Phys.* **2000**, *113* (24), 11222.

(129) Tokushima, T.; Horikawa, Y.; Takahashi, O.; Arai, H.; Sadakane, K.; Harada, Y.; Takata, Y.; Shin, S. Solvation Dependence of Valence Electronic States of Water Diluted in Organic Solvents Probed by Soft X-Ray Spectroscopy. *Phys. Chem. Chem. Phys.* **2014**, *16* (22), 10753–10761.

(130) Bergmann, U.; Nordlund, D.; Wernet, P.; Odelius, M.; Pettersson, L. G. M.; Nilsson, A. Isotope Effects in Liquid Water Probed by X-Ray Raman Spectroscopy. *Phys. Rev. B* **2007**, *76* (2), 24202.

(131) Nordlund, D.; Ogasawara, H.; Andersson, K. J.; Tatarkhanov, M.; Salmerón, M.; Pettersson, L. G. M.; Nilsson, A. Sensitivity of X-Ray Absorption Spectroscopy to Hydrogen Bond Topology. *Phys. Rev. B* **2009**, *80* (23), 233404.

(132) Näslund, L.-Å.; Cavalleri, M.; Ogasawara, H.; Nilsson, A.; Pettersson, L. G. M.; Wernet, P.; Edwards, D. C.; Sandström, M.; Myneni, S. Direct Evidence of Orbital Mixing between Water and Solvated Transition-Metal Ions: An Oxygen 1s XAS and DFT Study of Aqueous Systems. *J. Phys. Chem. A* **2003**, *107* (35), 6869–6876.

(133) Guo, J.-H.; Augustsson, A.; Kashtanov, S.; Spångberg, D.; Nordgren, J.; Hermansson, K.; Luo, Y. The Interaction of Cations and Liquid Water Studied by Resonant Soft-X-Ray Absorption and Emission Spectroscopy. *J. Electron Spectros. Relat. Phenomena* **2005**, *144–147*, 287–290.

(134) Cappa, C. D.; Smith, J. D.; Messer, B. M.; Cohen, R. C.; Saykally, R. J. Effects of Cations on the Hydrogen Bond Network of Liquid Water: New Results from X-Ray Absorption Spectroscopy of Liquid Microjets. *J. Phys. Chem. B* **2006**, *110* (11), 5301–5309.

(135) Aziz, E. F.; Ottosson, N.; Eisebitt, S.; Eberhardt, W.; Jagoda-Cwiklik, B.; Vácha, R.; Jungwirth, P.; Winter, B. Cation-Specific Interactions with Carboxylate in Amino Acid and Acetate Aqueous Solutions: X-Ray Absorption and Ab Initio Calculations. *J. Phys. Chem. B* **2008**, *112* (40), 12567–12570.

(136) Cappa, C. D.; Smith, J. D.; Messer, B. M.; Cohen, R. C.; Saykally, R. J. The Electronic Structure of the Hydrated Proton: A Comparative X-Ray Absorption Study of Aqueous HCl and NaCl Solutions. *J. Phys. Chem. B* **2006**, *110* (3), 1166–1171.

(137) Chen, C.; Huang, C.; Waluyo, I.; Nordlund, D.; Weng, T.-C.; Sokaras, D.; Weiss, T.; Bergmann, U.; Pettersson, L. G. M.; Nilsson, A. Solvation Structures of Protons and Hydroxide Ions in Water. *J. Chem. Phys.* **2013**, *138* (15), 154506.

(138) Schwartz, C. P.; Uejio, J. S.; Duffin, A. M.; Drisdell, W. S.; Smith, J. D.; Saykally, R. J. Soft X-Ray Absorption Spectra of Aqueous Salt Solutions with Highly Charged Cations in Liquid Microjets. *Chem. Phys. Lett.* **2010**, *493* (1–3), 94–96.

(139) Wertz, D. L.; Kruh, R. K. Reinvestigation of the Structures of Ethanol and Methanol at Room Temperature. *J. Chem. Phys.* **1967**, *47* (2), 388–390.

(140) Weitkamp, T.; Neuefeind, J.; Fischer, H. E.; Zeidler, M. D. Hydrogen Bonding in Liquid Methanol at Ambient Conditions and at High Pressure. *Mol. Phys.* **2000**, *98* (3), 125–134.

(141) Guo, J.-H.; Luo, Y.; Augustsson, A.; Kashtanov, S.; Rubensson, J.-E.; Shuh, D.; Zhuang, V.; Ross, P.; Ågren, H.; Nordgren, J. The Molecular Structure of Alcohol-Water Mixtures Determined by Soft-X-Ray Absorption and Emission Spectroscopy. *J. Electron Spectros. Relat. Phenomena* **2004**, *137–140* (SPEC. ISS.), 425–428.

(142) Wilson, K. R.; Cavalleri, M.; Rude, B. S.; Schaller, R. D.; Catalano, T.; Nilsson, A.; Saykally, R. J.; Pettersson, L. G. M. X-Ray Absorption Spectroscopy of Liquid Methanol Microjets: Bulk Electronic Structure and Hydrogen Bonding Network. *J. Phys. Chem. B* **2005**, *109* (20), 10194–10203.

(143) Pylkkänen, T.; Lehtola, J.; Hakala, M.; Sakko, A.; Monaco, G.; Huotari, S.; Hämäläinen, K. Universal Signature of Hydrogen Bonding in the Oxygen K-Edge Spectrum of Alcohols. *J. Phys. Chem. B* **2010**, *114* (41), 13076–13083.

(144) Nagasaka, M.; Mochizuki, K.; Leloup, V.; Kosugi, N. Local Structures of Methanol-Water Binary Solutions Studied by Soft X-Ray Absorption Spectroscopy. *J. Phys. Chem. B* **2014**, *118* (16), 4388–4396.

(145) Lam, R. K.; Smith, J. W.; Saykally, R. J. Communication: Hydrogen Bonding Interactions in Water-Alcohol Mixtures from X-Ray Absorption Spectroscopy. *J. Chem. Phys.* **2016**, *144* (19), 191103.

(146) Prince, K.C.; Richter, R.; de Simone, M.; Alagia, M.; Coreno, M. Near Edge X-Ray Absorption Spectra of Some Small Polyatomic Molecules. *J. Phys. Chem. A* **2003**, *107* (12), 1955.

(147) Butler, J. A. V; Thomson, D. W.; Maclennan, W. H. 173. The Free Energy of the Normal Aliphatic Alcohols in Aqueous Solution. Part I. The Partial Vapour Pressures of Aqueous Solutions of Methyl{,} N-Propyl{,} and N-Butyl Alcohols. Part II. The Solubilities of Some Normal Aliphatic Alcohols in Water. Part . *J. Chem. Soc.* **1933**, No. 0, 674–686.

(148) Duffin, A. M.; Schwartz, C. P.; England, A. H.; Uejio, J. S.; Prendergast, D.; Saykally, R. J. pH-Dependent X-Ray Absorption Spectra of Aqueous Boron Oxides. *J. Chem. Phys.* **2011**, *134* (15), 154503.

(149) Smith, J. W.; Lam, R. K.; Shih, O.; Rizzuto, A. M.; Prendergast, D.; Saykally, R. J. Properties of Aqueous Nitrate and Nitrite from X-Ray Absorption Spectroscopy. *J. Chem. Phys.* **2015**, *143* (8), 84503.

(150) Aziz, E. F.; Zimina, A.; Freiwald, M.; Eisebitt, S.; Eberhardt, W. Molecular and Electronic Structure in NaCl Electrolytes of Varying Concentration: Identification of Spectral Fingerprints. *J. Chem. Phys.* **2006**, *124* (11), 114502.

(151) Aziz, E. F.; Eisebitt, S.; Eberhardt, W.; Cwiklik, L.; Jungwirth, P. Existence of Oriented Ion-Hydroxide Clusters in Concentrated Aqueous NaCl Solution at pH 13. *J. Phys. Chem. B* **2008**, *112* (4), 1262–1266.

(152) Aziz, E. F.; Eisebitt, S.; de Groot, F.; Chiou, J. W.; Dong, C.; Guo, J.; Eberhardt, W. Direct Contact versus Solvent-Shared Ion Pairs in $NiCl_2$ Electrolytes Monitored by Multiplet Effects at Ni(II) L Edge X-Ray Absorption. *J. Phys. Chem. B* **2007**, *111* (17), 4440–4445.

(153) Uejio, J. S.; Schwartz, C. P.; Duffin, A. M.; Drisdell, W. S.; Cohen, R. C.; Saykally, R. J. Characterization of Selective Binding of Alkali Cations with Carboxylate by X-Ray Absorption Spectroscopy of Liquid Microjets. *Proc. Natl. Acad. Sci. U. S. A.* **2008**, *105* (19), 6809–6812.

(154) Vrbka, L.; Vondrásek, J.; Jagoda-Cwiklik, B.; Vácha, R.; Jungwirth, P. Quantification and Rationalization of the Higher Affinity of Sodium over Potassium to Protein Surfaces. *Proc. Natl. Acad. Sci. U. S. A.* **2006**, *103* (42), 15440–15444.

(155) Tabayashi, K.; Yamamoto, K.; Maruyama, T.; Yoshida, H.; Okada, K.; Tamenori, Y.; Suzuki, I. H.; Gejo, T.; Honma, K. Core-Electron Excitation and Fragmentation Processes of Hydrogen Bonded Acetic-Acid Clusters in the Oxygen K-Edge Region. **2011**, *184* (3–6), 134–139.

(156) Horikawa, Y.; Arai, H.; Tokushima, T.; Shin, S. Spectral Fingerprint in X-Ray Absorption for Hydrogen-Bonded Dimer Formation of Acetic Acids in Solution. *Chem. Phys. Lett.* **2012**, *522*, 33–37.

(157) Tokushima, T.; Horikawa, Y.; Harada, Y.; Takahashi, O.; Hiraya, A.; Shin, S. Selective Observation of the Two Oxygen Atoms at Different Sites in the Carboxyl Group (–COOH) of Liquid Acetic Acid. *Phys. Chem. Chem. Phys.* **2009**, *11* (11), 1679.

(158) Shih, O.; England, A. H.; Dallinger, G. C.; Smith, J. W.; Duffey, K. C.; Cohen, R. C.; Prendergast, D.; Saykally, R. J. Cation-Cation Contact Pairing in Water: Guanidinium. *J. Chem. Phys.* **2013**, *139* (3), 35104.

(159) Lange, K. M.; Bergmann, U.; Hodeck, K. F.; Könnecke, R.; Schade, U.; Aziz, E. F. Shared Solvation of Sodium Ions in Alcohol-Water Solutions Explains the Non-Ideality of Free Energy of Solvation. *Phys. Chem. Chem. Phys.* **2011**, *13* (34), 15423–15427.

(160) Bonhommeau, S.; Ottosson, N.; Pokapanich, W.; Svensson, S.; Eberhardt, W.; Björneholm, O.; Aziz, E. F. Solvent Effect of Alcohols at the L-Edge of Iron in Solution: X-Ray Absorption and Multiplet Calculations. *J. Phys. Chem. B* **2008**, *112* (40), 12571–12574.

(161) Smith, J. W.; Lam, R. K.; Sheardy, A. T.; Shih, O.; Rizzuto, A. M.; Borodin, O.; Harris, S. J.; Prendergast, D.; Saykally, R. J. X-Ray Absorption Spectroscopy of $LiBF_4$ in Propylene Carbonate: A Model Lithium Ion Battery Electrolyte. *Phys. Chem. Chem. Phys.* **2014**, *16* (43), 23568–23575.

(162) England, A. H.; Duffin, A. M.; Schwartz, C. P.; Uejio, J. S.; Prendergast, D.; Saykally, R. J. On the Hydration and Hydrolysis of Carbon Dioxide. *Chem. Phys. Lett.* **2011**, *514* (4–6), 187–195.

(163) Lam, R. K.; England, A. H.; Sheardy, A. T.; Shih, O.; Smith, J. W.; Rizzuto, A. M.; Prendergast, D.; Saykally, R. J. The Hydration Structure of Aqueous Carbonic Acid from X-Ray Absorption Spectroscopy. *Chem. Phys. Lett.* **2014**, *614*, 282–286.

(164) Lam, R. K.; England, A. H.; Smith, J. W.; Rizzuto, A. M.; Shih, O.; Prendergast, D.; Saykally, R. J. The Hydration Structure of Dissolved Carbon Dioxide from X-Ray Absorption Spectroscopy. *Chem. Phys. Lett.* **2015**, *633*, 214–217.

(165) Messer, B. M.; Cappa, C. D.; Smith, J. D.; Drisdell, W. S.; Schwartz, C. P.; Cohen, R. C.; Saykally, R. J. Local Hydration Environments of Amino Acids and Dipeptides Studied by X-Ray Spectroscopy of Liquid Microjets. *J. Phys. Chem. B* **2005**, *109* (46), 21640–21646.

(166) Messer, B. M.; Cappa, C. D.; Smith, J. D.; Wilson, K. R.; Gilles, M. K.; Cohen, R. C.; Saykally, R. J. pH Dependence of the Electronic Structure of Glycine. *J. Phys. Chem. B* **2005**, *109* (11), 5375–5382.

(167) Uejio, J. S.; Schwartz, C. P.; Duffin, A. M.; England, A.; Prendergast, D.; Saykally, R. J. Monopeptide versus Monopeptoid: Insights on Structure and Hydration of Aqueous Alanine and Sarcosine via X-Ray Absorption Spectroscopy. *J. Phys. Chem. B* **2010**, *114* (13), 4702–4709.

(168) Aziz, E. F.; Ottosson, N.; Bonhommeau, S.; Bergmann, N.; Eberhardt, W.; Chergui, M. Probing the Electronic Structure of the Hemoglobin Active Center in Physiological Solutions. *Phys. Rev. Lett.* **2009**, *102* (6), 68103.

(169) Bergmann, N.; Bonhommeau, S.; Lange, K. M.; Greil, S. M.; Eisebitt, S.; de Groot, F.; Chergui, M.; Aziz, E. F. On the Enzymatic Activity of Catalase: An Iron L-Edge X-Ray Absorption Study of the Active Centre. *Phys. Chem. Chem. Phys.* **2010**, *12* (18), 4827–4832.

(170) Schwartz, C. P.; Uejio, J. S.; Duffin, A. M.; England, A. H.; Kelly, D. N.; Prendergast, D.; Saykally, R. J. Investigation of Protein Conformation and Interactions with Salts via X-Ray Absorption Spectroscopy. *Proc. Natl. Acad. Sci. U. S. A.* **2010**, *107* (32), 14008–14013.

(171) MacNaughton, J. B.; Yablonskikh, M. V.; Hunt, A. H.; Kurmaev, E. Z.; Lee, J. S.; Wettig, S. D.; Moewes, A. Solid versus Solution: Examining the Electronic Structure of Metallic DNA with Soft X-Ray Spectroscopy. *Phys. Rev. B* **2006**, *74* (12), 125101.

(172) Ukai, M.; Yokoya, A.; Fujii, K.; Saitoh, Y. X-Ray Absorption Spectrum for Guanosine--Monophosphate in Water Solution in the Vicinity of the Nitrogen K-Edge Observed in Free Liquid Jet in Vacuum. *Radiat. Phys. Chem.* **2008**, *77* (10–12), 1265–1269.

(173) Guo, J.-H.; Kastanov, S.; Soderstrom, J.; Glans, P.-A.; West, M.; Learmonth, T.; Chiou, J.-W.; Luo, Y.; Nordgren, J.; Smith, K.; *et al.* Electronic Structure Study of the Bases in DNA Duplexes by in Situ Photon-In/photon-out Soft X-Ray Spectroscopy. *J. Electron Spectros. Relat. Phenomena* **2010**, *181* (2–3), 197–201.

(174) Kelly, D. N.; Schwartz, C. P.; Uejio, J. S.; Duffin, A. M.; England, A. H.; Saykally, R. J. Communication: Near Edge X-Ray Absorption Fine Structure Spectroscopy of Aqueous Adenosine Triphosphate at the Carbon and Nitrogen K-Edges. *J. Chem. Phys.* **2010**, *133* (10), 101103.

(175) de Groot, F. Multiplet Effects in X-Ray Spectroscopy. *Coord. Chem. Rev.* **2005**, *249* (1), 31–63.

(176) de Groot, F. M. F. Ligand and Metal X-Ray Absorption in Transition Metal Complexes. *Inorganica Chim. Acta* **2008**, *361* (4), 850–856.

(177) Lange, K. M.; Golnak, R.; Bonhommeau, S.; Aziz, E. F. Ligand Discrimination of Myoglobin in Solution: An Iron L-Edge X-Ray Absorption Study of the Active Centre. *Chem. Commun.* **2013**, *49* (39), 4163.

(178) Aziz, E. F. X-Ray Spectroscopies Revealing the Structure and Dynamics of Metalloprotein Active Centers. *J. Phys. Chem. Lett.* **2011**, *2* (4), 320–326.

Chapter 3: X-Ray Absorption Spectroscopy of $LiBF_4$ in Alkyl Carbonates

Material from this chapter has been reproduced from

Smith, J. W.; Lam, R. K.-J.; Sheardy, A. T.; Shih, O.; Rizzuto, A. M.; Borodin, O.; Harris, S. J.; Prendergast, D.; Saykally, R. J. "X-Ray Absorption Spectroscopy of LiBF4 in Propylene Carbonate: A Model Lithium Ion Battery Electrolyte." *Phys. Chem. Chem. Phys.* **2014**.

published by the PCCP Owner Societies, with permission from all co-authors under a Creative Commons license.

I. Abstract

Since their introduction into the commercial marketplace in 1991, lithium ion batteries have become increasingly ubiquitous in portable technology. Nevertheless, improvements to existing battery technology are necessary to expand their utility for larger-scale applications, such as electric vehicles. Advances may be realized from improvements to the liquid electrolyte; however, current understanding of the liquid structure and properties remain incomplete. X-ray absorption spectroscopy of solutions of $LiBF_4$ in propylene carbonate (PC), ethylene carbonate (EC), and dimethyl carbonate (DMC), interpreted using first-principles electronic structure calculations within the eXcited electron and Core Hole (XCH) approximation, yields new insight into the solvation structure of the Li^+ ion in alkyl carbonate solutions. By generating linear combinations of the computed spectra of Li^+-associating and free PC molecules and comparing to the experimental spectrum of 1M $LiBF_4$ in PC, we find a Li^+-solvent interaction number of 4.5. This result suggests that computational models of lithium ion battery electrolytes should move beyond tetrahedral coordination structures.

II. Introduction

Lithium ion batteries (LIBs) have rapidly grown to dominate the rechargeable battery market for portable technology. Given the simultaneous expansion of the market for handheld devices (i.e. cellular phones, laptops, tablets, etc.), LIBs now comprise a multibillion dollar industry.[1] Such demand has spurred intense research and development efforts.[2] Nevertheless, serious shortcomings persist which limit the utility of modern LIBs for larger-scale applications in electric vehicles (EVs) or for power storage utilized in conjunction with intermittent renewable energy sources (wind, solar, etc.).[2–4] These shortcomings include high cost, energy density below optimal EV standards, slow recharging rates, and limited lifetimes.

A typical commercial LIB consists of a graphite negative electrode and metal oxide or metal phosphate positive electrode (e.g. $LiCoO_2$, $LiFePO_4$, $LiMnO_2$, etc.). Charge is transported by lithium ions travelling between the electrodes through a liquid electrolyte commonly consisting of a lithium salt with a large, charge-disperse anion such as PF_6^-, BF_4^-, ClO_4^-, or more recently larger, carbon-based anions such as bis(oxalato)borate {$B(C_2O_4)_2^-$; BOB^-} dissolved in a non-aqueous solvent. These solvents typically consist of combinations of linear alkyl carbonate molecules such as dimethyl carbonate (DMC) and ethyl methyl carbonate (EMC), and the cyclic alkyl carbonate ethylene carbonate (EC). Propylene carbonate (PC), a structural analogue of EC with a methyl group on a ring carbon, is unsuitable for use in commercial batteries, as it

penetrates and ultimately damages the graphite electrode. Oxidation and reduction of the liquid electrolyte at the electrodes during initial cycling results in the formation of the "solid-electrolyte interphase (SEI),"[5–9] consuming liquid electrolyte and incorporating some of the Li^+ charge carriers from the cell. This passivating layer is thought to grow until it has become sufficiently resistive to fully restrict electron transfer between the electrode and liquid electrolyte while allowing passage of Li^+.[3] Thereafter, minimal damage occurs in the liquid electrolyte.

A great deal of effort has been dedicated to investigation of the electrodes and associated SEI of LIBs and the transport of Li^+ through these media.[2,5,6,10–14] Substantially less study has been directed towards the liquid electrolyte.[15] It is becoming increasingly clear, however, that the structure of the liquid electrolyte substantially influences the function of LIBs, and that improvements to the liquid electrolyte are an essential component of the overall effort to improve LIBs for use in EVs and large-scale energy storage. Several studies have demonstrated that the solvation environment of the lithium ion in the electrolyte dictates the formation mechanism and resulting structure of the SEI.[7,16–18] This is significant for a number of reasons: SEI growth consumes Li^+, produces a high-resistivity region through which ions must migrate, and is widely implicated as the region of the battery in which failure is most likely to occur.[19] Furthermore, recent studies by Xu *et al.* have suggested that the desolvation of the Li^+ from the liquid electrolyte is the slow step in Li^+ insertion into the electrodes, thus comprising a critical limitation on power density and recharging rates.[20,21] Clearly, improvements in the electrolytic properties will improve nearly all significant aspects of LIB performance, including energy and power density, recharge time, and cycle life.

In order to realize the performance enhancements from improved electrolytes, it is necessary to thoroughly understand the electrolyte structure. Unfortunately, while a number of studies have been performed on LIB electrolyte systems, a clear picture of the solvation structure of the Li^+ ion in alkyl carbonate solutions remains elusive. For example, several experimental and theoretical studies have suggested that a substantial degree of ion pairing/aggregation exists between Li^+ and the counterion (BF_4^-, ClO_4^-, PF_6^-) at concentrations of ~1M (1 mol/dm^3), the approximate solution concentration in standard commercial LIBs.[22–25] Other studies of the electrochemical properties and infrared and Raman spectra of the same solutions and concentrations have suggested little or no ion pairing or aggregation.[16,26,27] Similarly, the interactions of the ions with the solvent remain incompletely characterized. The generally favored structure comprises a tetrahedral coordination of carbonyl oxygen atoms around the Li^+ and weakly solvated counterions. Numerous experimental and theoretical studies have found total coordination numbers for Li^+ (Li-O + Li-counterion interactions) very near four.[8,25,28,29] However, several vibrational spectroscopy studies (infrared absorption, Raman) of LIB electrolytes have suggested Li^+ coordination numbers between 4 and 5.[16,30,31] A study published by Kondo *et al.* utilized conductivity measurements to estimate the coordination number of Li^+ in PC at 4.3.[27] Neutron diffraction studies by Kameda *et al.* have found a Li-O coordination number of 4.5 in the same electrolyte solution.[32] Bogle *et al.* have interpreted the chemical shifts in ^{17}C NMR to ascertain a Li-O coordination number of 5.69 for $LiPF_6$ in EC,[33] while at least one study utilizing NMR diffusivity measurements has estimated a coordination number for Li^+ as $LiClO_4$ in EC to be ~7 in concentrations up to ~1M.[34]

Here we investigate the coordination structure of Li^+ in solutions of $LiBF_4$ in PC and a 50:50 (by mole ratio) mixture of EC:DMC using x-ray absorption spectroscopy (XAS) of liquid microjets.[35] XAS is an atom-specific core-level spectroscopic probe of the unoccupied electronic states; as such, it is sensitive to both the intra- and intermolecular environment of the target atom.

Experimental spectra in PC solution are interpreted through utilization of molecular dynamics simulations and spectral simulations computed using the Prendergast-Galli eXcited electron and Core Hole (XCH) methodology.[36] Previous studies in our group have used these experimental and theoretical techniques to investigate the structure and chemistry of a variety of aqueous solutions.[37–40] Here, we extend the methodology to a non-aqueous system of substantial practical utility for the purpose of understanding and improving the solvation properties and desolvation process of the Li^+ ion in LIB electrolytes.

III. Experimental and Theoretical Methods

a. X-ray spectroscopy of Liquid Microjects

$LiBF_4$, PC, EC, and DMC were obtained from Sigma Aldrich and had minimum purity of 98%, 99.7%, 99%, and 98%, respectively. PC was stored under dry nitrogen until use. A mixture of 50:50 EC:DMC by mole ratio was produced volumetrically in atmosphere and was not stored under an inert gas. X-ray absorption spectra of PC solutions were collected at Beamline 8.0.1 of the Advanced Light Source at Lawrence Berkeley National Laboratory (Berkeley, CA); this beamline has a nominal maximum output of 6×10^{15} photons/s with resolving power $E/\Delta E$ of 7000. XA spectra of EC:DMC solutions were collected at Beamline 6.0.2. As this beamline was designed with a chopper for time-resolved studies, the photon flux to the sample is substantially lower than that at Beamline 8.0.1. Liquid jets are produced by forcing pressurized (~15 bar) liquids through a 100 μm inner diameter silica capillary into a vacuum chamber (10^{-5} torr), where they interact with the x-ray beamline. Total electron yield (TEY) XA spectra are collected on a 2.1 kV biased copper as a function of photon energy. Our previous work has demonstrated that spectra obtained in this manner are representative of the bulk liquid.[41,42] Spectra are normalized to the signal collected simultaneously on a high-transmission gold grid intersecting the beamline several meters before it is focused into the chamber. Unlike previous work published by our group, this paper presents liquid spectra without gas-phase background subtraction; the low vapor pressure of PC (<2 torr at 298K) renders the gas phase spectrum insignificant, accounting for <0.2% of total intensity. Full XA spectra of the carbon and oxygen K-edges were collected with 0.2 eV step sizes and 1s count times; detailed spectra of the oxygen K-edge were collected with 0.05 eV steps and 2s count times. Single-point energy axis calibrations were performed using gas-phase carbon dioxide for the carbon K-edge and liquid water for the oxygen K-edge. A more complete description of the experiment can be found in a prior publication.[35]

b. Molecular Dynamics Simulations

A many-body polarizable force field (FF) APPLE&P[43] (Atomistic Polarizable Potential for Liquids, Electrolytes, and Polymers) has been used for molecular dynamics (MD) simulations of PC and (PC)$LiBF_4$ electrolytes. APPLE&P utilizes an exp-6 form for description of non-bonded interactions, also called the Buckingham potential, in conjunction with permanent charges situated on atomic sites and off-ether oxygen atomic sites for PC. The many-body polarization interactions are represented by the induced isotropic atomic dipoles and were solved self-consistently. The short-range interaction between induced dipoles is screened using Thole methodology with the Thole parameter (a_T=0.4). Atoms connected by bonds (1-2) and bends (1-2-3) were excluded from the list of non-bonded interactions. Atoms connected by 3 or more

bonds had full non-bonded interactions with the exception that 1-4 interaction between permanent charges and induced dipoles were scaled by 0.8. A detailed discussion of the functional form is provided elsewhere.[43] Previously developed PC and PC/Li^+ force field parameters were used.[44,45] APPLE&P parameters[46] for $LiBF_4$ were modified by refitting BF_4^- charges to electrostatic potential around anion obtained at MP2/aug-cc-pvTz level, while Li…F repulsion parameters were refit to Li^+/BF_4^- binding energy obtained at the same level. The revised force field version was denoted as "e44." The revised force field yielded ion self-diffusion coefficients and ionic conductivity of PC($LiBF_4$) electrolytes in excellent agreement with experiments (see Table 1).

We closely followed the simulation methodology previously used in MD simulations of electrolytes containing lithium salts.[45,46] Two PC-$LiBF_4$ systems have been constructed: a *large* simulation cell containing 640 PC and 64 $LiBF_4$, and a *small* simulation cell containing 20 PC and 2 $LiBF_4$. Simulations were performed at 298 K. Equilibration runs were 6 ns at 333 K followed by 3 ns and 6 ns equilibration runs in NPT ensemble at 298 K for the large and small systems, respectively. The density of the large box was imposed upon the small box to compensate for large density fluctuations arising from the small sample size. Production runs were performed for 8.3 ns and 1 ns for the large and small systems, respectively, in the NVT ensemble. The cutoff for non-bonded interactions was set to 12 Å for the large box and at half a box for the small simulation cell. Snapshots of the molecular configurations of the small simulation box were saved at 20 ps intervals for the spectral simulations. Snapshots from a small box containing 20 PC were generated following the same methods.

Table S1: Comparison of large and small MD simulation box properties to previously published experimental findings of Takeuchi *et al.*[23]

	Large Box	Small Box	Experiment[23]
# PC in MD box	640	20	
# $LiBF_4$ in MD box	64	2	
Concentration (mol/L)	1.13	1.13	1.00
Concentration (mol/kg)	1.03	1.03	
Length of equilibration (ns)	3.2	6	
Length of the run (ns)	5.55	0.6	
Density (kg/m^3)	1257	1261	1251
D, solvent (1e-6 cm^2/s)	2.47118		2.2
D, anion (1e-6 cm^2/s)	1.06465		1.5
D, Li+ (1e-6 cm^2/s)	0.901052		0.9
Conductivity, no Finite Size Correction (mS/cm)	3.412459		3.6
Conductivity, hydro-corrected (mS/cm)	4.301659		3.6
dynamic degree of dissociation	0.41		0.4
fraction of free Li (r Li-B > 3.6 Å)	0.16	0.008	
fraction of free B (r Li-B > 3.6 Å)	0.06	0	

c. Spectral Simulations

Simulated spectra of the oxygen K-edge of PC and the (PC)$LiBF_4$ electrolyte were calculated using the XCH approximation,[36] a first-principles constrained-occupancy density functional theory (DFT) calculation, using molecular coordinates sampled from the small box

MD simulations described above. DFT calculations were performed under periodic boundary conditions using the Plane Wave Self-Consistent Field (PWSCF) program within the Quantum-ESPRESSO package,[47] employing the Pardew-Burke-Ernzerhof form of the Generalized Gradient Approximation to the exchange-correlation potential.[48] The plane wave basis set, with a 25 Ry kinetic energy cutoff, is sufficiently flexible to model both localized and delocalized Kohn-Sham orbitals in the XCH approximation to the core-excited states. The electron density of the lowest energy core-excited state was generated self-consistently with explicit inclusion of a core hole on a target oxygen atom, modeled with a suitably modified pseudopotential, together with the inclusion of the excited electron in the first available valence orbital. Higher energy excited states were approximated using the unoccupied Kohn-Sham orbitals of the XCH self-consistent field. Transition matrix elements were computed within Fermi's Golden Rule between the 1s atomic orbital of the ground state and the unoccupied orbitals from the XCH calculation. Resulting transitions were broadened via Gaussian convolution using a fixed linewidth parameter of 0.2 eV to produce the final simulated spectrum. Spectra obtained from independent excited atoms and/or MD snapshots were aligned based on an isolated atomic reference, utilizing a previously-published methodology,[39] using the spectrum of gaseous CO_2 to provide a single-point energy alignment to experiment.

IV. Results and Discussion

a. XAS of PC and (PC)$LiBF_4$

The TEY XA spectra collected for the carbon and oxygen K-edges of neat PC and 1M $LiBF_4$ in PC are shown in Figures 1 and 2, respectively. As the carbon K-edge spectrum exhibits no significant changes upon addition of the lithium salt, no additional analysis has been performed for these spectra. However, several features in the oxygen K-edge spectrum exhibit a blue shift in the (PC)$LiBF_4$ electrolyte relative to the analogous features in the spectrum of the neat solvent. Detailed spectra on the first sharp feature in the oxygen K-edge spectra, near 533.5 eV, were collected for neat PC and solutions of 0.25, 0.5, and 1.0 M $LiBF_4$ in PC (Figure 3). This feature exhibits a progressive blue shift, increasing as a function of $LiBF_4$ concentration, with a total shift of 0.07 eV from neat PC to the 1M solution. As this spectral feature is much sharper and more clearly defined than those near 538 and 543 eV, which also exhibit blue shifts upon addition of the lithium salt, we have chosen to focus our analysis on this region of the spectrum.

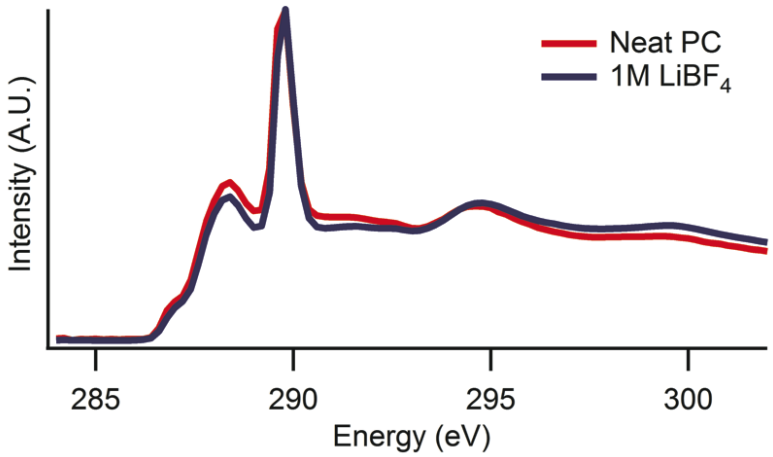

Figure 1: Experimental carbon K-edge XA spectra of propylene carbonate (PC) and 1M (PC)$LiBF_4$. The PC spectrum does not exhibit any significant change upon addition of the lithium salt.

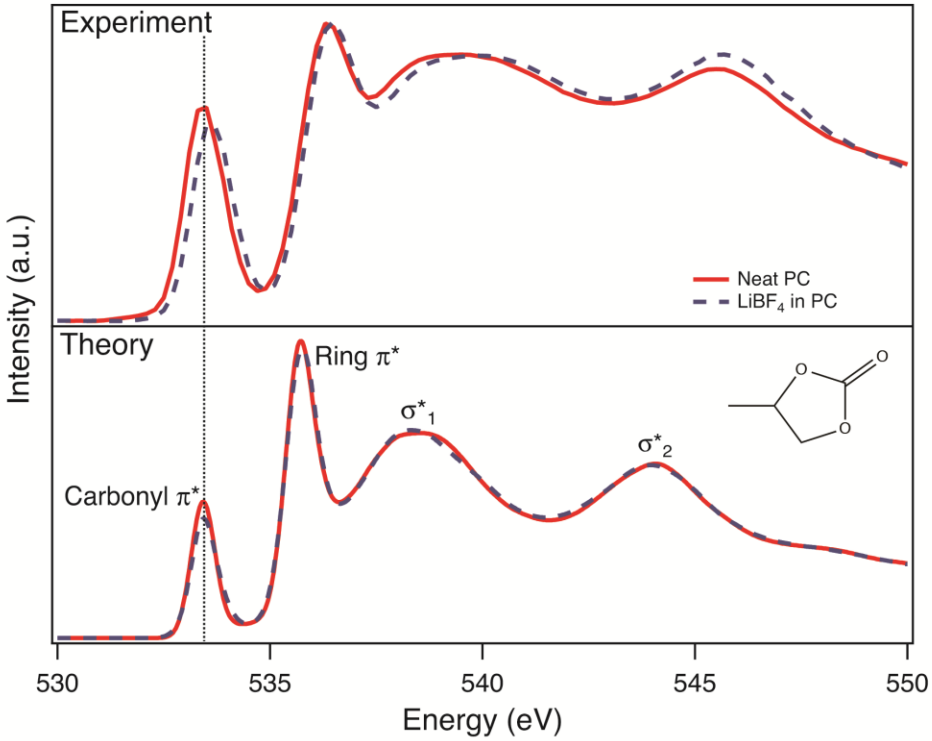

Figure 2: Experimental and calculated oxygen K-edge XA spectra of PC and (PC)$LiBF_4$. The black dotted line corresponds to the center of a Gaussian fit performed on the carbonyl π* feature of the experimental spectrum of neat PC. Features are labeled with their character as assigned from isosurfaces of the final states. The calculated PC spectrum accurately reproduces the experimental spectrum, but the blue shift observed in the experimental spectrum upon addition of $LiBF_4$ is not reproduced in the theory. The PC structure is illustrated in the lower panel.

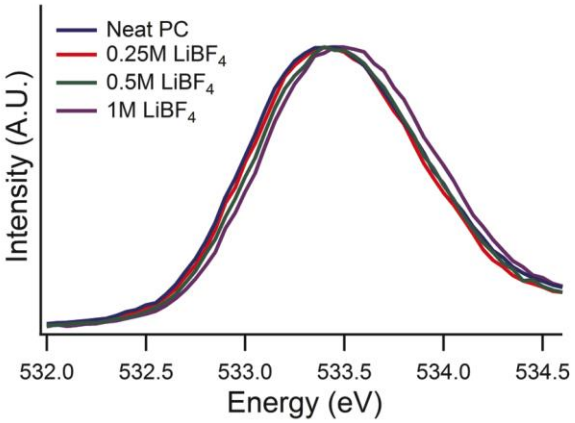

Figure 3: High-resolution experimental XA spectra of the carbonyl π* feature of PC and (PC)$LiBF_4$ electrolyte solutions. The blue shift observed for the π* feature increases as a function of concentration: 0.25M, 0.02 eV; 0.5M, 0.04 eV; 1.0M, 0.09 eV relative to neat PC.

b. MD Simulations

The large-box MD simulations produced values for diffusivity, conductivity, and degree of uncorrelated ionic motion (ionicity) in excellent agreement with previously reported experimental values;[25] these values are tabulated in Table 1. A comparison of the structural parameters of the small and large boxes is presented in Figure 4. The small box does exhibit a small increase in ion aggregation (Li..F association number of 1.95 for the large box, 2.1 for the small box), likely facilitated by the enforced proximity of ions in the small box. The increase in $Li^+..BF_4^-$ association is balanced by a corresponding decrease in the number of Li^+-solvent interactions in the first solvation shell (2.3 large box, 2.15 small box), resulting in a constant value for the total lithium coordination number (~4.25). The Li^+..carbonyl interaction lengths and Li^+..O=C angular distributions are very similar for the small and large boxes (average Li^+..O=C angle 149.2° large box, 148.4° small box). This suggests that the interactions between the lithium ion and solvent molecules are not substantially altered by the small system size in the small simulation box.

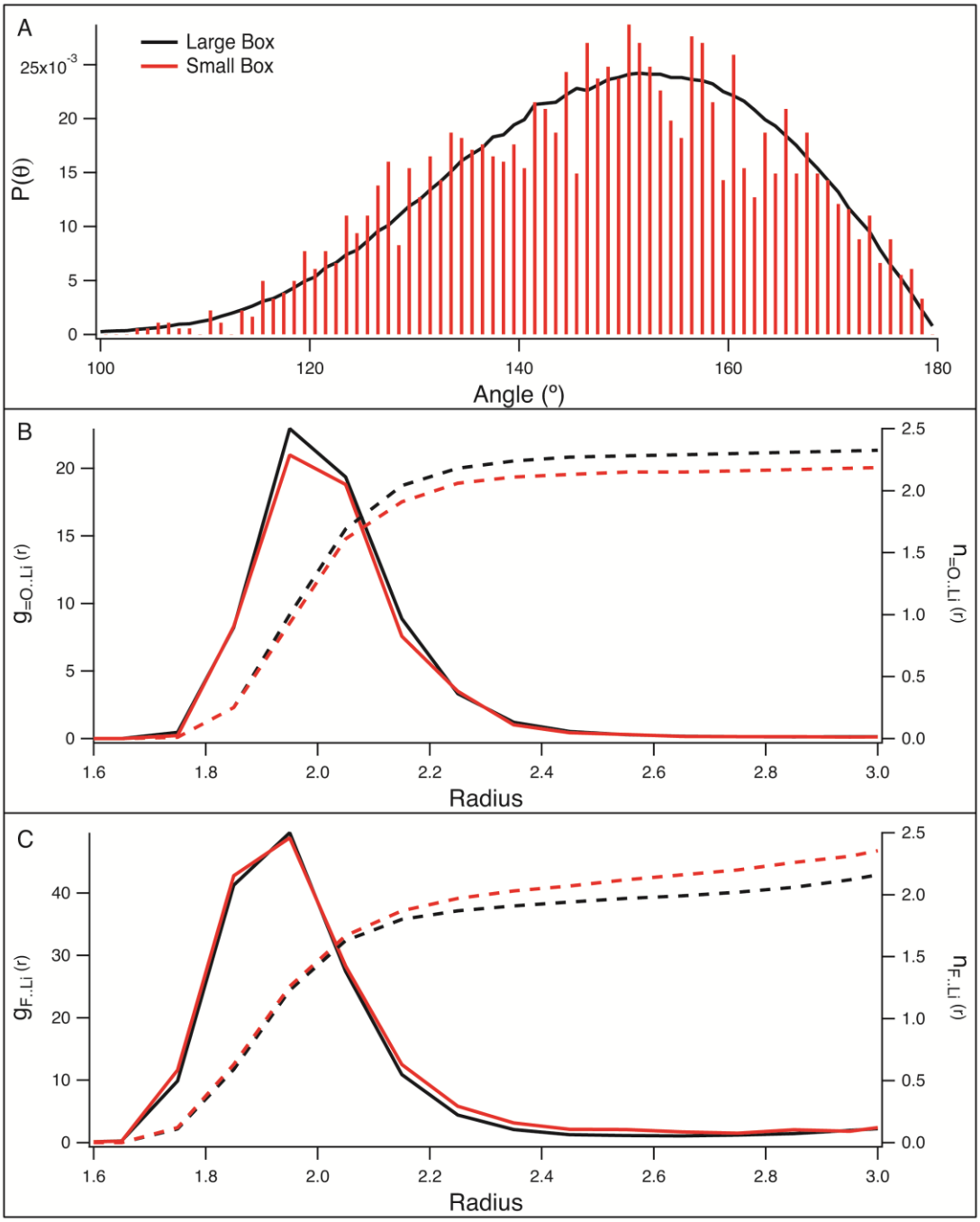

Figure 4: Comparison of structural parameters from large (640 PC, 64 $LiBF_4$) and small (20 PC, 2$LiBF_4$) MD simulation boxes: (A) Angular distribution of Li^+..O=C solvent interactions; (B) Radial distribution functions {RDFs, g(r)} and integrated radial distribution functions {iRDFs, n(r), shown as dashed lines} for interactions of Li^+ with PC carbonyl oxygen; and (C) RDFs and iRDFs for interaction of lithium with fluorine from the BF_4^- counterion. There is a small increase in Li..F interaction and decrease in Li..O= interaction in the small box relative to the large box, but the total coordination number (4.25) and solvent interaction angles are consistent.

c. Spectral Simulations

Due to the high computational cost of performing first-principles electronic structure calculations on large systems, the XCH calculation was performed using molecular configurations sampled from the small simulation boxes containing 20 PC for the neat liquid and 20 PC with 2 $LiBF_4$ for the electrolyte. The calculated spectrum of neat PC, shown in the bottom panel of Figure 2, reproduces the experimental spectrum well. The calculated spectrum of the (PC)$LiBF_4$ electrolyte solution does not exhibit the characteristic blue shift relative to the neat liquid observed in the experimental spectrum. Observed transitions in the XA spectrum were assigned with the assistance of isosurfaces generated for the states comprising each of the four major spectral features in neat PC. These isosurfaces, presented in Figure 5, suggest that the sharp features near 533.5 and 536.5 eV represent transitions to the π-antibonding system from the carbonyl and ring oxygen atoms, respectively. The broader, higher-energy states represent 1s-σ* transitions. As observed in the isosurfaces, the σ* states are highly disperse, with substantial density on neighboring molecules; as such, configurational broadening arising from inhomogeneity of the liquid environment is the primary source of spectral broadening for these features. The π* system is more localized, minimizing inhomogeneous broadening, explaining the narrower spectral width of features associated with transitions into this state. Other significant sources of broadening for these features include core-hole lifetime broadening and vibrational broadening.[49] In the condensed phase, vibrational structure is broadened, resulting in asymmetric features weighted towards the blue;[50] such structure is observed in the π* features of the experimental spectra. Each σ* feature contains spectral intensity for transitions originating from both carbonyl and ring oxygen atoms. While the calculated spectrum does not reproduce the experimental blue shift from PC to (PC)$LiBF_4$, the features in the experimental spectrum exhibiting the shift originate at least in part from the carbonyl oxygen. The largest shift is observed in the carbonyl π* feature. Less dramatic shifts are observed for the σ* features, resulting from shifting only of the spectral lines associated with transitions originating from the carbonyl oxygen. The ring 1s to π* transition exhibits very little shift in the experimental spectrum. These observations support the Raman findings of Kondo *et al*, which suggest that Li^+-PC interactions at concentrations below 2M occur nearly exclusively at the carbonyl oxygen of PC.[27]

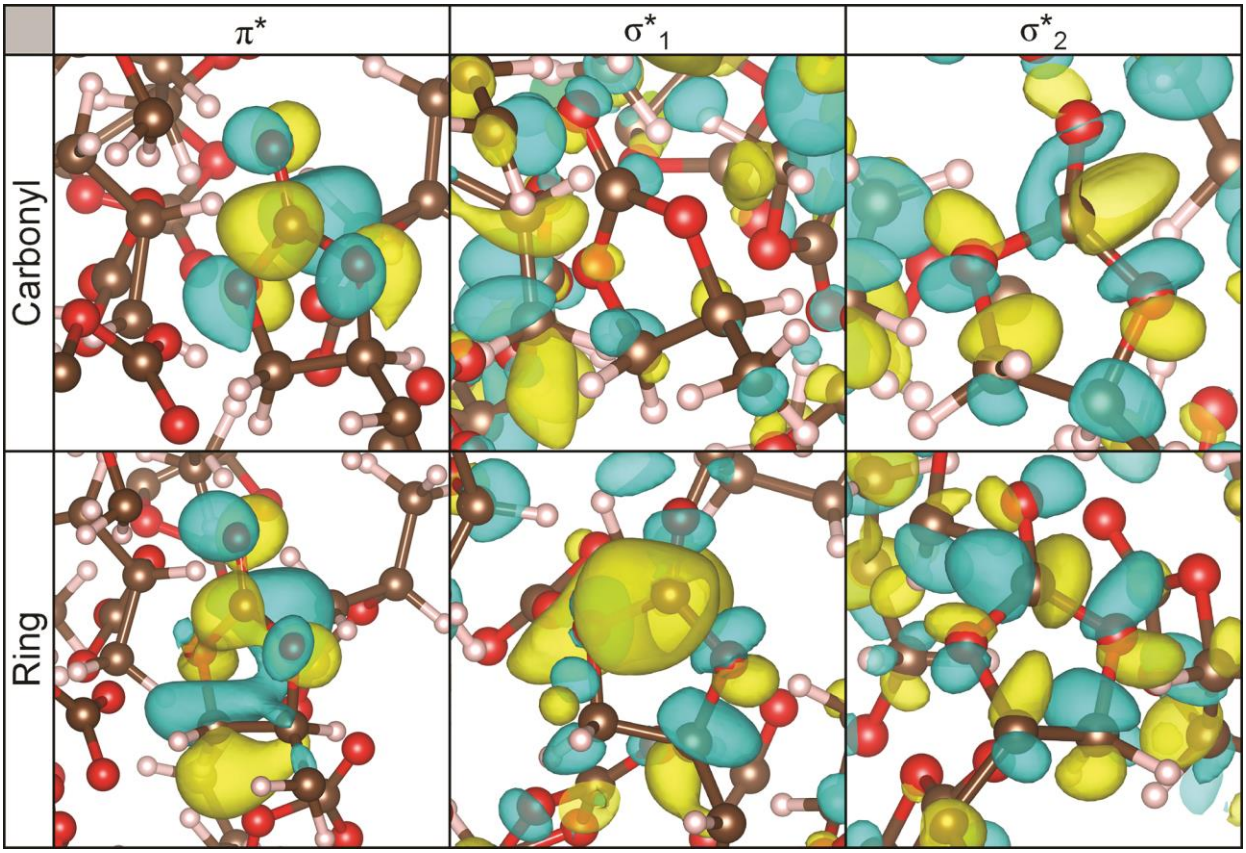

Figure 5: Isosurfaces of excited states for transitions from the carbonyl and ring oxygen atoms of PC. All isosurfaces were calculated for the same molecule from the small simulation box of neat PC. Surfaces correspond to spectral features as labeled in Figure 2. The π* transitions originating from the carbonyl and ring oxygen atoms correspond to the separate, well-resolved transitions labeled as $\pi^*_{carbonyl}$ and π^*_{ring}, while transitions from both the carbonyl and ring oxygen contribute to the spectral features denoted σ^*_1 and σ^*_2. The σ* states are highly delocalized throughout the neighboring PC molecules, resulting in substantial inhomogeneous configurational broadening of spectral features associated with transitions into these states. This phenomenon is not observed for the π* transitions, which are observed to have far more localized excited states. Isosurfaces were generated using Quantum-ESPRESSO and visualized in VESTA.[51]

d. Evaluation of the Li^+-PC Coordination Number

We divided the PC molecules in the molecular coordinates utilized to generate the calculated spectrum of PC($LiBF_4$) into two groups: those associating directly with the Li^+ ion (i.e. in the first solvation shell, Li..O=C separation <2.5 Å), and those not directly associating with Li^+ (free PC). Within the molecular coordinates sampled, no interactions were observed between Li^+ and PC except via the carbonyl oxygen; i.e. no ring oxygen or carbon atoms were located within the 2.5 Å interaction range. The spectra calculated from excitations from the carbonyl and ring oxygen in the associating and non-associating molecule groups were averaged to produce independent spectra for PC associating with Li^+ and free PC. These spectra are displayed in Figure 6. As predicted, there is no substantive difference in the spectrum of ring oxygen between associating and non-associating molecules. However, the carbonyl oxygen

spectrum of Li^+-associating PC molecules does exhibit a blue shift relative to that of free PC; for the carbonyl π^* feature centered at 533.5 eV, the peak is shifted by 0.35 eV, substantially greater than the experimental shift of 0.07 eV between the neat liquid and 1M electrolyte solution. Thus, the inability of the initial theoretical calculations to reproduce the experimentally observed blue-shift most likely results from an underestimation of the association number of Li^+-PC in the MD simulations. In order to estimate the correct association number, we have generated linear combinations of the computed carbonyl oxygen XAS spectra of associating and non-associating carbonyl oxygen for ratios of 20-50% associating molecules. The carbonyl π^* region of these linearly combined spectra are presented in Figure 7, along with a line indicating the location of the center of the carbonyl 1s-π^* transition feature in the experimental spectrum of 1M $LiBF_4$ in PC. The experimental shift is best reproduced by the combination containing 40% (±2%) Li^+-associating molecules. A comparison of the linear combination for this proportion of Li^+-associating PC to the experimental spectrum is shown in Figure 8 and exhibits excellent agreement. Using a density of 1M (PC)$LiBF_4$ of 1.251 kg/dm^3,[25] this association proportion corresponds to an average Li^+-PC association number of 4.5 (±0.2). While incongruous with the standard tetrahedral model of Li^+ solvation in electrolyte systems,[8,25,28,29] this value is in excellent agreement with that measured in neutron diffraction experiments[32] as well as IR studies of Li^+-EC.[16]

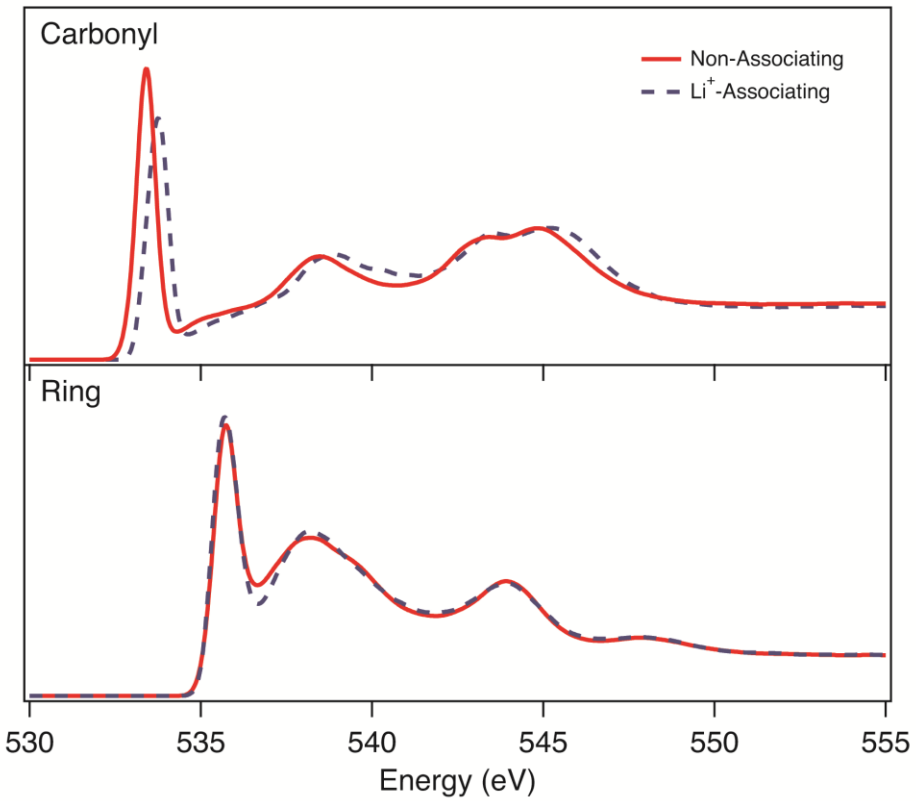

Figure 6: Calculated XA spectra for transitions from carbonyl and ring oxygen in Li^+-associating and non-associating PC molecules. 'Li^+-associating' PC has been defined for the purposes of this distinction as having a Li^+ ion within 2.5 Å of the carbonyl oxygen; however, there are almost no Li^+..O=C interactions longer than 2.25 Å and under 3 Å, as is apparent in the Li..O=C RDF in Figure 4. There is a distinct blue shift in the calculated XA spectrum of carbonyl oxygen interacting with lithium, while the spectrum of ring oxygen is insensitive to the presence of Li^+. The calculated spectrum of non-interacting carbonyl oxygen closely matches the carbonyl oxygen spectrum of neat PC.

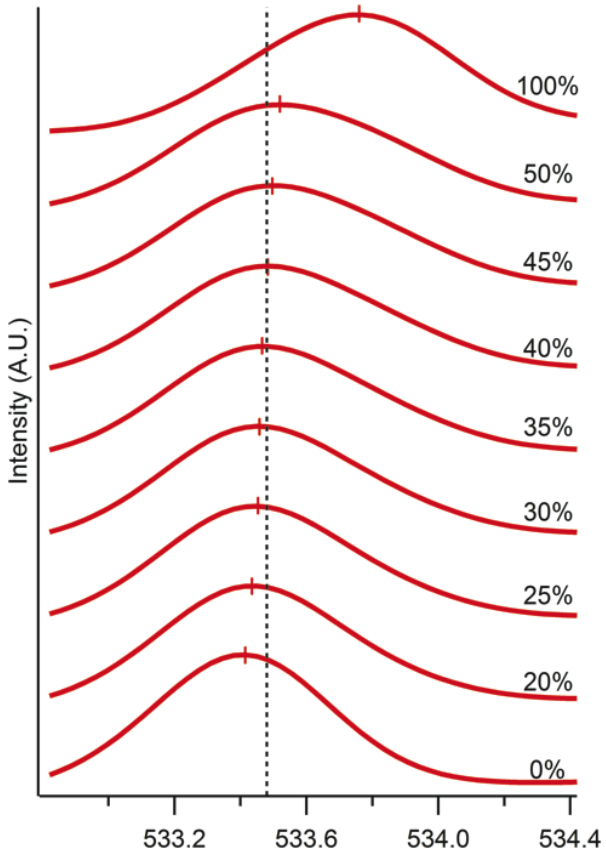

Figure 7: Linear combinations of the calculated XA spectra of Li^+-associating and non-associating (free) PC molecules in (PC)$LiBF_4$ around the carbonyl π* transition. Spectra are labeled with the weighting of Li^+-associating molecules in the linear combination producing each spectrum (thus, the curve labeled 0% is the spectrum of free PC, and 100% the spectrum of Li^+-associating PC). The center of each peak is marked with a vertical hash. The black dashed vertical line marks the experimental location of the carbonyl π* transition in 1M $LiBF_4$. The experimental peak is best reproduced by the linear combination comprising 40% Li^+-associating PC and 60% free PC.

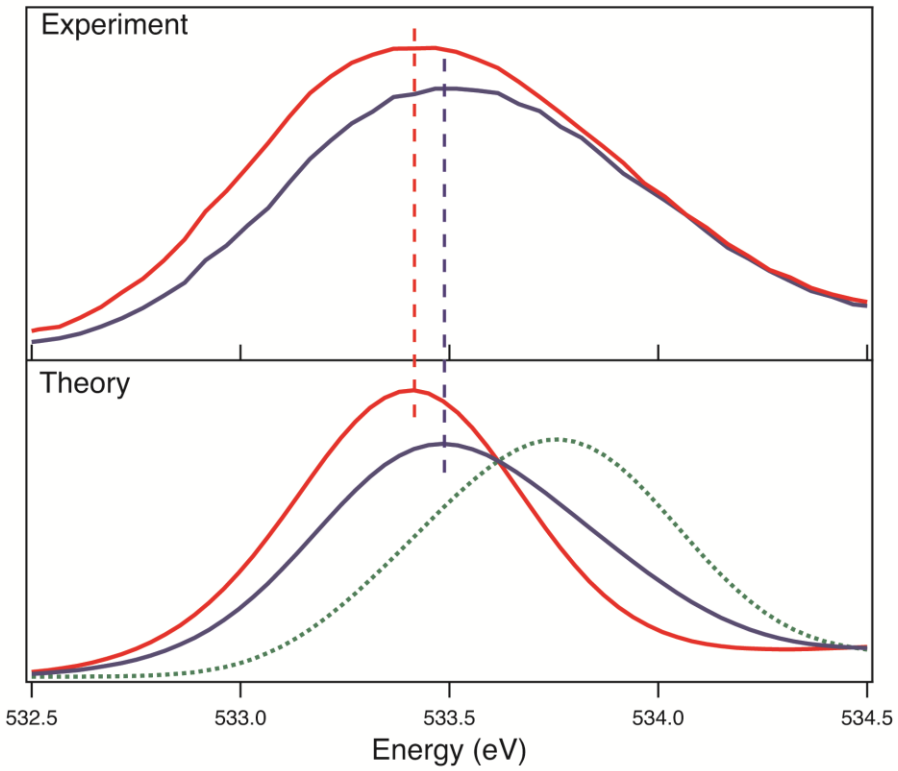

Figure 8: Comparison of the calculated spectrum containing 40% Li^+-associating PC and 60% free PC with the experimental spectrum of 1M $LiBF_4$ in PC around the carbonyl π* feature (in blue). The experimental spectrum of neat PC and calculated spectrum of non-associating PC molecules are shown in red for comparison. The dashed green line indicates the spectrum of the Li^+-associating PC molecules. This linear combination accurately reproduces the blue shift observed in the carbonyl π* feature of the experimental XA spectrum of the (PC)$LiBF_4$ electrolyte relative to the neat liquid.

e. XAS of EC:DMC and (EC:DMC)$LiBF_4$

The oxygen K-edge XA spectra of 50:50 (mole ratio) EC:DMC and 1M $LiBF_4$ in the same solvent mixture are shown in Figure 9. As with PC, the lowest-energy spectral feature, corresponding to the carbonyl 1s → π* transition, exhibits a small blue shift upon addition of the lithium salt. Furthermore, an additional spectral feature is observed at higher energy than the salient features of the PC spectrum, at ~549 eV. A single molecular dynamics snapshot from a suitably relaxed simulation box containing 10 molecules each of EC and DMC has also been utilized as the input for an XCH calculation of the spectrum of the pure solvent mixture. While the sample size is small, the combined spectrum accurately reproduces the major spectral features of the experimental spectrum. The 549 eV feature is found to arise from DMC, the spectrum of which is also observed to lack the σ* feature at ~545 eV. The calculated energies of the π* features of EC and DMC are found to match one another exactly, which is consistent with experimental spectral widths for these features commensurate with those found for PC.

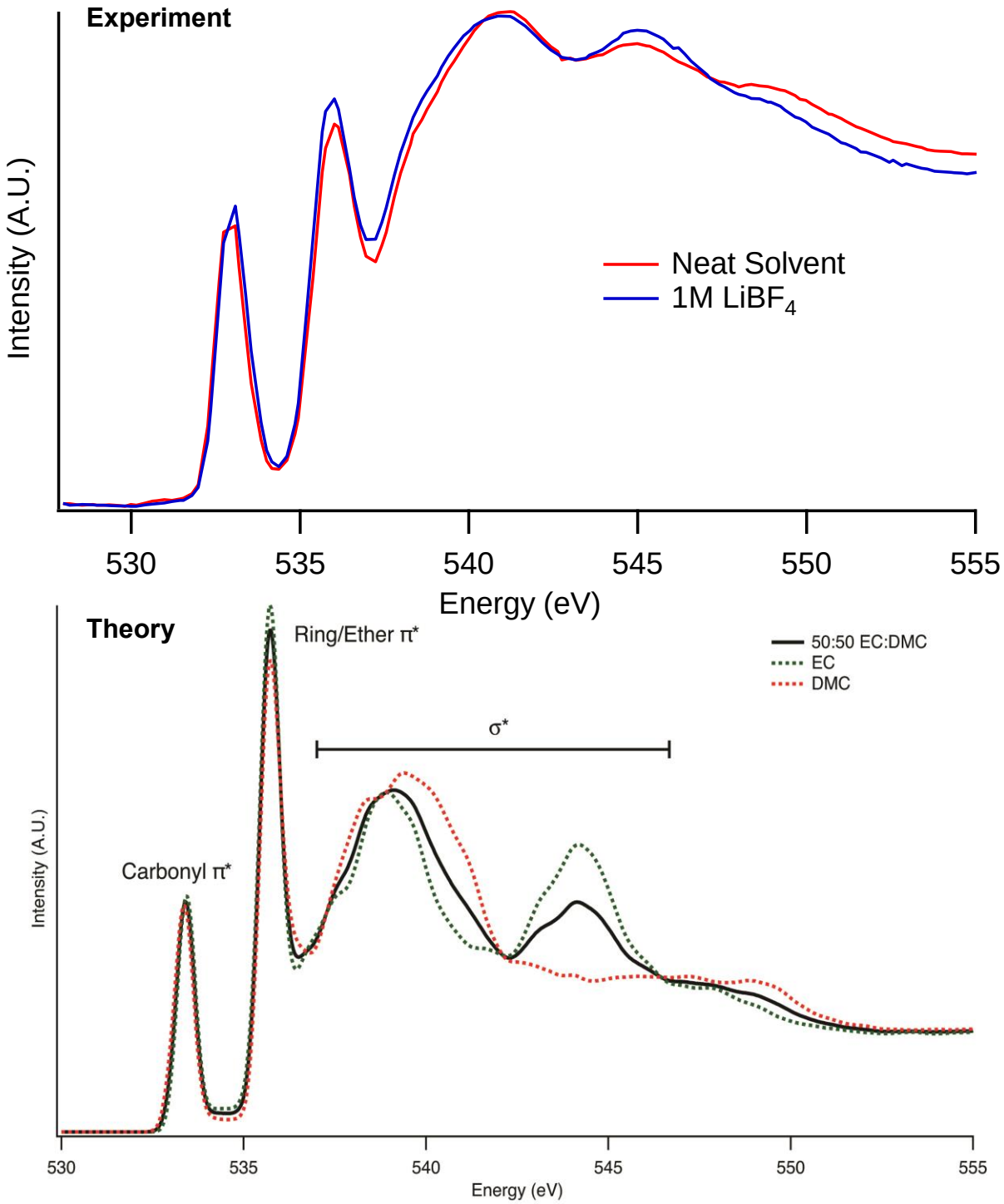

Figure 9: Experimental and calculated oxygen K-edge XA spectra of a 50:50 mixture of EC:DMC and experimental spectrum of 1M $LiBF_4$ in the same mixture. Major spectral features are labeled on the calculated spectrum. As in the experimental spectra of neat PC and 1M $LiBF_4$ in PC, a small blue shift is observed in the carbonyl π* feature upon addition of the lithium salt. The second σ* feature does not occur in the calculated spectrum of DMC, while a new, lower-intensity feature appears at ~549 eV.

High-resolution detail scans of the carbonyl π* feature of 50:50 EC:DMC and 1M $LiBF_4$ in the same mixture are shown in Figure 10. The lithium salt is observed to produce a 0.08 eV blue shift in the peak center of this spectral feature. This shift is commensurate with the shift observed in 1M PC solutions. As only rough XCH calculations have been performed on the neat solvent and no spectral simulations have been performed on the salt solution, analysis of the solvation number has not been performed for this system. However, solvation numbers in similar electrolyte solutions have been computed from Raman spectra utilizing a similar methodology fitting to computed peaks of Li^+-associating and non-associating solvent molecules.[52] The same analysis was not possible via Raman spectroscopy for PC-based electrolytes due to added spectral complexity arising from the different isomers and conformers of PC.

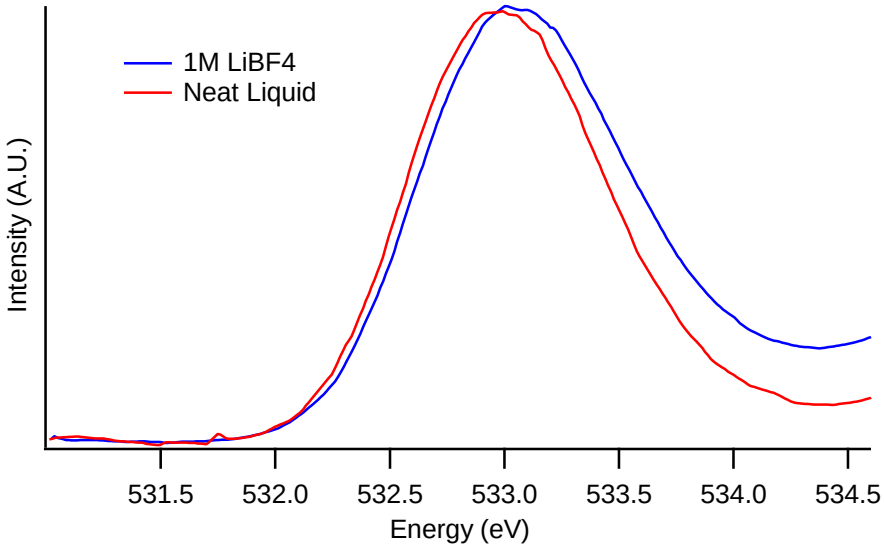

Figure 10: High-resolution detail scans of the carbonyl π* feature in the oxygen K-edge NEXAFS spectra of neat 50:50 EC:DMC and 1M $LiBF_4$ in 50:50 EC:DMC indicating a blue shift of 0.08 eV upon addition of the lithium salt.

V. Conclusions

The oxygen K-edge XA spectrum of PC and 50:50 EC:DMC exhibit a small blue shift upon addition of $LiBF_4$ which increases as a function of concentration. Shifts are only observed in spectral features associated with transitions from the carbonyl oxygens; transitions from the ring oxygens are unaffected by the addition of salt. XCH calculations have shown that the spectrum of free PC in the electrolyte solution is unchanged from that of the neat liquid, while the spectra of PC molecules coordinating Li^+ exhibit a blue shift. The experimental electrolyte spectrum can be accurately modeled as a linear combination of the spectra of Li^+-associating and free PC molecules. A linear combination of 40% lithium-associating and 60% free PC best reproduces the experimental spectrum of 1M $LiBF_4$. From this ratio we have calculated a Li^+..O=C association number of 4.5±0.2. The solvation number of Li^+ in EC:DMC was not calculated. MD simulations developed to provide molecular coordinates for the XCH calculation produced bulk solution properties in good agreement with experimental values. However, on the molecular scale they underestimate the solvation number of Li^+-PC relative to the experimental value determined in this study. New theoretical investigations of LIB electrolyte solutions

allowing for a substantial number of non-tetrahedral Li^+ solvation structures will produce a more accurate model of the real solutions and may provide a route to improvements to current battery technology.

VII. References

(1) Narain, V. *Global Industrial Batteries Market*; 2013.

(2) Goodenough, J. B.; Park, K.-S. The Li-Ion Rechargeable Battery: A Perspective. *J. Am. Chem. Soc.* **2013**, *135* (4), 1167–1176.

(3) Goodenough, J. B.; Kim, Y. Challenges for Rechargeable Li Batteries. *Chem. Mater.* **2010**, *22* (3), 587–603.

(4) Armand, M.; Tarascon, J.-M. Building Better Batteries. *Nature* **2008**, *451* (7179), 652–657.

(5) Aurbach, D. Review of Selected Electrode–solution Interactions Which Determine the Performance of Li and Li Ion Batteries. *J. Power Sources* **2000**, *89* (2), 206–218.

(6) Peled, E. Advanced Model for Solid Electrolyte Interphase Electrodes in Liquid and Polymer Electrolytes. *J. Electrochem. Soc.* **1997**, *144* (8), L208.

(7) Ganesh, P.; Kent, P. R. C.; Jiang, D. Solid–Electrolyte Interphase Formation and Electrolyte Reduction at Li-Ion Battery Graphite Anodes: Insights from First-Principles Molecular Dynamics. *J. Phys. Chem. C* **2012**, *116* (46), 24476–24481.

(8) Leung, K.; Budzien, J. L. Ab Initio Molecular Dynamics Simulations of the Initial Stages of Solid-Electrolyte Interphase Formation on Lithium Ion Battery Graphitic Anodes. *Phys. Chem. Chem. Phys.* **2010**, *12* (25), 6583–6586.

(9) Xing, L.; Li, W.; Wang, C.; Gu, F.; Xu, M.; Tan, C.; Yi, J. Theoretical Investigations on Oxidative Stability of Solvents and Oxidative Decomposition Mechanism of Ethylene Carbonate for Lithium Ion Battery Use. *J. Phys. Chem. B* **2009**, *113* (52), 16596–16602.

(10) Goodenough, J. B. Evolution of Strategies for Modern Rechargeable Batteries. *Acc. Chem. Res.* **2013**, *46* (5), 1053–1061.

(11) Hung, I.; Zhou, L.; Pourpoint, F.; Grey, C. P.; Gan, Z. Isotropic High Field NMR Spectra of Li-Ion Battery Materials with Anisotropy >1 MHz. *J. Am. Chem. Soc.* **2012**, *134* (4), 1898–1901.

(12) Harris, S. J.; Timmons, A.; Baker, D. R.; Monroe, C. Direct in Situ Measurements of Li Transport in Li-Ion Battery Negative Electrodes. *Chem. Phys. Lett.* **2010**, *485* (4–6), 265–274.

(13) Borodin, O.; Zhuang, G. V.; Ross, P. N.; Xu, K. Molecular Dynamics Simulations and Experimental Study of Lithium Ion Transport in Dilithium Ethylene Dicarbonate. *J. Phys. Chem. C* **2013**, *117* (15), 7433–7444.

(14) Borodin, O.; Bedrov, D. Interfacial Structure and Dynamics of the Lithium Alkyl Dicarbonate SEI Components in Contact with the Lithium Battery Electrolyte. *J. Phys. Chem. C* **2014**, *118* (32), 140723165951001.

(15) Xu, K. Nonaqueous Liquid Electrolytes for Lithium-Based Rechargeable Batteries. *Chem. Rev.* **2004**, *104* (10), 4303–4417.

(16) Nie, M.; Abraham, D. P.; Seo, D. M.; Chen, Y.; Bose, A.; Lucht, B. L. Role of Solution Structure in Solid Electrolyte Interphase Formation on Graphite with $LiPF_6$ in Propylene Carbonate. *J. Phys. Chem. C* **2013**, *117* (48), 25381–25389.

(17) von Cresce, A.; Xu, K. Preferential Solvation of Li^+ Directs Formation of Interphase on Graphitic Anode. *Electrochem. Solid-State Lett.* **2011**, *14* (10), A154.

(18) Xu, K.; Lam, Y.; Zhang, S. S.; Jow, T. R.; Curtis, T. B. Solvation Sheath of Li^+ in Nonaqueous Electrolytes and Its Implication of Graphite/Electrolyte Interface Chemistry. *J. Phys. Chem. C* **2007**, *111* (20), 7411–7421.

(19) Harris, S. J.; Lu, P. Effects of Inhomogeneities - Nanoscale to Mesoscale - on the Durability of Li-Ion Batteries. *J. Phys. Chem. C* **2013**, *117*, 6481–6492.

(20) Xu, K.; von Cresce, A.; Lee, U. Differentiating Contributions to "Ion Transfer" Barrier from Interphasial Resistance and Li+ Desolvation at Electrolyte/Graphite Interface. *Langmuir* **2010**, *26* (13), 11538–11543.

(21) Xu, K.; von Wald Cresce, A. Li^+-Solvation/desolvation Dictates Interphasial Processes on Graphitic Anode in Li Ion Cells. *J. Mater. Res.* **2012**, *27* (18), 2327–2341.

(22) Ding, M. S. Conductivity and Viscosity of PC-DEC and PC-EC Solutions of $LiBF_4$. *J. Electrochem. Soc.* **2004**, *151* (1), A40.

(23) Yang, L.; Xiao, A.; Lucht, B. L. Investigation of Solvation in Lithium Ion Battery Electrolytes by NMR Spectroscopy. *J. Mol. Liq.* **2010**, *154* (2–3), 131–133.

(24) Reddy, V. P.; Smart, M. C.; Chin, K. B.; Ratnakumar, B. V.; Surampudi, S.; Hu, J.; Yan, P.; Surya Prakash, G. K. ^{13}C NMR Spectroscopic, CV, and Conductivity Studies of Propylene Carbonate-Based Electrolytes Containing Various Lithium Salts. *Electrochem. Solid-State Lett.* **2005**, *8* (6), A294.

(25) Takeuchi, M.; Kameda, Y.; Umebayashi, Y.; Ogawa, S.; Sonoda, T.; Ishiguro, S.; Fujita, M.; Sano, M. Ion–ion Interactions of $LiPF_6$ and $LiBF_4$ in Propylene Carbonate Solutions. *J. Mol. Liq.* **2009**, *148* (2–3), 99–108.

(26) Burba, C. M.; Frech, R. Spectroscopic Measurements of Ionic Association in Solutions of LiPF6. *J. Phys. Chem. B* **2005**, *109* (31), 15161–15164.

(27) Kondo, K.; Sano, M.; Hiwara, A. Conductivity and Solvation of Li^+ Ions of $LiPF_6$ in Propylene Carbonate Solutions. *J. Phys. Chem. B* **2000**, *104*, 5040–5044.

(28) Morita, M.; Asai, Y.; Yoshimoto, N.; Ishikawa, M. A Raman Spectroscopic Study of Organic Electrolyte Solutions Based on Binary Solvent Systems of Ethylene Carbonate with Low Viscosity Solvents Which Dissolve Different Lithium Salts. *J. Chem. Soc., Faraday Trans.* **1998**, *94*, 3451–3456.

(29) Ganesh, P.; Jiang, D.; Kent, P. R. C. Accurate Static and Dynamic Properties of Liquid Electrolytes for Li-Ion Batteries from Ab Initio Molecular Dynamics. *J. Phys. Chem. B* **2011**, *115* (12), 3085–3090.

(30) Hyodo, S.-A.; Okabayashi, K. Raman Intensity Study of Local Structure in Non-Aqueous Electrolyte solutions—I. Cation-Solvent Interaction in $LiClO_4$/ethylene Carbonate. *Electrochim. Acta* **1989**, *34* (11), 1551–1556.

(31) Allen, J. L.; Borodin, O.; Seo, D. M.; Henderson, W. a. Combined Quantum chemical/Raman Spectroscopic Analyses of Li^+ Cation Solvation: Cyclic Carbonate solvents—Ethylene Carbonate and Propylene Carbonate. *J. Power Sources* **2014**, *267*, 821–830.

(32) Kameda, Y.; Umebayashi, Y.; Takeuchi, M.; Wahab, M. A.; Fukuda, S.; Ishiguro, S.; Sasaki, M.; Amo, Y.; Usuki, T. Solvation Structure of Li^+ in Concentrated LiPF6-Propylene Carbonate Solutions. *J. Phys. Chem. B* **2007**, *111* (22), 6104–6109.

(33) Bogle, X.; Vazquez, R.; Greenbaum, S.; Cresce, A. von W.; Xu, K. Understanding Li^+–Solvent Interaction in Nonaqueous Carbonate Electrolytes with 17 O NMR. *J. Phys. Chem. Lett.* **2013**, *4* (10), 1664–1668.

(34) Castriota, M.; Cazzanelli, E.; Nicotera, I.; Coppola, L.; Oliviero, C.; Ranieri, G. A. Temperature Dependence of Lithium Ion Solvation in Ethylene carbonate–$LiClO_4$ Solutions. *J. Chem. Phys.* **2003**, *118* (12), 5537.

(35) Wilson, K. R.; Rude, B. S.; Smith, J.; Cappa, C.; Co, D. T.; Schaller, R. D.; Larsson, M.; Catalano, T.; Saykally, R. J. Investigation of Volatile Liquid Surfaces by Synchrotron X-Ray Spectroscopy of Liquid Microjets. *Rev. Sci. Instrum.* **2004**, *75* (3), 725–736.

(36) Prendergast, D.; Galli, G. X-Ray Absorption Spectra of Water from First Principles Calculations. *Phys. Rev. Lett.* **2006**, *96* (21), 215502.

(37) Duffin, A. M.; England, A. H.; Schwartz, C. P.; Uejio, J. S.; Dallinger, G. C.; Shih, O.; Prendergast, D.; Saykally, R. J. Electronic Structure of Aqueous Borohydride: A Potential Hydrogen Storage Medium. *Phys. Chem. Chem. Phys.* **2011**, *13* (38), 17077–17083.

(38) Duffin, A. M.; Schwartz, C. P.; England, A. H.; Uejio, J. S.; Prendergast, D.; Saykally, R. J. pH-Dependent X-Ray Absorption Spectra of Aqueous Boron Oxides. *J. Chem. Phys.* **2011**, *134* (15), 154503.

(39) England, A. H.; Duffin, A. M.; Schwartz, C. P.; Uejio, J. S.; Prendergast, D.; Saykally, R. J. On the Hydration and Hydrolysis of Carbon Dioxide. *Chem. Phys. Lett.* **2011**, *514* (4–6), 187–195.

(40) Shih, O.; England, A. H.; Dallinger, G. C.; Smith, J. W.; Duffey, K. C.; Cohen, R. C.; Prendergast, D.; Saykally, R. J. Cation-Cation Contact Pairing in Water: Guanidinium. *J. Chem. Phys.* **2013**, *139* (3), 35104.

(41) Wilson, K. R.; Rude, B. S.; Catalano, T.; Schaller, R. D.; Tobin, J. G.; Co, D. T.; Saykally, R. J. X-Ray Spectroscopy of Liquid Water Microjets. *J. Phys. Chem. B* **2001**, *105* (17), 3346–3349.

(42) Cappa, C. D.; Smith, J. D.; Wilson, K. R.; Saykally, R. J. Revisiting the Total Ion Yield X-Ray Absorption Spectra of Liquid Water Microjets. *J. Phys. Condens. Matter* **2008**, *20* (20), 205105.

(43) Borodin, O. Polarizable Force Field Development and Molecular Dynamics Simulations of Ionic Liquids. *J. Phys. Chem. B* **2009**, *113* (33), 11463–11478.

(44) von Wald Cresce, A.; Borodin, O.; Xu, K. Correlating Li^+ Solvation Sheath Structure with Interphasial Chemistry on Graphite. *J. Phys. Chem. C* **2012**, *116* (50), 26111–26117.

(45) Borodin, O.; Smith, G. D. Quantum Chemistry and Molecular Dynamics Simulation Study of Dimethyl Carbonate: Ethylene Carbonate Electrolytes Doped with $LiPF_6$. *J. Phys. Chem. B* **2009**, *113* (6), 1763–1776.

(46) Seo, D. M.; Borodin, O.; Han, S.-D.; Boyle, P. D.; Henderson, W. A. Electrolyte Solvation and Ionic Association II. Acetonitrile-Lithium Salt Mixtures: Highly Dissociated Salts. *J. Electrochem. Soc.* **2012**, *159* (9), A1489–A1500.

(47) Giannozzi, P.; Baroni, S.; Bonini, N.; Calandra, M.; Car, R.; Cavazzoni, C.; Ceresoli, D.; Chiarotti, G. L.; Cococcioni, M.; Dabo, I.; et al. QUANTUM ESPRESSO: A Modular and Open-Source Software Project for Quantum Simulations of Materials. *J. Phys. Condens. Matter* **2009**, *21* (39), 395502.

(48) Perdew, J. P.; Burke, K.; Ernzerhof, M. Generalized Gradient Approximation Made Simple. *Phys. Rev. Lett.* **1996**, *77* (18), 3865–3868.

(49) Stöhr, J. *NEXAFS Spectroscopy*; 1992; Vol. 25.

(50) Schwartz, C. P.; Uejio, J. S.; Saykally, R. J.; Prendergast, D. On the Importance of Nuclear Quantum Motions in near Edge X-Ray Absorption Fine Structure Spectroscopy of Molecules. *J. Chem. Phys.* **2009**, *130* (18), 184109.

(51) Momma, K.; Izumi, F. VESTA : A Three-Dimensional Visualization System for Electronic and Structural Analysis. *J. Appl. Crystallogr.* **2008**, *41* (3), 653–658.

(52) Allen, J. L.; Borodin, O.; Seo, D. M.; Henderson, W. A. Combined Quantum chemical/Raman Spectroscopic Analyses of Li^+ Cation Solvation: Cyclic Carbonate solvents—Ethylene Carbonate and Propylene Carbonate. *J. Power Sources* **2014**, *267*, 821–830.

Chapter 4: Properties of Aqueous Nitrate and Nitrite from X-ray Absorption Spectroscopy

Material in this chapter has been reproduced from

Smith, J. W.; Lam, R. K.; Shih, O.; Rizzuto, A. M.; Prendergast, D.; Saykally, R. J. "Properties of Aqueous Nitrate and Nitrite from X-Ray Absorption Spectroscopy." *J. Chem. Phys.* **2015**, *143* (8), 84503.

published by the American Institute of Physics, with permission of all co-authors.

I. Abstract

Nitrate and nitrite ions are of considerable interest, both for their widespread use in commercial and research contexts and because of their central role in the global nitrogen cycle. The chemistry of atmospheric aerosols, wherein nitrate is abundant, has been found to depend on the interfacial behavior of ionic species. The interfacial behavior of ions is determined largely by their hydration properties; consequently, the study of the hydration and interfacial behavior of nitrate and nitrite comprises a significant field of study. In this work we describe the study of aqueous solutions of sodium nitrate and nitrite via X-ray absorption spectroscopy (XAS), interpreted in light of first-principles density functional theory electronic structure calculations. Experimental and calculated spectra of the nitrogen K-edge XA spectra of bulk solutions exhibit a large 3.7 eV shift between the XA spectra of nitrate and nitrite resulting from greater stabilization of the nitrogen 1s energy level in nitrate. A similar shift is not observed in the oxygen K-edge XA spectra of NO_3^- and NO_2^-. The hydration properties of nitrate and nitrite are found to be similar, with both anions exhibiting a similar propensity towards ion pairing.

II. Introduction

Owing largely to their affordable pricing and excellent water solubility, salts of nitrate and nitrite have found numerous uses in both commercial and laboratory applications. For example, nitrate is an important component of agricultural fertilizers, promoting general and leaf growth, although overuse of such fertilizers has come under significant scrutiny in recent years for its environmental impacts.[1] In addition to their well-known applications in food preservation and similar antimicrobial roles, nitrite anions may prove useful in the complexation of actinides as part of the life cycle of nuclear fuels.[2] In addition, recent studies have indicated that nitrate and nitrite may have therapeutic medical applications in the treatment of numerous conditions, particularly acute cardiovascular events including myocardial infarction and stroke.[3]

Nitrate is of particular importance in environmental chemistry and modeling as a result of its high concentration in atmospheric aerosols.[4] It has become increasingly clear that the chemistry of such aerosols depends substantially on the interfacial behavior of constituent anions.[5,6] Consequently, the behavior of atmospherically abundant ions such as nitrate at the air-water interface have become the subject of substantial study in recent years.[7–11] The results of theoretical investigations of the interfacial behavior of NO_3^- have been inconsistent, with some models predicting interfacial enhancement and others interfacial depletion. Experimental results from ultraviolet second harmonic generation (UV-SHG) spectroscopy indicate a weak surface

enhancement,[12] while X-ray photoelectron spectroscopy (XPS)[11] indicates that nitrate is present at the air-water interface at a depleted concentration relative to the bulk. Much of this inconsistency can be attributed to a free energy of adsorption near 0.[12]

Several researchers have proposed that surface affinity is largely driven by the polarizability of the ion in question.[7,8,13] However, while polarizability often correlates with anion surface activity, recent studies have indicated that surface adsorption propensity is more generally controlled by the bulk hydration properties of the anion.[14–16] Both models predict a stronger surface affinity for nitrate than for nitrite. However, UV-SHG investigations of aqueous sodium nitrite have indicated a substantially stronger surface affinity than that observed for the nitrate salts.[17] This surprising result has been attributed to the adsorption of nitrite to the air-water interface as a contact ion pair with the sodium counterion.

In this work we present the study of aqueous solutions of sodium nitrate and sodium nitrite via X-ray absorption spectroscopy (XAS). XAS provides an atom-specific probe of unoccupied electronic states, and is sensitive to both the intra- and intermolecular environment of the target atom. Extraction of meaningful chemical information from XA spectra requires interpretation with the assistance of detailed electronic structure calculations. We have utilized the Prendergast-Galli eXcited electron and Core Hole (XCH) methodology, a first-principles density functional theory calculation, to compute theoretical XA spectra of aqueous $NaNO_3$ and $NaNO_2$ solutions. We have recently used this combination of experimental and theoretical methodology to study cation-cation pairing in aqueous solutions of guanidinium hydrochloride,[18] the hydrolysis of carbon dioxide in the carbon cycle,[19–21] and the solvation of Li^+ by propylene carbonate.[22(Chapter 2)] Here, we apply these techniques to the comparative study of ion solvation and pairing in aqueous solutions of $NaNO_3$ and $NaNO_2$.

III. Experimental and Theoretical Methods

a. X-ray Spectroscopy of Liquid Microjets

Nitrate and nitrite were used as obtained from Merck AgA, ACS grade, with 99% minimum purity. Solutions were prepared in 18.1 MΩ·cm water obtained from a Millipore system.

XA spectra of the nitrogen K-edge were collected at Beamline 8.0.1 of the Advanced Light Source at Lawrence Berkeley National Laboratory (Berkeley, CA), with nominal resolving power $E/\Delta E = 7000$. Liquid jets of solutions of nitrate and nitrite were generated by pumping the liquid through a 30-μm inner diameter silica capillary. The liquid jets interact with the focused X-ray beamline (spot size ~100 μm x 35 μm) in a vacuum chamber at ~10^{-4} torr. Total electron yield (TEY) XA spectra are collected on a 2.1 kV biased copper electrode with 0.2 eV step sizes and 1 second count time per step. Our previous work has demonstrated that TEY XA spectra are representative of the bulk liquid.[23,24] Spectra have been normalized to I_0 signal collected on a high-transmission gold grid intersecting the beamline upstream of the chamber. Spectra of the gas-phase background were measured by moving the jet ~1 mm out of the X-ray beamline and collecting the TEY spectrum; the resulting gas-phase spectra were subsequently subtracted from the corresponding liquid spectra. A single-point energy axis calibration was performed using gaseous nitrogen. A more complete description of the experiment can be found in a prior publication.[25]

b. Molecular Dynamics Simulations

Condensed phase molecular dynamics simulations were performed in Amber 14[26] under periodic boundary conditions. We constructed simulation cells for sodium nitrate and sodium nitrite solvated by TIP3P water molecules in two sizes: small boxes, containing ~90 water molecules; and larger boxes containing ~550 water molecules. Exact simulation box sizes and contents are listed in Table 1 for nitrate and Table 2 for nitrite. We employed a semi-empircal Quantum Mechanics/Molecular Mechanics (QM/MM) approach utilizing the PM3 methodology, while the classical region was simulated using the Amber default ff99SB force field parameters. The quantum mechanical region consisted of the nitrate/nitrite anion and intermolecular interactions of the anion with any cation or water molecule within a defined interaction cutoff distance; this same cutoff distance was utilized for treatment of intermolecular interactions within the classical region of the simulation cell comprising all components aside from the anion. Trajectories of the small boxes were simulated for 20 ns using a 4Å cutoff for intermolecular interactions, with coordinate snapshots stored every 200 fs. The larger boxes were simulated with 4, 7, and 10Å interaction cutoffs, with simulation times between 20 and 150 ns and again recording coordinates every 200 fs. More detailed simulation parameters may be found in Tables I and II. Radial distribution functions (RDFs) and integrated RDFs were calculated using the built-in analysis tools of the Visual Molecular Dynamics (VMD) program.[27]

c. Simulated Spectroscopy

Simulated spectra of the nitrogen and oxygen K-edges of nitrate and nitrite were calculated using the XCH approximation,[28] a first-principles constrained-occupancy density functional theory (DFT) electronic structure calculation. Molecular coordinates for the electronic structure calculations were sampled from the small box MD simulation, with snapshots for simulated spectroscopy separated by 160 ps. Fifty snapshots each corresponding to ion-paired ($r_{N\text{-}O\ldots Na} \leq 2.6$ Å) and unpaired ($r_{N\text{-}O\ldots Na} > 2.6$ Å) configurations were analyzed and averaged for each anion. DFT calculations were performed under periodic boundary conditions using the Plane Wave Self-Consistent Field (PWSCF) program within the Quantum-ESPRESSO package.[29] Exchange correlation potentials were calculated within the Perdew-Burke-Ernzerhof form of the Generalized Gradient Approximation (PBE-GGA).[30] The XCH calculation generates the electron density of the lowest energy core-excited state self-consistently, promoting an electron from a target atom and modeling the impact of the core hole on electronic structure via a suitably modified pseudopotential. Higher energy excited states are approximated from the unoccupied Kohn-Sham orbitals of the self-consistent field generated for the first core-excited state. Transition matrix elements between the 1s atomic orbital of the target atom and calculated unoccupied states are computed within Fermi's Golden Rule. Resulting transitions were broadened via Gaussian convolution using a fixed linewidth of 0.2 eV to generate the X-ray absorption spectrum of the target atom. The averaged spectra over the 50 snapshots of each anion/configuration were rigidly aligned to the experimental energy scale using a constant shift derived from alignment of a reference spectrum of gaseous N_2 using a previously-described methodology that provides relative spectral alignment by reference to an isolated atom.[19]

IV. Results and Discussion

XA spectra of the nitrogen K-edge of sodium nitrate and sodium nitrite solutions between 0.5 and 3M are shown in Figure 1. The spectra exhibit two strong features: a sharp feature corresponding to the 1s-π* transition, and a broader feature corresponding to the 1s-σ* transition centered ~9.5 eV higher in energy. The spectrum of each anion is found to be invariant with concentration in this range. However, a substantial blue shift of ~3.65 eV (measured at the center of the 1s-π* transition) separates the nitrate spectrum from the nitrite spectrum. This is consistent with similar shifts previously reported between the X-ray photoelectron spectra of aqueous nitrate and nitrite[11] and XA spectra of the solid potassium salts.[31] It is substantially larger than the 1.4 eV shift previously observed in the nitrogen K-edge spectra of aqueous glycine with neutral and protonated (oxidation state +1) nitrogen atoms.[32]

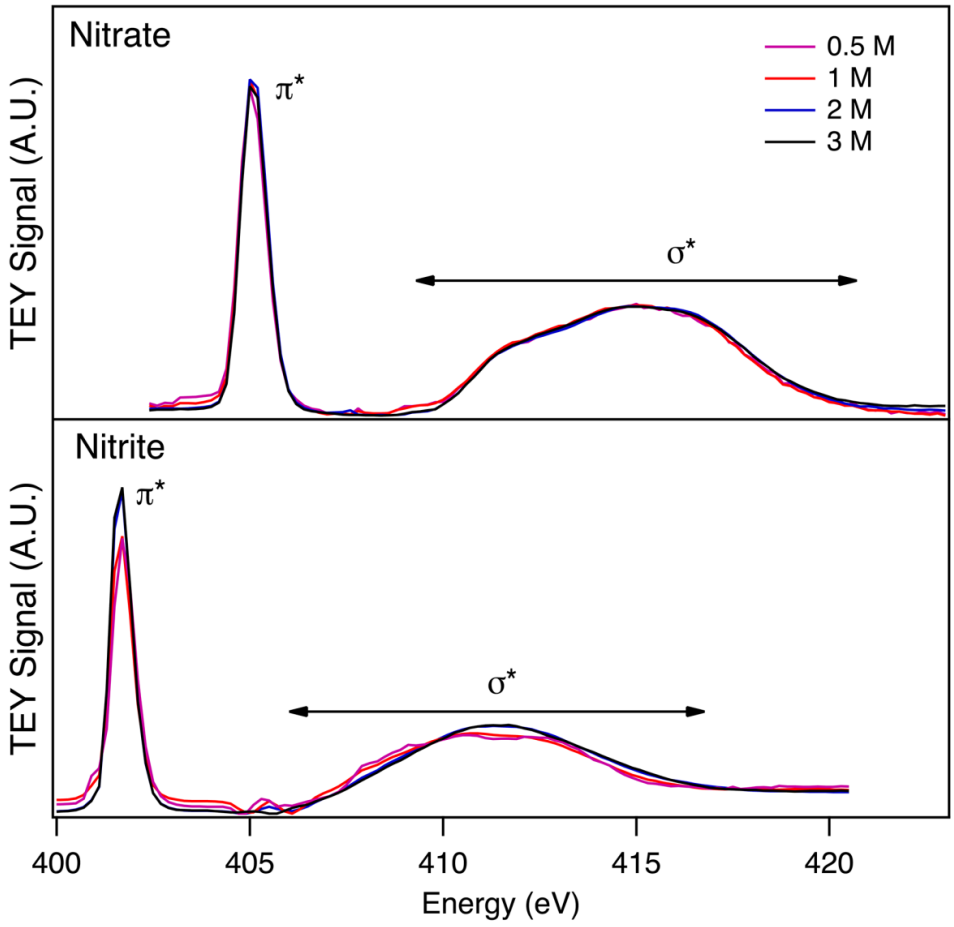

Figure 1: Nitrogen K-edge TEY XA spectra of solutions of $NaNO_3$ and $NaNO_2$ between 0.5 and 3 M. The spectra of each salt are qualitatively similar across the concentration range studied. Annotations indicate the spectral regions corresponding to 1s-σ* and 1s-π* transitions.

Table 1: Simulation parameters from MD simulations of sodium nitrate. [i] Percentage of snapshots representing an ion-paired configuration.

Interaction cutoff (Å)	4	4	7	10
# of water molecules	90	511		
Box dimensions (Å)	14.584	25.622		
	13.062	24.324		
	14.334	25.251		
Concentration (mol/L)	0.608	0.105		
Run time (ns)	20	82	81	150
Pairs (%)[i]	68.2	39.8	53.4	31.2

Table 2: Simulation parameters from MD simulations of sodium nitrite. [i] Percentage of snapshots representing an ion-paired configuration.

Interaction cutoff (Å)	4	4	7	10
# of water molecules	89	555		
Box dimensions (Å)	13.080	24.866		
	14.332	26.542		
	13.885	25.589		
Concentration (mol/L)	0.638	0.0983		
Run time (ns)	20	20	20	20
Pairs (%)[i]	63.8	27.9	42.8	59.8

The performed MD simulations do not suggest a statistically significant difference in the ion pairing rates of sodium nitrate and sodium nitrite salt solutions in the small box simulations used for electronic structure calculations (see Tables 1 and 2). Radial distribution functions (RDFs) and integrated RDFs describing the interactions of the anions (as measured from the position of the nitrogen atom) and Na^+ cations with the water solvent and one another are shown in Figures 2 (nitrate) and 3 (nitrite). Unsurprisingly, increasing the box size from ~90 water molecules to >500 waters substantially decreased the ion pairing probability for both nitrate (from 68% to 22%) and nitrite (from 63% to 28%). It is likely that the ions in the small box used for electronic structure calculations experienced enhanced ion pairing as a result of finite size effects. Also unsurprisingly, increasing the interaction length in the larger box generally increases the probability of ion pairing. There is a decrease in $NO_3^-\ldots Na^+$ ion pairing from the 7Å cutoff simulation to the 10Å cutoff simulation, which was reproducible over several simulation runs. The origin of this anomalous behavior is not clear. It is reasonable to assume that the results of the 10Å cutoff simulations are most accurate within the simulation parameters utilized. However, this is the only set of simulation parameters for which nitrite exhibits a greater propensity for ion pairing than nitrate, whereas experimentally determined activity coefficients for solutions of sodium nitrate[33] and nitrite[34] indicate a greater propensity towards ion pairing in nitrate solutions throughout the concentration range covered in this work. While this does indicate that the small box simulations used in the electronic structure calculations was reasonably representative of the relative rates of ion pairing indicated by the experimental data,

the anomalous ion pairing behavior observed in the 10Å cutoff simulations of the larger system – ostensibly the most accurate simulations performed – presents an interesting matter for future investigation. Correlation curves – calculated by correlation(dt) = $\langle f(t) \cdot f(t+dt) \rangle$ with f(t) = 1 for ion-paired configurations, f(t) = -1 for unpaired configurations – are shown in Figure 4, fitted to least-squares exponential decay curves. Fit parameters and correlation lifetimes may be found in Table 3. The ion-pairing correlation lifetimes for the small box simulations are found to be 121 and 77 ps for NO_3^- and NO_2^-, below the 160 ps interval at which parameters were stored for electronic structure calculations.

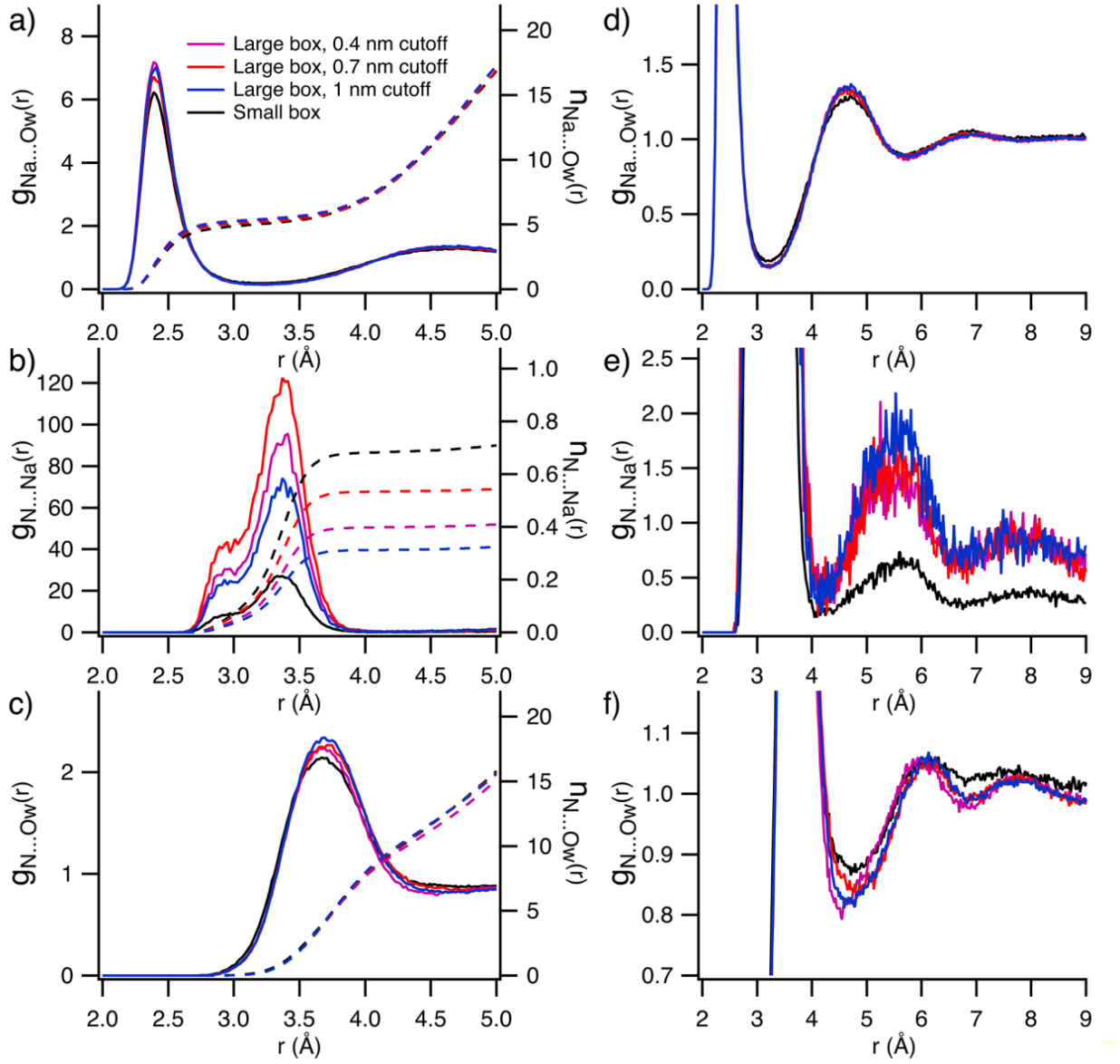

Figure 2: a) Radial distribution functions {RDFs, *g(r)*} and integrated radial distribution functions {nRDFs, *n(r)*, shown as dashed lines} for the interaction of the sodium ion with water oxygen in MD simulations of $NaNO_3$; b) RDFs and nRDFs for the interaction of the sodium ion with nitrate (measured from the position of the nitrogen atom) for the same MD simulations; c) RDFs and nRDFs for the interaction of the nitrate nitrogen atom with water oxygen; d-f) contain the RDFs from a-c, respectively, extended to longer range and expanded to lower values on the y-axis to show second and third solvation layers in ion-water RDFs and solvent-separated ion pair formation in the ion-ion RDF. The splitting observed in b) arises from the existence of two distinct ion-pairing configurations, one in which the cation sits between two of the oxygen atoms of the nitrate anion, closer to the nitrogen, and one in which the sodium ion interacts with only one oxygen atom, further from the nitrogen.

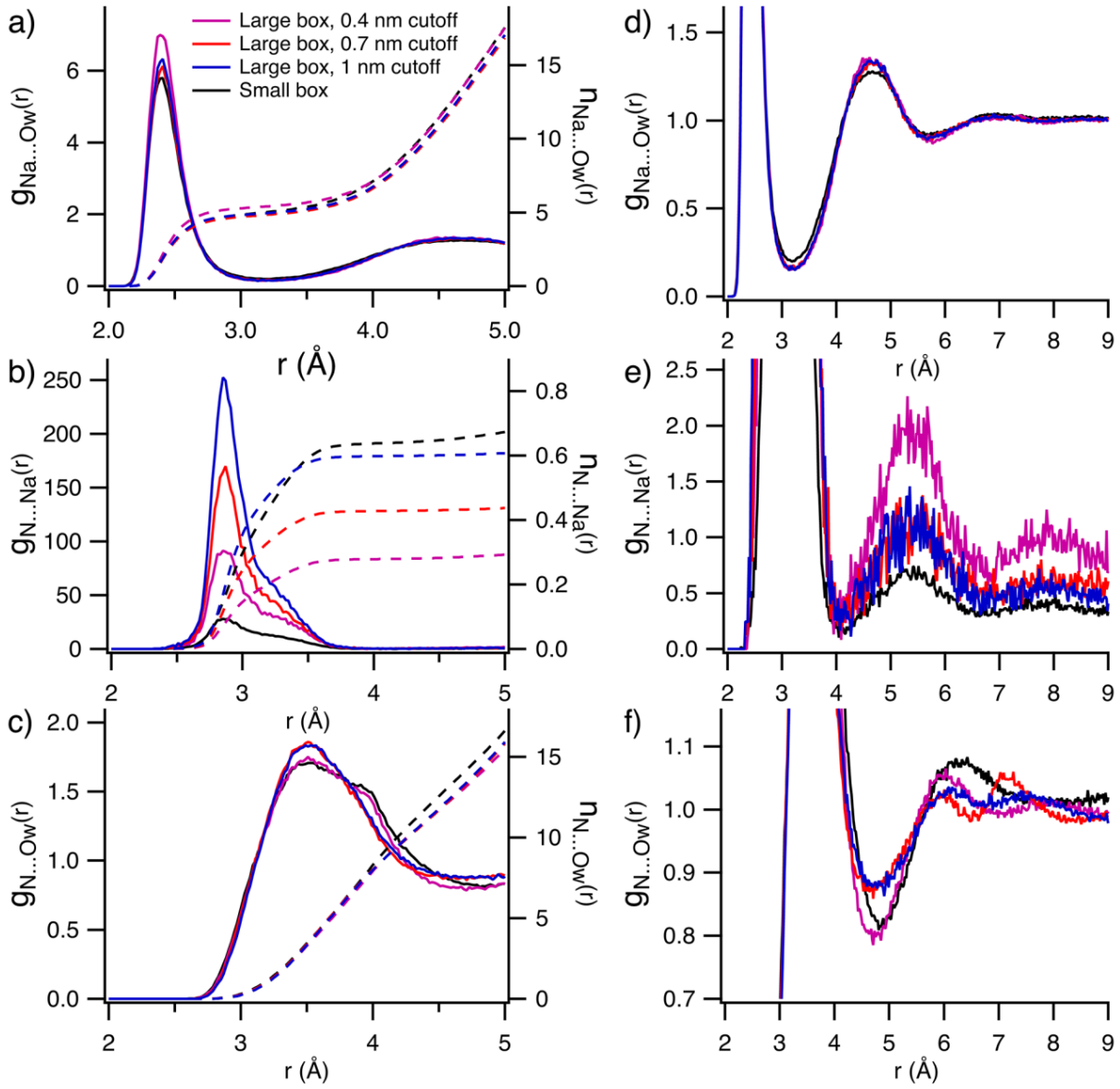

Figure 3: a) RDFs {*g(r)*} and nRDFs {*n(r)*, shown as dashed lines} for the interaction of the sodium ion with water oxygen in MD simulations of $NaNO_2$; b) RDFs and nRDFs for the interaction of the sodium ion with nitrite (measured from the position of the nitrogen atom) for the same MD simulations; c) RDFs and nRDFs for the interaction of the nitrite nitrogen atom with water oxygen; d-f) contain the RDFs from a-c, respectively, extended to longer range and expanded to lower values on the y-axis to show second and third solvation layers in ion-water RDFs and solvent-separated ion pair formation in the ion-ion RDF. The Na^+…water RDF exhibits different behavior outside the first solvation shell for different interaction cutoff lengths. This behavior was not observed in the Na^+…water RDFs for the nitrate simulations, which overlaid well across all interaction cutoffs.

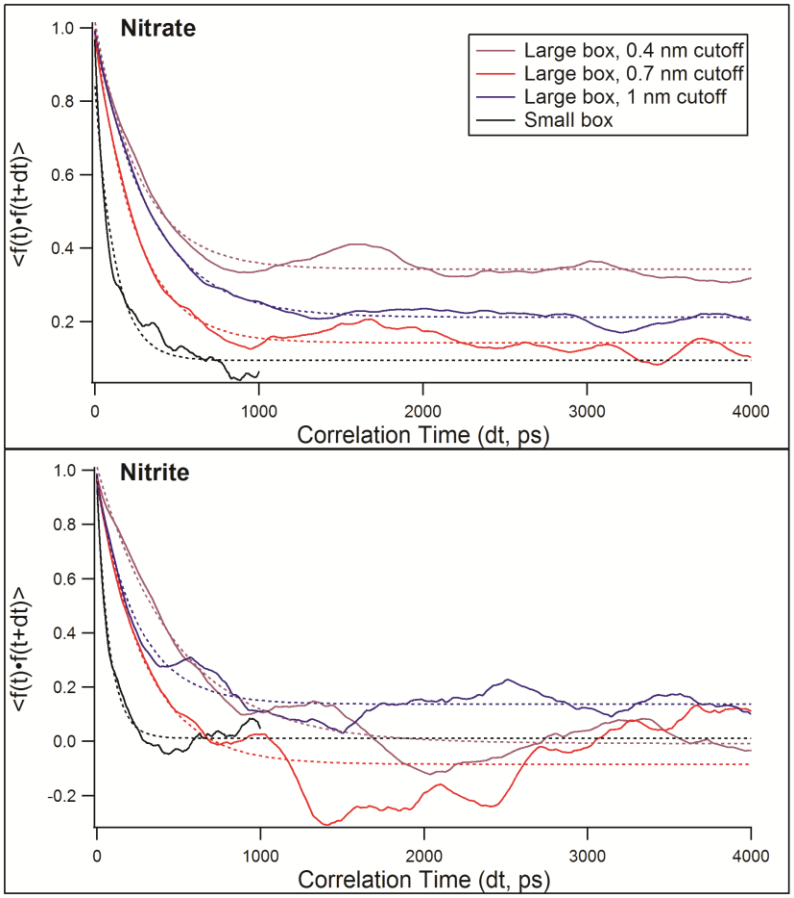

Figure 4: Correlation functions <f(t)·f(t+dt)> for anion-cation interactions in MD simulations of $NaNO_3$ (top) and $NaNO_2$ (bottom). Least-squares best fit exponential decay curves for each correlation function are indicated by dashed lines of corresponding color. Coefficients for best-fit lines and corresponding correlation times are listed in Table 3.

Table 3: Fit coefficients from the least-squares exponential fits of form $f(dt) = Y_0 + Ae^{-dt/\tau}$ to the ion-pairing correlation plots in Figure 4. The first 3 rows for each anion contain the fit parameters to the correlation curves from the large box simulation results with 4, 7, and 10 Å cutoffs for intermolecular interactions, while the fourth line contains the fit parameters for the correlation curve of the small box simulation. The correlation lifetimes τ are found in the last column.

	Cutoff (Å)	Y_0	A	$1/\tau$ (ps^{-1}) $\times 10^{-3}$	τ (ps)
NO_3^-	4	0.342(4)	0.67(3)	3.6(5)	274
	7	0.141(7)	0.85(6)	4.1(4)	242
	10	0.211(2)	0.782(0)	3.00(8)	332
(small box)	4	0.093(9)	0.74(7)	8.2(7)	121
NO_2^-	4	-0.008(3)	1.02(0)	2.0(9)	479
	7	-0.08(5)	1.05(5)	3.5(1)	285
	10	0.136(9)	0.80(9)	4.0(1)	249
(small box)	4	0.011(6)	0.91(0)	12.(9)	77

The sodium-water RDFs exhibit a maximum for the first solvation shell at 2.4 Å and corresponding minimum between the first two shells at 3.15 Å, consistent with literature values from experiments and theory.[35–37] The Na^+ hydration number obtained by the value of the nRDF at the 3.15 Å minimum is found to be ~4.9. This is slightly lower than previously reported values, but within error of most;[36,38–40] furthermore, the hydration numbers from the small box simulations used for electronic structure calculations are found to be slightly higher at ~5.05.

MD simulations reveal very little difference in the hydration properties of nitrate and nitrite. The hydration of each anion was found to be consistent between the small and large simulation boxes and across interaction lengths, with nitrate and nitrite hydrated by an average of 11.8 and 11.9 water molecules, respectively, in the first shell. These values are somewhat larger than previously reported hydration numbers from ab initio simulations[41,42] and classical MD simulations.[9] Some of this discepancy is likely explained by differences in the method by which hydration number is calculated. Many previous papers have estimated hydration numbers by the number of hydrogen bond donors or the RDF from the oxygen atoms. We have estimated hydration numbers from the integrated RDF, counting water molecules around the oxygen atoms as well as those directly interacting with the nitrogen center and effectively including non-bonding or weakly-interacting near-neighbors (i.e. not in a traditional hydrogen bond donor geometry with respect to the anion). Experimental estimates of the hydration numbers from scattering and infrared absorption experiments vary substantially,[43–45] with one X-ray diffraction study finding a hydration number for nitrate as high as 17.7.[46] The question of solvation structure is further complicated by the suggestion of Simeon et al. that two distinguishable forms of aqueous NO_3^- with differing solvation numbers coexist near room temperature.[47] Furthermore, it has been suggested that the first solvation shell of the nitrate anion, from the standpoint of solvation thermodynamics and polarizability, contains only 3 water molecules,[8,48] suggesting that precise solvation number from the integrated RDF may have a limited effect on electronic structure and associated transition dipole oscillator strengths. The maximum of the first peak in the $N\ldots O_{water}$ RDF, corresponding to the first solvation shell, is consistently located at 3.7 Å. This is slightly longer than the average experimental radius of 3.51 Å measured at 25º C via X-ray diffraction.[49] The maximum of the nitrite $N\ldots O_{water}$ RDF is located closer to the nitrogen, at 3.5 Å; however, this results from the nearer proximity of oxygen to the increased exposure of the nitrogen atom, and the hydrogen bond lengths are similar to those from the nitrate simulations. The first peak of the RDF extends to the same minimum at 4.5 Å as that found for nitrate.

Calculated XA spectra of the nitrogen K-edge for ion-paired and unpaired molecular configurations of NO_3^- and NO_2^- are compared to the experimental spectra in Figure 5. The theoretical spectra accurately reproduce the spectral features observed in the experimental spectra. No significant differences between the ion-paired and unpaired spectra are evident for either anion. This is consistent with the experimental findings of an XAS spectrum independent of solution concentration. A spectral shift of 3.7 eV is observed between the 1s-π^* features of nitrate and nitrite, consistent with the 3.65 eV shift between the experimental spectra. The computed valence density of states exhibit no substantial shift in the positions of the available virtual orbitals in the ground state (LUMO shift of ~0.07 eV), indicating that the observed and calculated spectral shift derives from a difference in the energy levels of the nitrogen 1s core levels of nitrate and nitrite. This is consistent with the previously-noted similar spectral shift observed in the XPS spectra of the ions.[11]

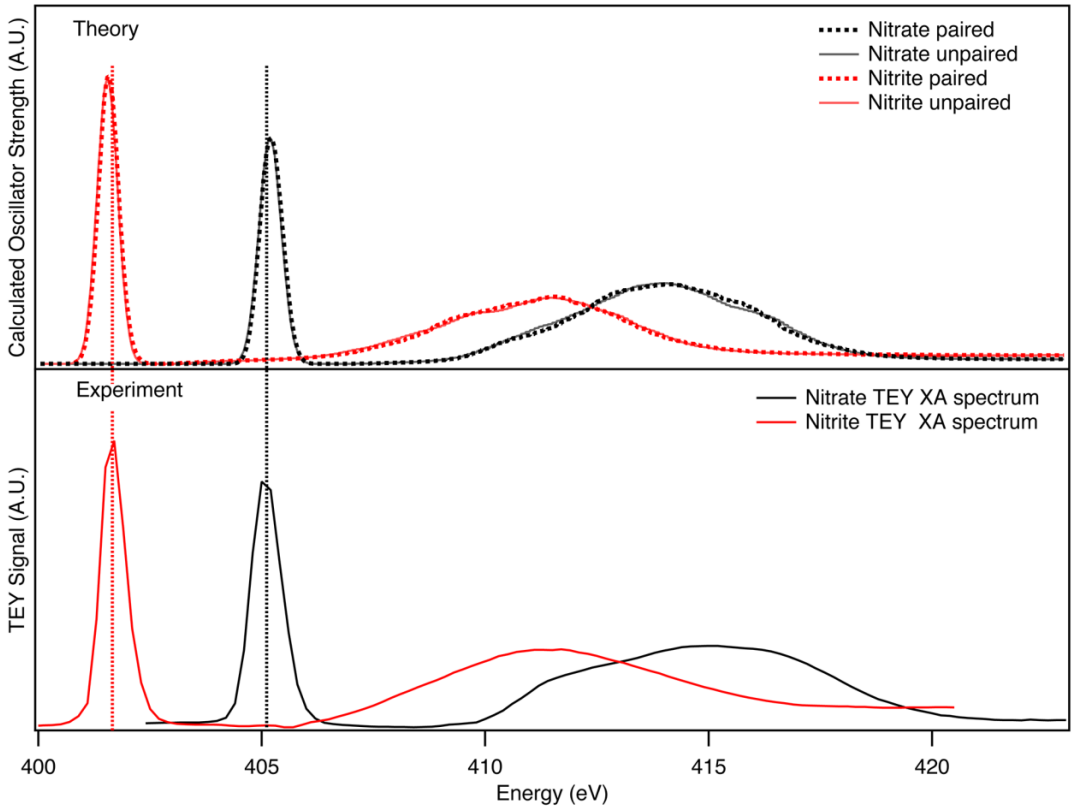

Figure 5: Calculated nitrogen K-edge XA spectra of ion-paired and unpaired molecular configurations of $NaNO_3$ (black) and $NaNO_2$ (red). The lower panel shows the corresponding experimental spectra for comparison. Experimental and theoretical spectra have both been calibrated via a single-point energy alignment relative to the well-characterized spectrum of N_2 gas. The calculated spectra of ion-paired and unpaired molecular configurations indicate that the nitrogen K-edge spectrum is not sensitive to ion pairing. Dashed vertical lines indicate the peak centers of the 1s-π* transition for each anion in the experimental spectrum. The calculated spectrum of NO_2^- matches experiment well; a blue shift of .05 eV relative to experiment is observed for NO_3^-.

Density isosurfaces of the core-excited LUMO and LUMO+1 states of aqueous nitrate and nitrite are exhibited in Figure 6. The LUMO for each anion exhibits π* symmetry, while the LUMO+1 exhibits primarily σ* character but is highly delocalized, with substantial electron density observed on solvent molecules throughout the simulation cell. The π* LUMO state is highly localized on the ion, with almost no electron density observed on the solvent water. This explains the insensitivity of the spectral feature associated with the transition into this state to the solvation environment of the ion. Similarly, the substantial extent of delocalization observed in the σ* states may explain their calculated and observed spectral insensitivity to the local environment; as the calculated electron density extends well beyond the first solvation shell and does not appear to favor hydrogen-bonded solvent molecules, the state may be sampling the bulk solvent sufficiently to render local structure fluctuations insignificant. Similar electronic structures have previously been found to exhibit spectral insensitivity to the local solvation environment in boron oxides.[50]

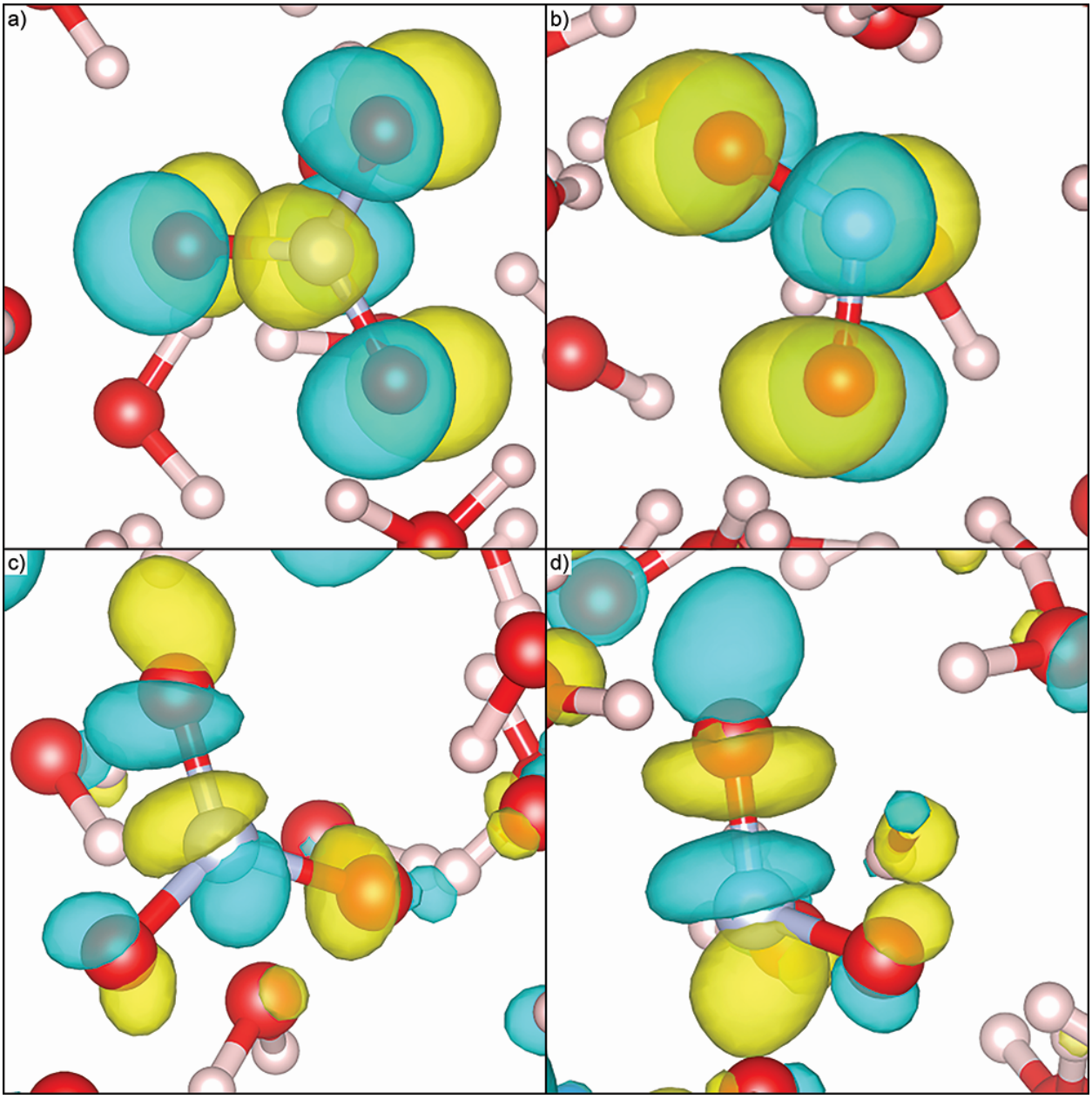

Figure 6: Electron-density isosurfaces of the LUMO and LUMO+1 core excited states of aqueous nitrate and nitrite anions. Images a) and b) show the calculated isosurfaces of the LUMO of nitrate and nitrite, respectively. These states exhibit distinctive π* geometry and are almost entirely localized on the anion. Images c) and d) exhibit the LUMO+1 of nitrate and nitrite, respectively. These states have primarily σ* character and are highly delocalized; while the displayed image highlights the character of the state on the anion, significant electron density is calculated to exist on water molecules throughout the simulation cell. Some solvent-centered density may be observed here, and does not appear to depend on hydrogen bonding or other specific solvent-solute geometries.

We have also computed the oxygen K-edge XA spectra of the nitrate and nitrite anions from the same snapshots; these are displayed in Figure 7. The computed spectra of ion-paired and unpaired snapshots were once again near-identical, and only the average of all snapshots is displayed. Oxygen K-edge spectra are found to be in the same energy range for nitrate and nitrite, suggesting that the enhanced core-level stabilization of the nitrogen atom in nitrate relative to nitrite is not present in the oxygen atoms. Generally, measurement of the XA spectra of aqueous solutes at the oxygen K-edge is not plausible due to the high-intensity, broad background spectrum of the H_2O solvent. The calculated position of the first feature in the spectrum of aqueous nitrate and nitrite, however, is at slightly lower energy than the onset of water signal between 532 and 533 eV, and it may be possible to observe this feature in experimental spectra in future studies.

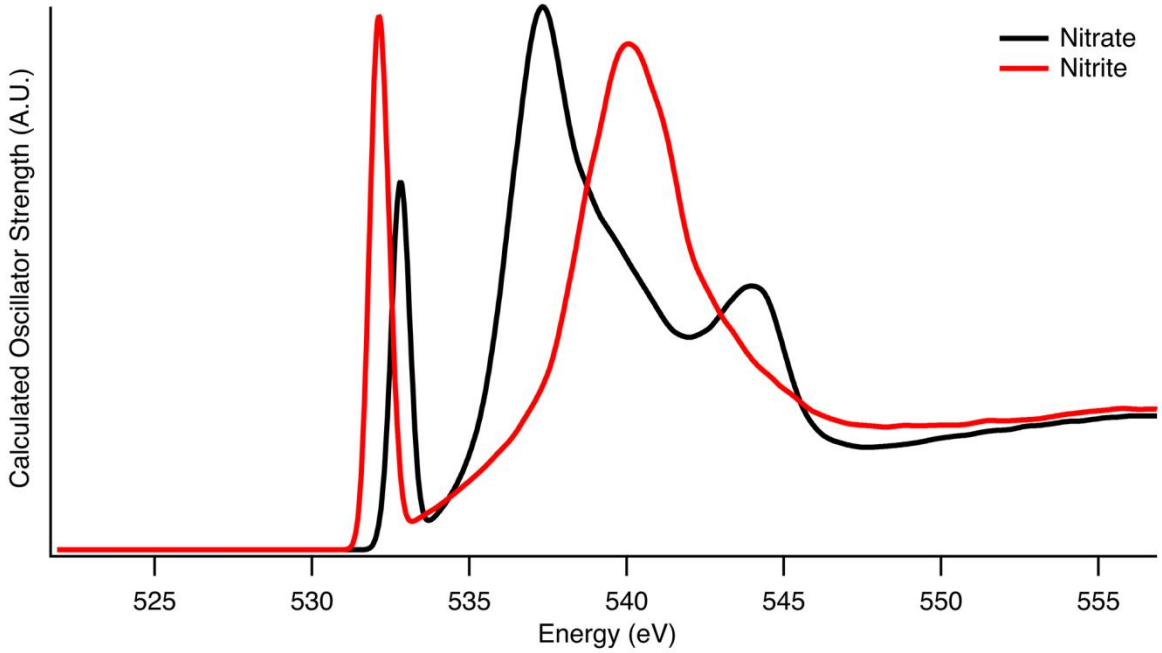

Figure 7: Calculated oxygen K-edge XA spectra of NO_3^- and NO_2^-. Energy calibration was performed relative to the oxygen K-edge absorption spectrum of gaseous CO_2. As with the calculated nitrogen K-edge spectra exhibited in Figure 5, the calculated oxygen K-edge spectra of ion-paired and unpaired molecular configurations overlaid nearly exactly. Consequently, only the overall average spectra are displayed here. Collection of experimental oxygen K-edge absorption spectra is implausible due to the broad, high-intensity background signal generated by the liquid water solvent.

V. Conclusions

We have presented the first XA spectra of aqueous NO_3^- and NO_2^-. The hydration properties and ion-pairing propensities of the anions are found to be similar. The XA spectrum of NO_2^- is red-shifted by 3.7 eV relative to the NO_3^- spectrum; the theory indicates that this shift arises from a relative stabilization of the nitrogen 1s ground state in nitrate. The spectra are found to be insensitive to the local environment; this is likely a result of the localization of the π^* state on the anion and delocalization of the σ^* state well into the bulk water beyond the first

hydration shell. Calculated XA spectra of the oxygen K-edge of nitrate and nitrite do not indicate a substantial shift between the spectra of the two anions.

VI. References

(1) Sutton, M. A.; Oenema, O.; Erisman, J. W.; Leip, A.; van Grinsven, H.; Winiwarter, W. Too Much of a Good Thing. *Nature* **2011**, *472* (7342), 159–161.

(2) Dulong, F.; Pouessel, J.; Thuéry, P.; Berthet, J.-C.; Ephritikhine, M.; Cantat, T. Nitrite Complexes of Uranium and Thorium. *Chem. Commun. (Camb).* **2013**, *49* (24), 2412–2414.

(3) Lundberg, J. O.; Weitzberg, E.; Gladwin, M. T. The Nitrate-Nitrite-Nitric Oxide Pathway in Physiology and Therapeutics. *Nat. Rev. Drug Discov.* **2008**, *7* (2), 156–167.

(4) Wayne, R. P. *Chemistry of Atmospheres*; Oxford University Press: Oxford, 2000.

(5) Hunt, S. W.; Roeselová, M.; Wang, W.; Wingen, L. M.; Knipping, E. M.; Tobias, D. J.; Dabdub, D.; Finlayson-Pitts, B. J. Formation of Molecular Bromine from the Reaction of Ozone with Deliquesced NaBr Aerosol: Evidence for Interface Chemistry. *J. Phys. Chem. A* **2004**, *108* (52), 11559–11572.

(6) Wingen, L. M.; Moskun, A. C.; Johnson, S. N.; Thomas, J. L.; Roeselová, M.; Tobias, D. J.; Kleinman, M. T.; Finlayson-Pitts, B. J. Enhanced Surface Photochemistry in Chloride-Nitrate Ion Mixtures. *Phys. Chem. Chem. Phys.* **2008**, *10* (37), 5668–5677.

(7) Jungwirth, P.; Tobias, D. J. Specific Ion Effects at the Air/Water Interface. *Chem. Rev.* **2006**, *106* (4), 1259–1281.

(8) Salvador, P.; Curtis, J. E.; Tobias, D. J.; Jungwirth, P. Polarizability of the Nitrate Anion and Its Solvation at the Air/water Interface. *Phys. Chem. Chem. Phys.* **2003**, *5* (17), 3752.

(9) Dang, L. X.; Chang, T.-M.; Roeselova, M.; Garrett, B. C.; Tobias, D. J. On NO3--H2O Interactions in Aqueous Solutions and at Interfaces. *J. Chem. Phys.* **2006**, *124* (6), 66101.

(10) Thomas, J. L.; Roeselová, M.; Dang, L. X.; Tobias, D. J. Molecular Dynamics Simulations of the Solution-Air Interface of Aqueous Sodium Nitrate. *J. Phys. Chem. A* **2007**, *111* (16), 3091–3098.

(11) Brown, M. A.; Winter, B.; Faubel, M.; Hemminger, J. C. Spatial Distribution of Nitrate and Nitrite Anions at the Liquid/vapor Interface of Aqueous Solutions. *J. Am. Chem. Soc.* **2009**, *131* (24), 8354–8355.

(12) Otten, D. E.; Petersen, P. B.; Saykally, R. J. Observation of Nitrate Ions at the Air/water Interface by UV-Second Harmonic Generation. *Chem. Phys. Lett.* **2007**, *449* (4–6), 261–265.

(13) Levin, Y. Polarizable Ions at Interfaces. *Phys. Rev. Lett.* **2009**, *102* (14), 147803.

(14) Geissler, P. L. Water Interfaces, Solvation, and Spectroscopy. *Annu. Rev. Phys. Chem.* **2013**, *64*, 317–337.

(15) Vaikuntanathan, S.; Shaffer, P. R.; Geissler, P. L. Adsorption of Solutes at Liquid–vapor Interfaces: Insights from Lattice Gas Models. *Faraday Discuss.* **2013**, *160*, 63–74.

(16) Caleman, C.; Hub, J. S.; van Maaren, P. J.; van der Spoel, D. Atomistic Simulation of Ion Solvation in Water Explains Surface Preference of Halides. *Proc. Natl. Acad. Sci.* **2011**, *108* (17), 6838–6842.

(17) Otten, D. E.; Onorato, R.; Michaels, R.; Goodknight, J.; Saykally, R. J. Strong Surface Adsorption of Aqueous Sodium Nitrite as an Ion Pair. *Chem. Phys. Lett.* **2012**, *519–520*, 45–48.

(18) Shih, O.; England, A. H.; Dallinger, G. C.; Smith, J. W.; Duffey, K. C.; Cohen, R. C.; Prendergast, D.; Saykally, R. J. Cation-Cation Contact Pairing in Water: Guanidinium. *J. Chem. Phys.* **2013**, *139* (3), 35104.

(19) England, A. H.; Duffin, A. M.; Schwartz, C. P.; Uejio, J. S.; Prendergast, D.; Saykally, R. J. On the Hydration and Hydrolysis of Carbon Dioxide. *Chem. Phys. Lett.* **2011**, *514* (4–6), 187–195.

(20) Lam, R. K.; England, A. H.; Sheardy, A. T.; Shih, O.; Smith, J. W.; Rizzuto, A. M.; Prendergast, D.; Saykally, R. J. The Hydration Structure of Aqueous Carbonic Acid from X-Ray Absorption Spectroscopy. *Chem. Phys. Lett.* **2014**, *614*, 282–286.

(21) Lam, R. K.; England, A. H.; Smith, J. W.; Rizzuto, A. M.; Shih, O.; Prendergast, D.; Saykally, R. J. The Hydration Structure of Dissolved Carbon Dioxide from X-Ray Absorption Spectroscopy. *Chem. Phys. Lett.* **2015**, *633*, 214–217.

(22) Smith, J. W.; Lam, R. K.-J.; Sheardy, A. T.; Shih, O.; Rizzuto, A. M.; Borodin, O.; Harris, S. J.; Prendergast, D.; Saykally, R. J. X-Ray Absorption Spectroscopy of LiBF4 in Propylene Carbonate: A Model Lithium Ion Battery Electrolyte. *Phys. Chem. Chem. Phys.* **2014**.

(23) Wilson, K. R.; Rude, B. S.; Catalane, T.; Schaller, R. D.; Tobin, J. G.; Co, D. T.; Saykally, R. J. X-Ray Spectroscopy of Liquid Water Microjets. *J. Phys. Chem. B* **2001**, *105* (17), 3346–3349.

(24) Cappa, C. D.; Smith, J. D.; Wilson, K. R.; Saykally, R. J. Revisiting the Total Ion Yield X-Ray Absorption Spectra of Liquid Water Microjets. *J. Phys. Condens. Matter* **2008**, *20* (20), 205105.

(25) Wilson, K. R.; Rude, B. S.; Smith, J.; Cappa, C.; Co, D. T.; Schaller, R. D.; Larsson, M.; Catalano, T.; Saykally, R. J. Investigation of Volatile Liquid Surfaces by Synchrotron X-Ray Spectroscopy of Liquid Microjets. *Rev. Sci. Instrum.* **2004**, *75* (3), 725–736.

(26) D.A. Case, V. Babin, J.T. Berryman, R.M. Betz, Q. Cai, D.S. Cerutti, T.E. Cheatham, III, T.A. Darden, R.E. Duke, H. Gohlke, A.W. Goetz, S. Gusarov, N. Homeyer, P. Janowski, J. Kaus, I. Kolossváry, A. Kovalenko, T.S. Lee, S. LeGrand, T. Luchko, R. Luo, B. Madej, K.M. Merz, F. Paesani, D.R. Roe, A. Roitberg, C. Sagui, R. Salomon-Ferrer, G. Seabra, C.L. Simmerling, W. Smith, J. Swails, R.C. Walker, J. Wang, R.M. Wolf, X. Wu and P.A. Kollman (2014), AMBER 14, University of California, San Francisco.

(27) Humphrey, W.; Dalke, A.; Schulten, K. VMD: Visual Molecular Dynamics. *J. Mol. Graph.* **1996**, *14* (1), 33–38.

(28) Prendergast, D.; Galli, G. X-Ray Absorption Spectra of Water from First Principles Calculations. *Phys. Rev. Lett.* **2006**, *96* (21), 215502.

(29) Giannozzi, P.; Baroni, S.; Bonini, N.; Calandra, M.; Car, R.; Cavazzoni, C.; Ceresoli, D.; Chiarotti, G. L.; Cococcioni, M.; Dabo, I.; et al. QUANTUM ESPRESSO: A Modular and Open-Source Software Project for Quantum Simulations of Materials. *J. Phys. Condens. Matter* **2009**, *21* (39), 395502.

(30) Perdew, J. P.; Burke, K.; Ernzerhof, M. Generalized Gradient Approximation Made Simple. *Phys. Rev. Lett.* **1996**, *77* (18), 3865–3868.

(31) Rodriguez, J. A.; Jirsak, T.; Dvorak, J.; Sambasivan, S.; Fischer, D. Reaction of NO_2 with Zn and ZnO: Photoemission, XANES, and Density Functional Studies on the Formation of NO 3. *J. Phys. Chem. B* **2000**, *104* (2), 319–328.

(32) Messer, B. M.; Cappa, C. D.; Smith, J. D.; Wilson, K. R.; Gilles, M. K.; Cohen, R. C.; Saykally, R. J. pH Dependence of the Electronic Structure of Glycine. *J. Phys. Chem. B* **2005**, *109* (11), 5375–5382.

(33) Marcos-Arroyo, M. der M.; Khoshkbarchi, M. K.; Vera, J. H. Activity Coefficients of Sodium, Potassium, and Nitrate Ions in Aqueous Solutions of NaNO3, KNO3, and NaNO3+KNO3 at 25°C. *J. Solution Chem.* **1996**, *25* (10), 983–1000.

(34) Staples, B. R. Activity and Osmotic Coefficients of Aqueous Alkali Metal Nitrites. *J. Phys. Chem. Ref. Data* **1981**, *10* (3), 765.

(35) Skipper, N. T.; Neilson, G. W. X-Ray and Neutron Diffraction Studies on Concentrated Aqueous Solutions of Sodium Nitrate and Silver Nitrate. *J. Phys. Condens. Matter* **1989**, *1* (26), 4141–4154.

(36) Mancinelli, R.; Botti, A.; Bruni, F.; Ricci, M. A.; Soper, A. K. Hydration of Sodium, Potassium, and Chloride Ions in Solution and the Concept of Structure Maker/breaker. *J. Phys. Chem. B* **2007**, *111* (48), 13570–13577.

(37) Neilson, G. W.; Mason, P. E.; Ramos, S.; Sullivan, D. Neutron and X-Ray Scattering Studies of Hydration in Aqueous Solutions. *Philos. Trans. R. Soc. A Math. Phys. Eng. Sci.* **2001**, *359* (1785), 1575–1591.

(38) White, J. A.; Schwegler, E.; Galli, G.; Gygi, F. The Solvation of Na^+ in Water: First-Principles Simulations. *J. Chem. Phys.* **2000**, *113* (11), 4668.

(39) Carrillo-Tripp, M.; Saint-Martin, H.; Ortega-Blake, I. A Comparative Study of the Hydration of Na^+ and K^+ with Refined Polarizable Model Potentials. *J. Chem. Phys.* **2003**, *118* (15), 7062.

(40) Bankura, A.; Carnevale, V.; Klein, M. L. Hydration Structure of Salt Solutions from Ab Initio Molecular Dynamics. *J. Chem. Phys.* **2013**, *138* (1), 14501.

(41) Vchirawongkwin, V.; Kritayakornupong, C.; Tongraar, A.; Rode, B. M. Symmetry Breaking and Hydration Structure of Carbonate and Nitrate in Aqueous Solutions: A Study by Ab Initio Quantum Mechanical Charge Field Molecular Dynamics. *J. Phys. Chem. B* **2011**, *115* (43), 12527–12536.

(42) Vchirawongkwin, S.; Kritayakornupong, C.; Tongraar, A.; Vchirawongkwin, V. Hydration Properties Determining the Reactivity of Nitrite in Aqueous Solution. *Dalton Trans.* **2014**, *43* (32), 12164–12174.

(43) Ohtaki, H.; Radnai, T. Structure and Dynamics of Hydrated Ions. *Chem. Rev.* **1993**, *93* (3), 1157–1204.

(44) Bergstroem, P. A.; Lindgren, J.; Kristiansson, O. An IR Study of the Hydration of Perchlorate, Nitrate, Iodide, Bromide, Chloride and Sulfate Anions in Aqueous Solution. *J. Phys. Chem.* **1991**, *95* (22), 8575–8580.

(45) Kameda, Y.; Arakawa, H.; Hangai, K.; Uemura, O. The Structure around the Nitrite Ion in Concentrated Aqueous Solutions. *Bull. Chem. Soc. Jpn.* **1992**, *65* (8), 2154–2156.

(46) Dagnall, S. P.; Hague, D. N.; Towl, A. D. C. X-Ray Diffraction Study of Aqueous zinc(II) Nitrate. *J. Chem. Soc. Faraday Trans. 2* **1982**, *78* (12), 2161.

(47) Simeon, V.; Butorac, V.; Tomišić, V.; Kallay, N. Existence of Two Forms of Nitrate Ion in Dilute Aqueous Solutions. Thermodynamic Parameters of Interconversion. *Phys. Chem. Chem. Phys.* **2003**, *5* (10), 2015.

(48) Wang, X.-B.; Yang, X.; Wang, L.-S.; Nicholas, J. B. Photodetachment and Theoretical Study of Free and Water-Solvated Nitrate Anions, $NO_3^-(H_2O)_n$ (n=0–6). *J. Chem. Phys.* **2002**, *116* (2), 561.

(49) Caminiti, R.; Licheri, G.; Piccaluga, G.; Pinna, G. On NO_3^-–H2O Interactions in Aqueous Solutions. *J. Chem. Phys.* **1978**, *68* (4), 1967.

(50) Duffin, A. M.; Schwartz, C. P.; England, A. H.; Uejio, J. S.; Prendergast, D.; Saykally, R. J. pH-Dependent X-Ray Absorption Spectra of Aqueous Boron Oxides. *J. Chem. Phys.* **2011**, *134* (15), 154503.